

DISSERTATION

The effect of substitution and doping on the thermoelectric properties of CePd_3 (Cer Palladium 3)

ausgeführt zum Zwecke der Erlangung des akademischen Grades
eines Doktors der technischen Wissenschaften
unter der Leitung von

Ao.Univ.Prof.Dipl.-Ing.Dr.techn. Ernst Bauer

E138
Institut für Festkörperphysik

eingereicht an der Technischen Universität Wien
Technisch-Naturwissenschaftliche Fakultät
von

DI Robert Lackner
Matr.-Nr. 9526017
Neugasse 10
2453 Sommerein

Wien, im Mai 2007

Kurzfassung

Zwischenvalentes CePd_3 hat einen der höchsten Seebeckkoeffizienten unter den auf Ce basierenden intermetallischen Systemen. In Rahmen dieser Dissertation wurden vier Probenreihen (CePd_3B_y , $\text{Ce}(\text{Pd}_{1-x}\text{Rh}_x)_3$, $\text{Ce}(\text{Pd}_{1-x}\text{Rh}_x)_3\text{B}_{0.05}$ und $\text{Ce}(\text{Pd}_{0.94-x}\text{Rh}_x\text{Ag}_{0.06})_3$) hergestellt, um den Einfluss von Substitution an der Pd-Seite, sowie den Effekt von B Doping am freien Zwischengitterplatz auf die Transporteigenschaften zu untersuchen. Mittels Röntgendiffraktometrie wurden die Proben auf Phasenreinheit untersucht und anschließend wurden der elektrische Widerstand $\rho(T)$, die thermische Leitfähigkeit $\lambda(T)$ und der Seebeckeffekt $S(T)$ über einen großen Temperaturbereich gemessen. Die Daten wurden anhand theoretischer und empirischer Modelle analysiert. Durch die Auswertung von $\rho(T)$ und $S(T)$ konnte gezeigt werden, dass die Kondotemperatur bei kleinen Rh-Konzentrationen, nicht wie erwartet, stetig mit der Konzentration steigt, sondern vorerst absinkt. Mit einem Rh Anteil $x > 0.2$ wird das System einfach metallisch. Bei einer Zugabe von B verschiebt sich das Maximum in $\rho(T)$ und $S(T)$ wie erwartet zu tieferen Temperaturen, wobei ρ_{max} steigt, während S_{max} abnimmt. Die verwendeten Modelle können die Messwerte über einen breiten Temperaturbereich gut reproduzieren und die erhaltenen fit-Parameter sind sinnvoll. Die gemessene thermische Leitfähigkeit wurde anhand von zwei verschiedenen Modellen in ihren elektronischen- und ihren Gitteranteil geteilt, wobei beide Methoden vergleichbare Resultate lieferten. Der Gitterbeitrag wurde weiter analysiert um Aufschluss über einzelne Streumechanismen der Phononen zu erlangen. Durch die hohe Anzahl an fit-Parametern sind hier nur qualitative Aussagen möglich. Die thermische Leitfähigkeit bei tiefen Temperaturen sinkt generell bei geringfügiger Änderung der Stöchiometrie, wobei der Effekt bei Raumtemperatur nicht besonders stark ist. Für den thermoelektrischen Gütefaktor ZT bedeutet das, dass eine Zugabe von B oder eine Substitution von Pd durch Ag eine klare Verschlechterung bringt, während kleine Substitutionen mit Rh die thermoelektrischen Eigenschaften verbessern. Es sollte geprüft werden, ob es möglich ist, die Einbuße des Seebeckeffekts durch B Doping oder Ag Substitution durch Rh Substitution zu kompensieren und bei stark verringertem Phononenbeitrag der thermischen Leitfähigkeit eine Verbesserung von ZT zu erzielen. Bei den Serien $\text{Ce}(\text{Pd}_{1-x}\text{Rh}_x)_3\text{B}_{0.05}$ und $\text{Ce}(\text{Pd}_{0.94-x}\text{Rh}_x\text{Ag}_{0.06})_3$ hat sich gezeigt, dass $\lambda(T)$ weiterhin niedrige Werte aufweist, und auch $\rho(T)$ generell absinkt, wenn man den Rh Anteil erhöht. Auch der Seebeckeffekt wird verstärkt und somit wird der Gütefaktor tatsächlich größer, aber es wurde keine nennenswerte Überhöhung erreicht. Somit erreicht der Gütefaktor bei einer Zusammensetzung von $\text{Ce}(\text{Pd}_{0.9}\text{Rh}_{0.1})_3$ sein Maximum, das bei Raumtemperatur etwa 12% über dem Wert von CePd_3 liegt.

Abstract

The intermediate valency compound CePd_3 exhibits one of the highest Seebeck coefficients of Ce-based intermetallics. In the scope of this thesis the effect of substitution on the Pd site and doping on the interstitial site on the transport properties of CePd_3 has been tested on four sample series, namely CePd_3B_y , $\text{Ce}(\text{Pd}_{1-x}\text{Rh}_x)_3$, $\text{Ce}(\text{Pd}_{1-x}\text{Rh}_x)_3\text{B}_{0.05}$ and $\text{Ce}(\text{Pd}_{0.94-x}\text{Rh}_x\text{Ag}_{0.06})_3$. Phase purity of the samples was examined by employing X-Ray diffraction as well as the electrical resistivity $\rho(T)$, the thermal conductivity $\lambda(T)$ and the thermopower $S(T)$ were recorded over a broad temperature region. The measured data were interpreted by means of theoretical and empirical models. The analysis of $\rho(T)$ and $S(T)$ shows, that the Kondo temperature does not increase steadily with increasing Rh content as it was expected, rather it shows a small degradation with small Rh-concentrations. For a Rh content $x > 0.2$ the system behaves as a simple metal. Increasing doping with B causes a shift of the maximum in $\rho(T)$ and $S(T)$ to lower temperatures, while ρ_{max} increases and S_{max} diminishes. The applied models reproduce the measured data over a broad temperature region and the attained fit-parameters are reasonable. In terms of the analysis of thermal conductivity data two ways of splitting the thermal conductivity into an electronic part and a lattice contribution have been tested and the results of both are comparable. The lattice contribution was tested in order to understand the contributions of the different phonon scattering mechanisms. Due to the high count of fit-parameters only qualitative statements are possible. Due to minor changes of the stoichiometry the thermal conductivity generally decreases at low temperatures, while it is rather unaffected at room temperature. As a consequence the thermoelectric figure of merit ZT is diminished by the doping with B as well as by substitution with Ag on the Pd-site, while the substitution with small amounts of Rh enhance the thermoelectric properties. It had to be tested if it is possible to compensate the loss of thermopower due to Ag substitution and B doping by Rh substitution and if the ZT can be improved with a further decrease of the phonon scattering part of the thermal conductivity. The series $\text{Ce}(\text{Pd}_{1-x}\text{Rh}_x)_3\text{B}_{0.05}$ and $\text{Ce}(\text{Pd}_{0.94-x}\text{Rh}_x\text{Ag}_{0.06})_3$ exhibit still low $\lambda(T)$ - values, and $\rho(T)$ generally decreases, with increasing Rh content. The thermopower showed also an upward trend and therefore the figure of merit actually increased, but no boost in comparison to CePd_3 was reached. Thus the figure of merit peak out at a composition of $\text{Ce}(\text{Pd}_{0.9}\text{Rh}_{0.1})_3$, which shows about 12% higher values than CePd_3 at room temperature.

Ich danke...

... meinem Doktorvater Prof. Dr. Ernst Bauer, der mir mit Rat und Tat zu Seite stand. Er ermöglichte mir weitgehend freies Arbeiten in freundschaftlicher Atmosphäre und damit die Fertigstellung dieser Dissertation.

... dem gesamten Team des Instituts für Festkörperphysik für das freundschaftliche Arbeitsklima und die Hilfsbereitschaft mit der mich alle unterstützt haben.

... der Mannschaft unserer Werkstatt für die rasche und genaue Abwicklung aller Projekte sowie für deren Unterstützung bei allerlei gefinkelten Problemstellungen.

... Prof. Dr. Peter Rogl und seinem Team vom Institut für Physikalische Chemie der Universität Wien für die Hilfestellung bei der Probenpräparation, die Strukturanalysen meiner Probenserien, sowie für die vielen aufschlussreichen Gespräche.

... meinen Eltern, dass sie mir diese Ausbildung ermöglicht haben und immer für mich da waren.

... vor allem meiner Frau, die mich stets mit Geduld und Einfühlungsvermögen unterstützt und wieder aufgebaut hat.

Diese Arbeit wurde vom Fonds zur Förderung der wissenschaftlichen Forschung FWF durch die Projekte P16370 und P19165-N16 unterstützt.

Contents

Introduction	3
1 Theoretical aspects	5
1.1 Transport Phenomena	5
1.1.1 Electrical resistivity	7
1.1.2 Thermal conductivity	12
1.1.3 Thermopower	17
1.2 Thermoelectric energy conversion, the figure of merit	19
2 Experimental techniques	23
2.1 Sample preparation	23
2.2 Structure analysis	23
2.3 Electrical resistivity measurements	24
2.4 Thermal conductivity	25
2.5 Thermopower	28
3 The CePd₃ system	30
3.1 CePd ₃ sample series	33
3.2 CePd ₃ B _y	35
3.2.1 Electrical resistivity	37
3.2.2 Thermopower	38
3.2.3 Thermal conductivity	40
3.2.4 Figure of merit	47
3.3 Ce(Pd _{1-x} Rh _x) ₃	47
3.3.1 Electrical resistivity	48
3.3.2 Thermopower	51
3.3.3 Thermal conductivity	55
3.3.4 Figure of merit	59
3.4 Ce(Pd _{1-x} Rh _x) ₃ B _{0.05}	60
3.4.1 Electrical resistivity	62
3.4.2 Thermopower	64
3.4.3 Thermal conductivity	68
3.4.4 Figure of merit	70

3.5	Ce(Pd _{0.94-x} Rh _x Ag _{0.06}) ₃	72
3.5.1	Electrical resistivity	74
3.5.2	Thermopower	74
3.5.3	Thermal conductivity	76
3.5.4	Figure of merit	79
3.6	Summary	79
Conclusion		90
A Fitting procedure		92
A.1	Electrical resistivity $\rho(T)$	92
A.2	Seebeck coefficient $S(T)$	93
A.3	Thermal conductivity $\lambda(T)$	94
List of publications		103
List of conference contributions		106

Introduction

Thermoelectricity is the ability of materials to directly convert thermal energy into electrical energy or the other way around enabled by the Seebeck effect (1821) [1] and the Peltier effect (1834) [2], respectively. Benefits due to the lack of moving parts are e.g., simplicity, reliability, soundless and vibration less operation. In reasonable applications these benefits counterweigh the disadvantages of high cost and low efficiency. Examples for products which are already on the market are e.g. camping coolers, spot cooling of electronics or infrared detector cooling. A target for application is the waste heat conversion of e.g. the engine of a car into electrical energy, to increase the efficiency. The potential of a material for thermoelectric application is determined by the dimensionless figure of merit ZT , given by the product of the square of the Seebeck coefficient $S(T)$ and the temperature T divided by the product of electrical resistivity and thermal conductivity, $\rho(T)$ and $\lambda(T)$, respectively ($ZT = S^2T/\rho\lambda$).

CePd₃ is a long known intermetallic system, which crystallizes in the simple AuCu₃-structure. The transport properties of CePd₃ show many features which are still not understood. Although the crystal structure tolerates differing stoichiometry due to a wide stability region in the phase diagram, the electronic structure is very sensitive to smallest off-stoichiometry and impurities as demonstrated by M.J. Besnus et al. (1983) [3]. In 1973 it was already found, that the thermoelectric figure of merit of this material is anomalously large [4] and a survey of the effect of substitution with Rh on the electronic state of Ce was published even 1972 [5]. But 30 years later still no systematic substitution study with respect to the figure of merit has been published. The extraordinary high thermopower of CePd₃ is a consequence of strong Kondo interaction due to an intense 4f-s,p,d hybridization which is the driving parameter of the Ce valency. However the effect of substitution and doping on the Ce valency has been discussed in papers for a variety of compositions (see e.g. [6, 7, 8]). With a substitution of Pd by Rh the Ce valency can be shifted toward 4+, while Ag substitution tunes the valency toward 3+. Doping the interstitial 1b site of CePd₃ with elements like B, Si, Ga, In . . . also leads to a decrease of the Ce valency [9, 10] toward 3+. For an improvement of the thermoelectric figure of merit ZT

of CePd_3 an increase of thermopower $S(T)$ with a simultaneous decrease of the electrical resistivity $\rho(T)$ and the thermal conductivity $\lambda(T)$ would be preferable. In the year 1982 H. Stihoul et al. [11] published thermopower and resistivity data for $\text{Ce}(\text{Pd}_{1-x}\text{Rh}_x)_3$ and $\text{Ce}(\text{Pd}_{1-z}\text{Ag}_z)_3$ -series which show for $x=0.08$ a general increase of $S(T)$ with concurrent decrease of $\rho(T)$, while an increasing z shows rather unfavorable $S(T)$ and $\rho(T)$ -curves in terms of thermoelectricity. M. Houshiar et al. [12] have presented thermopower and resistivity data for CePd_3B_y , which also loses thermoelectric performance with increasing B content. In the scope of this thesis the material series CePd_3B_y , $\text{Ce}(\text{Pd}_{1-x}\text{Rh}_x)_3$, $\text{Ce}(\text{Pd}_{1-x}\text{Rh}_x)_3\text{B}_{0.05}$ and $\text{Ce}(\text{Pd}_{0.94-x}\text{Rh}_x\text{Ag}_{0.06})_3$ have been synthesized and their thermoelectric properties have been measured and analyzed by using models, which are common in literature. The applicability of different models is discussed and extracted fit-parameters are presented. In the first chapter of this thesis a survey on the theoretical background is given. The experimental setup and techniques used for data acquisition are described in chapter two. In chapter three the CePd_3 system is specified and the measured data for the different sample series are analyzed. In the summary the main results are outlined and in the Appendix a detailed description of the fitting procedure is given.

Chapter 1

Theoretical aspects

1.1 Transport Phenomena

The most important transport coefficients discussed in this thesis are the *electrical resistivity* ρ , the *thermal conductivity* λ and the *Seebeck coefficient* S . While ρ is defined as the ratio of the electrical field \vec{E} to the parallel current density \vec{I} without any temperature gradient, λ is the negative ratio of the heat flux density \vec{J} to a temperature gradient in the same direction with the boundary condition of $\vec{E} = 0$.

$$\vec{E} = \rho\vec{I} \quad \text{and} \quad \vec{J} = -\lambda\text{grad}T. \quad (1.1)$$

S , is an unique material specific constant, but its macroscopic effect can only be observed in an open circuit consisting of at least two different materials, where on the material junctions a temperature gradient is applied and as a consequence an electrical field \vec{E} is established (compare Fig. 1.1 and Eqn. 1.2)[1]. It is also possible to create a temperature gradient by applying an electric current, due to the *Peltier effect* [2]. The Peltier coefficient Π , which is related directly to S , shown in Eqn. 1.3, is the ratio of the heat exchange \vec{Q} to the current density \vec{I} .

$$\vec{E} = S\text{grad}T \quad \text{and} \quad \vec{Q} = \Pi\vec{I} \quad (1.2)$$

$$\Pi = ST \quad (1.3)$$

Using the definition 1.2 in a setup like that in Fig. 1.1 results in

$$S_{AB} = \lim_{\Delta T \rightarrow 0} \left(\frac{\Delta V}{\Delta T} \right), \quad (1.4)$$

where S_{AB} is the difference of S_A and S_B , the absolute Seebeck coefficients of material A and B , respectively. Equivalent considerations hold for Π_{AB} .

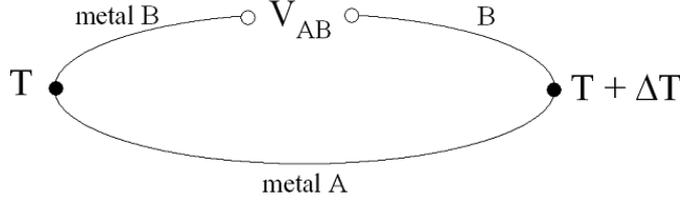


Figure 1.1: Thermoelectric circuit

Theoretically the transport coefficients like ρ , λ and S can be derived, in terms of the *linearized Boltzmann equation*,

$$\left(\frac{\partial}{\partial t} + \dot{\vec{r}} \cdot \nabla_r + \vec{k} \cdot \nabla_k \right) f(\nu, \vec{r}, t) = \left(\frac{\partial f(\nu, \vec{r}, t)}{\partial t} \right)_{coll} \quad (1.5)$$

which describes a dynamic equilibrium by connecting a collision term, represented by the right side of Eqn. 1.5 to a field term expressed by its left side. $f(\nu, \vec{r}, t)$ is the distribution function of a conduction electron dependent on the position \vec{r} and the wave vector \vec{k} , which is included into the quantum number ν as well as the band index and the spin direction. For a free electron gas in equilibrium, this function equals the *Fermi-Dirac distribution*

$$f_0(\varepsilon_\nu) = \left[\exp \frac{\varepsilon_\nu - \mu}{k_B T} + 1 \right]^{-1}, \quad (1.6)$$

which describes the occupation of electronic states as a function of temperature. ε_ν denotes the energy of the electrons corresponding to ν and $k_B = 1.381 \times 10^{-23}$ J/K is the Boltzmann constant. At $T = 0$ the chemical potential μ equals the Fermi energy E_F . Only electrons in the proximity of the Fermi energy can contribute to transport of charge, mass and thus energy. This electron movement is restricted by different scattering centers like impurities, lattice imperfections, phonons, magnetic moments and even electron-electron scattering itself. The simplest way to solve the linearized Boltzmann equation (Eqn. 1.5) is the *relaxation time approximation*

$$\left(\frac{\partial f(\nu)}{\partial t} \right)_{coll} = \frac{f(\nu) - f_0(\varepsilon_\nu)}{\tau_\nu}. \quad (1.7)$$

It is assumed that the perturbed distribution function $f(\nu)$ relaxes exponentially toward the equilibrium $f_0(\varepsilon_\nu)$ with τ_ν is the half-life or relaxation-time. Each scattering mechanism has a corresponding τ_i and if they are independent, they can be combined to an average τ using *Matthiessen's rule*

$$\tau^{-1} = \sum \tau_i^{-1}. \quad (1.8)$$

A further assumption uses a parabolic conduction band containing only one type of charge carrier and the interaction between charge carriers and phonons does not disturb the charge carrier distribution function. Then, transport quantities can be deduced from the linearized Boltzmann equation (Eqn. 1.5), resulting in following expressions:

$$\rho = \frac{1}{K_0} \frac{T}{e^2}, \quad (1.9)$$

$$S = \pm \frac{1}{eT} \left(\mu - \frac{K_1}{K_0} \right) \quad (1.10)$$

$$\lambda_e = \frac{1}{T^2} \left(K_2 - \frac{K_1^2}{K_0} \right). \quad (1.11)$$

The sign of S depends on the type of charge carriers as illustrated by \pm in Eqn. 1.10 accounting for electrons or holes as primary charge carriers. λ_e is the electronic thermal conductivity and e is the electronic charge. The transport integrals K_n are given by

$$K_n = \frac{k_F^3}{3\pi^2 m} \int \epsilon_k^n \tau(\epsilon_k) d\epsilon_k \left(-\frac{df_k}{d\epsilon} \right) \quad (1.12)$$

Once, the relaxation time is known for a particular interaction process, all the transport coefficients can be calculated.

1.1.1 Electrical resistivity

According to Matthiessen's rule (Eqn. 1.8) the electrical resistivity $\rho(T)$ can be written as a sum its basic components,

$$\rho(T) = \rho_0 + \rho_{ph}(T) + \rho_{e-e} + \rho_{mag}(T). \quad (1.13)$$

ρ_0 represents the elastic potential scattering of charge carriers by impurities, lattice imperfections or grain boundaries, ρ_{ph} denotes scattering of conduction electrons by lattice vibrations, ρ_{e-e} denotes scattering of conduction electrons by electrons and ρ_{mag} represents the contribution due to scattering of the charge carrier on magnetic moments.

While ρ_0 is independent on temperature (up to temperatures where diffusion processes start), the temperature dependence of ρ_{ph} is described by the *Bloch-Grüneisen formula* (Eqn. 1.14), which is the result of a variational type calculation in the scope of Boltzmann equation (Eqn. 1.5) assuming a spherical Fermi surface and neglecting Umklapp processes [13, 14].

$$\rho_{ph} = \frac{c_{BG}}{\Theta_D} \left(\frac{T}{\Theta_D} \right)^5 \int_0^{\Theta_D/T} \frac{x^5 dz}{(e^x - 1)(1 - e^{-x})}. \quad (1.14)$$

c_{BG} denotes a material dependent electron-phonon interaction constant, which is temperature independent. Θ_D is the Debye temperature and $x = \frac{\hbar\omega}{k_B T}$. Low ($T \ll \Theta_D$) and high temperature ($T \gg \Theta_D$) approximations of Eqn. 1.14 yield

$$\rho_{ph} \propto T^5 \quad \text{and} \quad \rho_{ph} \propto T, \quad (1.15)$$

respectively. For ρ_{e-e} an empirical law was first introduced by L. Landau and I. Pomeranchuk [15] to describe the electron-electron scattering at lowest temperatures.

$$\rho_{e-e} = AT^2 \quad (1.16)$$

The material dependent scaling parameter A can differ a lot. For simple metals it is about $1 \text{ f}\Omega\text{m}/\text{K}^2$ (e.g. for K it is $2.2 \text{ f}\Omega\text{m}/\text{K}^2$ [16]), but for heavy fermion compounds, this parameter can grow due to the enhanced effective mass of the charge carriers and reaches values of e.g. $23.5 \text{ n}\Omega\text{m}/\text{K}^2$ for CePt₃Si [17]. This emphasized T^2 -behavior is known as a crucial prove for systems to be a Fermi-liquid.

Considering only the paramagnetic state, without crystal electric field (CEF) splitting and any short range correlations. Then, ρ_{mag} is a temperature independent constant and can be expressed within a perturbation type calculation in the scope of the Heisenberg model as

$$\rho_{mag} = \frac{3\pi N m^*}{2\hbar e^2 E_F} |\Gamma|^2 (g-1)^2 J(J+1). \quad (1.17)$$

N means the number of magnetic moments in the unit cell, E_F is the Fermi energy and Γ is the exchange interaction constant between charge carriers and localized magnetic moments. $(g-1)^2 J(J+1)$ is the *de Gennes factor* with J referring to the total angular moment of the magnetic ion and g is the *Landé - factor*.

Crystal Electric Field (CEF)

The CEF is originated by the charge distribution around a magnetic ion and contributes to its potential energy by at least partly lifting the rotational degeneracy of the free ion multiplet according to the values of the projections of the total angular momentum J . This contribution is described by

$$V_{CEF}(\vec{r}) = \int \frac{\rho(\vec{R})}{|\vec{r} - \vec{R}|} d^3 R, \quad (1.18)$$

where $\rho(R)$ denotes the charge density of the surrounding electrons and nuclei. It is a solution of Laplace's equation and can be expanded in terms of spherical

harmonics, assuming that the ions carry only point charges. The results can be used in a Hamiltonian for the CEF written as

$$H_{CEF}(\vec{r}) = \sum_{l,m} A_l^m H_{lm} \quad (1.19)$$

with

$$A_l^m = \frac{4\pi}{2l+1} \int d^3R \frac{\rho(R) Y_l^{m*}(\Omega_R)}{R^{l+1}} \quad (1.20)$$

and

$$H_{lm} = \sum_{m=-l}^l r^l Y_l^m(\delta_i, \phi_i) \quad (1.21)$$

Stevens [18] showed by applying the Wigner-Eckhardt-theorem, that the matrix elements of H_{CEF} are proportional to those of equivalent operators which are defined by simple angular momentum operators J_z or J_{\pm} . Using this so called Stevens operators $O_n^m(J)$ and the rewritten crystal field parameters A_l^m

$$B_n^m = \sum_{n,m} A_n^m \langle r_{4f}^n \rangle \Theta_n \quad (1.22)$$

$$\Theta_n = \begin{cases} \alpha_j & \dots & n = 2 \\ \beta_j & \dots & n = 4 \\ \gamma_j & \dots & n = 6 \end{cases} \quad (1.23)$$

the crystal electric field Hamiltonian in its simplest form can be written as follows

$$H_{CEF} = \sum_{n,m} B_n^m O_n^m. \quad (1.24)$$

The B_n^m are usually determined experimentally and the operator equivalents are tabulated as functions of J operators and can be found in literature, e.g. [19].

The number of non-vanishing terms in H_{CEF} is generally strongly restricted by the local symmetry. For cubic point group symmetry the appropriate configuration is

$$H_{cub} = B_4^0(O_4^0 + 5O_4^4) + B_6^0(O_6^0 - 21O_6^4), \quad (1.25)$$

while for a hexagonal symmetry the following is the correct operator

$$H_{hex} = B_2^0 O_2^0 + B_4^0 O_4^0 + B_6^0 O_6^0 + B_6^6 O_6^6. \quad (1.26)$$

If CEF-splitting lifts the $(2J+1)$ -fold degeneracy of the ground state and excited levels are thermally populated, Eqn. 1.17 has to be modified as follows:

$$\rho_{mag} = \frac{3\pi N m^*}{2\hbar e^2 E_F} |\Gamma|^2 (g-1)^2 \sum_{m_s, m'_s, i, i'} \langle m'_s i' | \vec{s} \vec{J} | m_s i \rangle^2 p_i f_{ii'} \quad (1.27)$$

With m_s and m'_s correspond to the spins of the charge carriers in initial and final state i and i' . The relative population of CEF-levels with different energy E_i is determined by a *Boltzmann distribution*

$$p_i = \frac{e^{E_i/k_B T}}{\sum_j e^{-E_j/k_B T}} \quad (1.28)$$

The coefficients $f_{ii'}$ are defined as

$$f_{ii'} = \frac{2}{1 + e^{-(E_i - E_{i'})/k_B T}}. \quad (1.29)$$

As a consequence the paramagnetic contribution to $\rho(T)$ is not temperature independent anymore.

Also for long range magnetic ordered states different dependencies for $\rho_{mag}(T)$ have to be considered. While a T^2 behavior is related to ferromagnetism, a T^4 dependence is frequently found for antiferromagnetic materials at $T \ll T_{ord}$.

Kondo effect

Another important magnetic scattering mechanism is the *Kondo effect*, caused by second order scattering of conduction band electrons by non-interacting isolated magnetic moments. This can be realized by magnetic impurities e.g. Mn or Fe dissolved in a host metal like Cu or by compounds containing rare earth elements or actinides. Because the 4f- and 5f-shells are smaller than the d-orbitals, they are shielded and therefore isolated. Such materials are called *Kondo lattices* because the magnetic ions sit on regular lattice sites. The first theoretical explanation of such scattering processes was given by J. Kondo [20] using the Heisenberg s-d model:

$$H = -\mathcal{J} \vec{\sigma} \cdot \vec{S} \quad (1.30)$$

The exchange integral \mathcal{J} is assumed to be constant. Kondo found that using a negative J (i.e., antiferromagnetic exchange) and taking a two stage scattering process into account, a minimum in $\rho(T)$ of compounds with magnetic impurities can be explained. In the first stage an electron is scattered by the magnetic impurity and both stay in an intermediate state. A second scattering event restores the original state of the impurity and the electron is driven to its final state. The transition probability $W_{a \rightarrow b}$ from the initial state a

via the intermediate state c to the final state b can be described theoretically using the second Born approximation, where V_{ij} is the scattering potential between the states i and j .

$$W_{a \rightarrow b} = \frac{2\pi}{\hbar} \left(V_{ab}V_{ba} + \sum_{c \neq a} \frac{V_{ab}V_{bc}V_{ca}}{E_a - E_c} + c.c. \right). \quad (1.31)$$

The first term within the brackets is the first Born approximation, yielding a temperature independent scattering, while the summation inherits the nature of the unusual scattering. The energy E_a equals E_b but is different from E_c . If during the first scattering a spin flip of the electron and the impurity takes place, which is compensated with the second scattering event, the magnetic ion can have an intermediate spin state $m'_s = m_s + 1$ or $m'_s = m_s - 1$. These different intermediate states have different probabilities and energies. As a consequence, the electrical resistivity becomes temperature dependent and exhibits a logarithmic contribution. Calculations end up in

$$\rho_{imp} = \frac{3\pi m \mathcal{J}^2 S(S+1)}{2e^2 \hbar E_F} \left[1 - 4\mathcal{J}N(E_F) \ln \left(\frac{k_B T}{D} \right) \right] \quad (1.32)$$

D is a cut-off parameter and exchange coupling is assumed to be negative, i.e. antiferromagnetic ($\mathcal{J} < 0$). For intermediate valence compounds the relation $k_B T_K \gg \Delta_{CEF}$ is fulfilled, therefore the ground state degeneracy N_f reaches its maximum. In such a case the CEF split levels are strongly hybridized and individual levels can no longer be distinguished. As a result the individual peaks in neutron diffraction data are smeared out and a broad maximum with $\Gamma/2 \approx T_K$ remains. For Ce-compounds this leads to $N_f = 2J + 1 = 6$. Due to a valence shift toward 3+, however, T_K decreases and the ground state of a $J = \frac{5}{2}$ cubic system is split into a doublet and a quartet.

4f-contribution to $\rho(T)$: An empirical model

A. Freimuth [21] showed an empirical expression to describe the enhanced resistivity due to an unstable 4f-shell. The fluctuation temperature T_f which is proportional to T_K is correlated to the quasielastic linewidth Γ_{QE} of the neutron spectra by $\Gamma_{QE} = k_B T_f$ and for mixed valence compounds like CePd₃ it is independent of temperature in contrast to heavy Fermion compounds where T_f may be approximated by $T_f = k_1 + k_2 * \sqrt{T}$. Using a temperature dependent effective scattering width $W(T)$ and the temperature T_0 which is interpreted as energy difference between the energy of the "f-band" (e_f) and the Fermi energy E_f ($k_B T_0 = (e_f - E_f)$) the expression of the resistivity reads:

$$W(T) = T_f \exp(-T_f/T) \quad (1.33)$$

$$\rho_f(T) = bJ_{sf}^2 \frac{W(T)}{T_0^2 + W(T)^2} \quad (1.34)$$

The parameter b follows from comparison of the Drude-formula leading to $b = m^*k_B/ne^2\hbar$ with m^* is the effective mass and n is the charge carrier concentration. J_{sf} is interpreted as hybridization integral taking the overlap of the sd- and the f-wavefunctions into account.

1.1.2 Thermal conductivity

The total thermal conductivity of solids is the sum of an electronic contribution λ_e and a phonon part λ_{ph} .

$$\lambda_{tot} = \lambda_e + \lambda_{ph} \quad (1.35)$$

In a first approximation each contribution to the thermal resistivity W_i can be separated according to Matthiessen's rule (Eqn. 1.8). The electronic thermal resistivity W_e is similar to the electrical resistivity and consists of different contributions due to impurity scattering, electron phonon scattering and electron magnon scattering, $W_{e,0}$, $W_{e,ph}$ and $W_{e,mag}$, respectively.

$$W_e \equiv \lambda_e^{-1} = W_{e,0} + W_{e,ph} + W_{e,mag} \quad (1.36)$$

The electronic part of the thermal conductivity is related to the electrical resistivity via the *Wiedemann-Franz law*, i.e.,

$$\lambda_e = L_0\sigma T. \quad (1.37)$$

$L_0 = \frac{\pi^2}{3} \left(\frac{k_B}{e}\right)^2 = 2.45 \times 10^{-8} \text{ W}\Omega\text{K}^{-2}$ is the Lorenz number, and the electrical conductivity $\sigma \equiv \rho^{-1}$. For real metals the Lorenz number is temperature dependent and defined as $L_e = \frac{\lambda_e}{\sigma T}$. But for $T > \frac{\theta_D}{2}$, L_e normally does not deviate more than 20% from L_0 .

For more accuracy one can treat $W_{e,0}$ and $W_{e,ph}$ separately. $W_{e,0}$ can simply be expressed by applying the Wiedemann Franz law (Eqn. 1.37) to the residual resistivity.

$$W_{e,0} = \frac{\rho_0}{L_0 T} \quad (1.38)$$

$W_{e,ph}$ caused by electron scattering on phonons can be deduced similarly to the Bloch-Grüneisen equation 1.14 and is known as *Wilson equation* [22].

$$W_{e,ph} = \frac{4R}{L_0 T} \left(\frac{T}{\theta_D}\right)^5 \left\{ \left[1 + \frac{3}{\pi^2} \left(\frac{k_F}{q_D}\right)^2 \left(\frac{\theta_D}{T}\right)^2 \right] J_5(\theta_D/T) - \frac{1}{2\pi^2} J_7(\theta_D/T) \right\} \quad (1.39)$$

R is a material dependent constant, k_F is the wave vector at the Fermi energy and q_D is defined by the dispersion relation $q_D = \frac{\omega_D}{\nu_s}$ with ω_D is the Debye frequency and ν_s is the velocity of sound. The *Debye-integrals* are

$$J_n(x) = \int_0^x \frac{z^n dz}{(e^z - 1)(1 - e^{-z})} \quad \text{with} \quad z = \frac{\theta_D}{T} \quad (1.40)$$

The first term of Wilson's equation (Eqn. 1.39) describes *horizontal* scattering processes, which determines also the electrical resistivity. The second term accounts for *vertical* scattering processes which do not affect the electrical resistivity. The last term weighs both contributions. Similar to the Bloch-Grüneisen law for Wilson's equation, simple high and low T approximations exist which are:

$$W_{e,ph}(T) \approx \frac{R}{L_0 \Theta_D} = \text{const.} \quad \text{for} \quad T \gg \Theta_D \quad (1.41)$$

and

$$W_{e,ph}(T) \approx \text{const.} \left(\frac{124.4}{\Theta_D} \right)^3 T^2 \quad \text{for} \quad T \ll \Theta_D \quad (1.42)$$

In analogy to Eqn. 1.17 there exists an additional paramagnetic term which can be expressed as

$$W_{\text{mag}} = \frac{9m^* N}{2\pi \hbar k_B^2 E_F} |\mathcal{J}|^2 (g-1)^2 J(J+1) \frac{1}{T}. \quad (1.43)$$

For the lattice contribution to thermal conductivity, λ_{ph} J. Callaway [23] proposed a model based on the relaxation time approximation, taking a scattering time τ_c into account which consists of different contributions τ_i , which are assumed to be independent from each other and thus can be summed up according to the Matthiesens rule (Eqn. 1.8). τ_N stands for normal three phonon scattering processes, τ_D , τ_B , τ_U and τ_{ph-el} denote point defect scattering, boundary scattering, Umklapp processes and scattering of phonons by electrons, respectively which depend on T and $x = \hbar\omega/k_B T$.

$$\tau_c^{-1} = \tau_N^{-1} + \tau_U^{-1} + \tau_D^{-1} + \tau_B^{-1} + \tau_{ph-el}^{-1} \quad (1.44)$$

$$\lambda_{ph} = \frac{k_B}{2\pi^2 \nu_s} \left(\frac{k_B T}{\hbar} \right)^3 \left[\int_0^{\Theta_D/T} \tau_c \frac{x^4 e^x}{(e^x - 1)^2} dx + \frac{I_2}{I_1} \right] \quad (1.45)$$

with ν_s standing for the velocity of sound and I_1 and I_2 abbreviating the integrals,

$$I_1 = \int_0^{\Theta_D/T} \frac{\tau_c}{\tau_N} \frac{x^4 e^x}{(e^x - 1)^2} dx \quad \text{and} \\ I_2 = \int_0^{\Theta_D/T} \frac{1}{\tau_N} \left(1 - \frac{\tau_c}{\tau_N} \right) \frac{x^4 e^x}{(e^x - 1)^2} dx \quad (1.46)$$

respectively. The first term within the squared brackets of equation 1.45 is usually a good approximation for the lattice thermal conductivity as long as normal three-phonon interactions are negligible. With increasing τ_N the term I_1/I_2 must be taken into account. For interpretation of the experimental data this formulae are put together like it is shown in the appendix section A.3 and the ν_s is replaced by its equivalent using Debye theory.

$$\nu_s = \omega_D \left(6\pi^2 \frac{N}{V} \right)^{-\frac{1}{3}} \quad (1.47)$$

The temperature and ω -dependence of the different scattering mechanisms has been discussed in various papers and textbooks. For point defect and boundary scattering the calculated terms are the same but for τ_U and τ_{ph-el} the estimations differ a lot. P.G. Klemens [24] calculates τ_U in the low temperature limit ($T \ll \theta_D$) as

$$\tau_U^{-1} \propto \omega^2 e^{-\frac{\theta_D}{2T}} \left[1 + 6 \frac{T}{\theta_D} + 24 \left(\frac{T}{\theta_D} \right)^2 + 48 \left(\frac{T}{\theta_D} \right)^3 \right]. \quad (1.48)$$

M.G. Holland gives a summary of different estimations for τ_U in Ref. [25] and G.A. Slack et al. [26] proposed an empirical approach writing

$$\tau_U^{-1} \propto \omega^\alpha \left(\frac{T}{\theta_D} \right)^\beta e^{-\frac{\theta_D}{bT}} \quad (1.49)$$

and use $\alpha = 2, \beta = 1$ and $b = 3$ for their fitting, which should be a working approximation for $T \geq \theta_D$. Additional a variety of estimations can be found in articles and books by J.M. Ziman, R.Berman and J.E. Parrott [27, 28, 29].

For the scattering of phonons by electrons especially for valence fluctuations I.A. Smirnov et al. [30] introduced a relaxation time as follows,

$$\tau_{ph-el}^{-1} = \frac{U_0^2 m^{*2}}{2\pi \hbar^3 \rho^*} k \quad (1.50)$$

where U_0 is the deformation potential, ρ^* the material density and k is the phonon wave vector. On the bases of this formula J. Kitagawa et al. as well as Y. Aoki et al. [31, 32] assumed $\tau_{ph-el}^{-1} \propto T x$ ($k = \omega/\nu_s \propto T x$). In a recent article of J. Yang [33] a theoretical foundation of the scattering of phonons by electrons is presented. Referring to Ziman [34, 35] he specified a relaxation time for the scattering of phonons by conduction electrons:

$$\begin{aligned} \tau_{ph-el}^{-1} &= \frac{\epsilon^2 m^{*3} \nu_s}{4\pi \hbar^4 d} \left(\frac{2k_B T}{m^* \nu_s^2} \right) \left\{ \frac{\hbar \omega}{k_B T} - \ln[\Psi] \right\} \\ \Psi &= \frac{1 + \exp[(\frac{1}{2} m^* \nu_s^2 - E_F)/k_B T + \hbar^2 \omega^2 / 8 m^* \nu_s^2 k_B T + \hbar \omega / 2 k_B T]}{1 + \exp[(\frac{1}{2} m^* \nu_s^2 - E_F)/k_B T + \hbar^2 \omega^2 / 8 m^* \nu_s^2 k_B T - \hbar \omega / 2 k_B T]} \end{aligned} \quad (1.51)$$

where ϵ is the electron-phonon interaction constant or deformation potential and d is the mass density. Comparing Eqn. 1.50 and Eqn. 1.52 they are identities despite the $\ln[\Psi]$ -term, which can be neglected for elevated temperatures. An other expression for the scattering of phonons by electrons in a bound state is presented in a paper of Griffin and Carruthers [36].

$$\tau_{ph-el}^{-1} = \frac{G\omega^4}{[\omega^2 - (4\Delta/\hbar)^2]^2 [1 + r_0^2\omega^2/4\nu_s^2]^8} \quad (1.52)$$

where G is a proportionality constant containing the number of scattering centers, Δ is the chemical shift related to the splitting of the electronic states and r_0 is the mean radius of the localized state. It has to be emphasized that these formulae are based on the adiabatic principle and perturbation theory. Ziman has argued that this is only valid if the mean free path of the electrons L_e is longer than the wave length $L_p = 2\pi/k$ of the phonon it scatters ($kL_e > 1$). Pippard [37] developed a model to describe the ultrasonic attenuation in metals and found relaxation times over the whole range of kL_e .

$$\tau_{ph-el}^{-1} = \frac{4nm^*v_FL_e\omega^2}{15d\nu_s^2} \quad \text{for } kL_e \ll 1 \quad (1.53)$$

$$\tau_{ph-el}^{-1} = \frac{\pi nm^*v_F\omega}{6d\nu_s} \quad \text{for } kL_e \gg 1 \quad (1.54)$$

One can see that all models result in a dependence of $\tau_{ph-el}^{-1} \propto w$ for $kL_e \ll 1$. For $kL_e \gg 1$ the $\tau_{ph-el}^{-1} \propto w^2$. According to [30, 31, 32] we assume that the first condition is fulfilled. Thus, in this thesis the following terms will be used to account for the different scattering mechanisms.

$$\tau_U^{-1} = AT^3x^2e^{-\frac{\theta_D}{3T}} \quad (1.55)$$

$$\tau_D^{-1} = Dx^4T^4 \quad (1.56)$$

$$\tau_B^{-1} = B \quad (1.57)$$

$$\tau_{ph-el}^{-1} = CTx \quad (1.58)$$

The single scattering contributions to the phonon part of the thermal conductivity and resistivity are mapped in the right and the left panel of Fig.1.2, respectively. θ_D is assumed to be 220 K and the scattering constants were chosen corresponding to an average fit within this thesis. The single contribution due to point defect scattering can not be calculated by simply putting the other parameters zero, because this results in a diverging integral. It was extracted by inverting all results into resistances and subtracting the other curves from the total thermal lattice resistivity. At low temperatures this procedure may lead to large errors due to the numerical cut off and therefore leads to artificial features in the curve, but generally it may give a clue

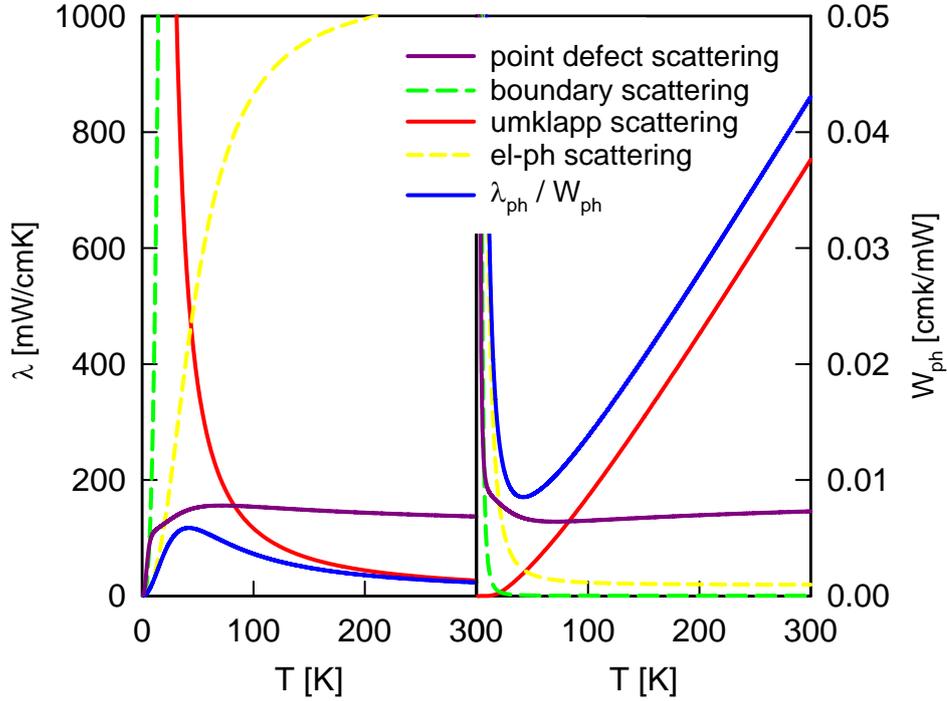


Figure 1.2: The left diagram shows the different scattering contributions as delimiters of λ_{ph} . The right panel maps the corresponding values in terms of thermal resistances.

how τ_D effects λ_{ph} . Modifying a theory by A. Einstein [38], D. G. Cahill and R. O. Pohl [39] found an expression for a minimal thermal conductivity not distinguishing between longitudinal and transverse acoustic phonon modes, which is written as

$$\lambda_{min} = \left(\frac{3n}{4\pi}\right)^{\frac{1}{3}} \frac{k_B^2 T^2}{\hbar \theta_D} \int_0^{\theta_D/T} \frac{x^3 e^x}{(e^x - 1)^2} dx \quad (1.59)$$

where $n = N/V$ is the number of atoms per unit volume. This expression is a lower limit of λ_{ph} , which is achieved by glass-like or amorphous systems especially at high temperatures.

Other possible contributions to the thermal conductivity are the so called "rattling modes", which are resonant scattering processes of the phonons by localized modes of loose bound atoms within the crystal-structure (e.g rare earth atoms in cage-compounds like Clathrates or Skutterudites). Such processes are defined by an Einstein temperature θ_E and a damping factor α . M. Wagner [40] introduced an analytical expression for the according relaxation time which was used by C.T. Walker and R.O. Pohl [41] to describe their experimental data.

$$\begin{aligned}
\tau_{rattle}^{-1} &= Ef(x, T)g(x, T) & (1.60) \\
f(x, T) &= \frac{\left(\frac{k_B\theta_E}{\hbar}\right)^2 \left(1 - \frac{Tx}{\theta_E}\right)^2 e^{\left(\frac{\theta_E}{T} - x\right)} (e^{x-1})}{\left(e^{\frac{\theta_E}{T}} - 1\right) \left[e^{\left(\frac{\theta_E}{T} - x\right)} - 1\right]} \\
g(x, T) &= \left(1 + \frac{4\alpha\nu_s\hbar}{k_B\theta_E}\right) \ln \left[1 + \frac{\frac{Tx}{\theta_E} \left(1 - \frac{Tx}{\theta_E}\right)}{\frac{4\alpha\nu_s\hbar}{k_B\theta_E}}\right] - 4 \left[\frac{Tx}{\theta_E} \left(1 - \frac{Tx}{\theta_E}\right)\right]
\end{aligned}$$

A fit function taking into account the rattling modes is also presented in appendix section A.3.

1.1.3 Thermopower

In the scope of a relaxation time approximation using the linearized Boltzmann equation, as for ρ and λ a general expression for the Seebeck effect can be written as

$$S = \frac{1}{eT} \frac{\int_0^\infty \sigma(E)(E - E_F) \frac{df_0}{dE} dE}{\int_0^\infty \sigma(E) \frac{df_0}{dE} dE} \quad (1.61)$$

$\sigma(E)$ is the energy dependent electrical conductivity, E_F is the Fermi energy and $\frac{df_0}{dE}$ is the slope of the electronic density of states (DOS). In general the total Seebeck coefficient of a metal is the sum of different contributions, which are the diffusion term S_e , originated by the movement of electrons due to a temperature gradient, the phonon-drag term S_{ph} , which represents the electron drag due to phonons and finally S_{mag} , which is caused by the electron drag caused by magnons. Usually the drag terms are second order effects and are frequently neglected. In contrast to ρ and λ , for S_e the application of Matthiessen's rule is not possible. Nevertheless using a variational procedure it can finally be expressed by the *Kohler rule* (Eqn. 1.62), which correlates the product of S_e and the total electronic thermal resistivity W_e to the sum of $W_{e,i}$ and Seebeck coefficient $S_{e,i}$ over the particular scattering mechanisms i .

$$S_e W_e = \sum_i^n W_{e,i} S_{e,i} \quad (1.62)$$

Applying the Wiedemann-Franz law (Eqn. 1.37) to the Kohler rule results in the Nordheim-Gorter rule

$$S_e = \sum_i \frac{\rho_i}{\rho} S_{e,i}, \quad (1.63)$$

serving as a first approximation.

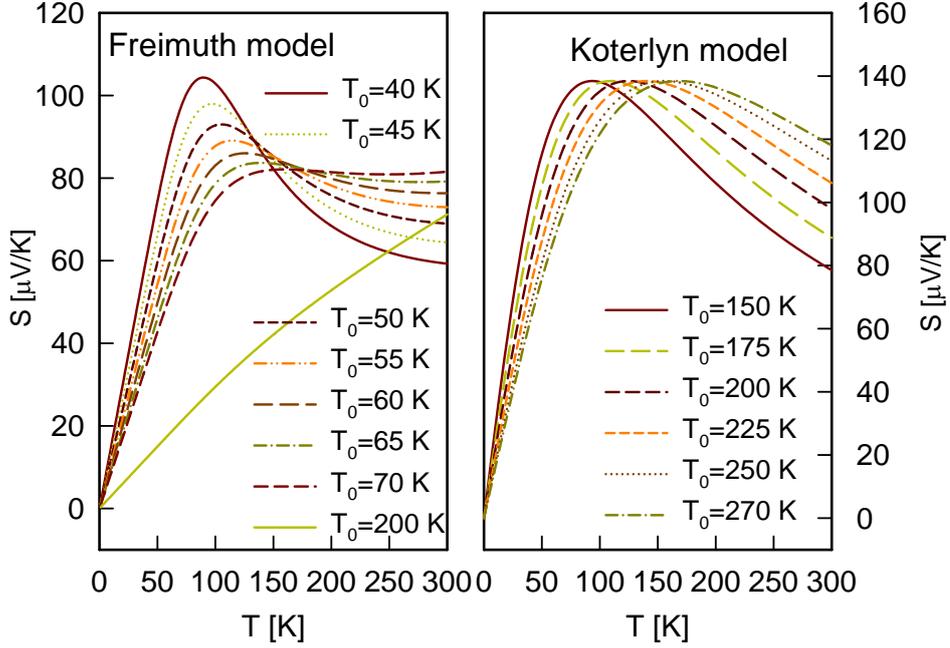


Figure 1.3: The diagrams show the dependence of the equations by Freimuth (Eqn.1.64) and Koterlyn (Eqn.1.65) model on T_0 , keeping the other parameters constant ($c_1 = 0, c_2 = 60, T_f = 200$ K and $N_f = 6$).

4f-contribution to $S(T)$: Empirical models

Together with the formula for resistivity (Eqn. 1.34) also an empirical formula for the 4f-contribution to the thermopower was introduced by Freimuth [21] bringing the temperature dependence into correlation with T_f and T_0 like follows

$$S_f(T) = c_1 * T + c_2 * \frac{TT_0}{T_0^2 + W(T)^2}. \quad (1.64)$$

c_1 and c_2 are material constants and $W(T)$ is explained as for the resistivity, compare Eqn. 1.33. An other approach was proposed by Koterlyn et al. [42]. Using the case of strong orbital degeneracy $N_F = 2J + 1 = 6$, which normally takes place for intermediate valent Ce, he obtained the temperature dependent thermopower as follows,

$$S_f(T) = \frac{2\pi^2 k_B}{3|e|} * \frac{TT_0}{\frac{\pi^2}{3}T^2 + (1 + \frac{\pi^2}{N_f^2})T_0^2}. \quad (1.65)$$

Although the models of Freimuth (Eqn. 1.64) and Koterlyn (Eqn. 1.65) look alike and produce also fit curves with same features, they result in varying fit-parameters which lead to different interpretation of the measured data.

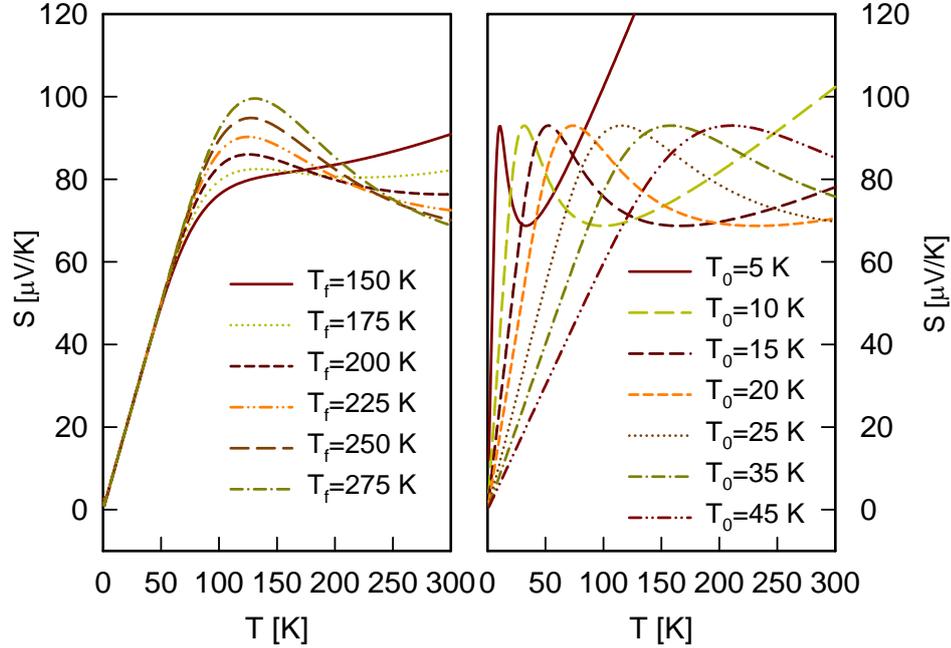


Figure 1.4: These diagrams show $S(T)$ -curves generated by using Eqn.1.64. While the left panel shows data for variable T_f keeping the other parameters constant ($c_1 = 0, c_2 = 60$ and $T_0 = 60$), the right panel shows curves for a constant ratio $T_f/T_0 = 4$ with variable T_0 ($c_1 = 0$ and $c_2 = 60$).

Figure 1.3 shows the drastic discrepancy between the two models with respect to the interpretation of T_0 . T_f is the second characteristic temperature which Freimuth uses for scaling and the effect of this parameter on the structure of $S(T)$ is denoted in the left panel of Fig.1.4, while the right panel shows the performance if the ratio T_f/T_0 is kept constant ($T_f/T_0 = 4$ which is about the ratio we get from a fit of CePd_3).

1.2 Thermoelectric energy conversion, the figure of merit

For the application of thermoelectric materials in heat pumps or for electric power generation, one has to consider terms like efficiency and performance. Detailed description and calculations can be found e.g. in Ref. [43, 44]. The most important facts will be treated here. In Fig.1.5 an idealized thermoelectric couple is schemed, which consists of a p-type (hole conductor with positive S) and an n-type (electron conductor with negative S) branch connected by idealized conductors with $\lambda(T) = S(T) = 0$. The branches are arranged in

an electric serial and a thermal parallel assembly. Neglecting thermal or electrical contact resistances between the branches and the connector material and also heat losses due to radiation and convection, the coefficient of performance for Peltier cooling can be obtained. First the heat flows $Q_{p,n}$ for each branch due to the Peltier effect (using equation 1.2 and 1.3) and the particular thermal conductivity $\lambda_{p,n}$ has to be taken into account, with $A_{p,n}$ denoting the cross section of each branch.

$$Q_p = S_p IT - \lambda_p A_p \frac{dT}{dx} \quad \text{and} \quad Q_n = -S_n IT - \lambda_n A_n \frac{dT}{dx} \quad (1.66)$$

The second term takes into account the Joules heat production due to the resistivity $\rho_{p,n}$, which produces a non constant thermal gradient.

$$-\lambda_{p,n} A_{p,n} \frac{d^2 T}{dx^2} = \frac{I^2 \rho_{p,n}}{A_{p,n}} \quad (1.67)$$

At this point all coefficients are assumed to be temperature independent. Applying the boundary conditions $T = T_H$ at the heat source ($x = 0$) and $T = T_C$ at the heat sink ($x = L_{p,n}$), equation 1.67 reads as

$$\lambda_{p,n} A_{p,n} \frac{dT}{dx} = -\frac{I^2 \rho_{p,n} (x - \frac{L_{p,n}}{2})}{A_{p,n}} + \frac{\lambda_{p,n} A_{p,n} \Delta T}{L_{p,n}} \quad (1.68)$$

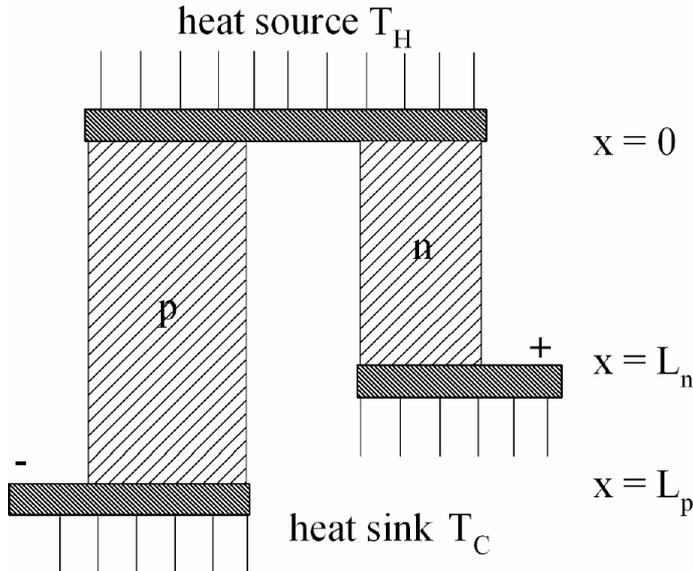


Figure 1.5: Thermocouple for heat pumping or power generation.

with $\Delta T = (T_H - T_C)$. The total heat flow from the heat source $Q_C = (Q_p + Q_n)|_{x=0}$, which is in fact the cooling power, can now be expressed by

$$Q_C = (S_p - S_n)IT_C - K\Delta T - \frac{I^2 R}{2}, \quad (1.69)$$

with the total thermal conductance K and the electrical resistance R

$$K = \frac{\lambda_p A_p}{L_p} + \frac{\lambda_n A_n}{L_n}, \quad R = \frac{L_p \rho_p}{A_p} + \frac{L_n \rho_n}{A_n}. \quad (1.70)$$

For $\frac{dQ_C}{dI} = 0$ the maximum cooling power is obtained corresponding to optimal current I_{max} .

$$Q_{C,max} = \frac{(S_p - S_n)^2 T_C^2}{2R} - K\Delta T \quad \text{and} \quad I_{max} = \frac{(S_p - S_n)T_C}{R} \quad (1.71)$$

For a positive cooling effect ΔT may not exceed the value limited by $Q_{C,max} \geq 0$. Using the definition

$$Z = \frac{(S_p - S_n)^2}{KR} \quad (1.72)$$

and Eqn. 1.71, the maximum achievable temperature gradient ΔT_{max} is given by

$$\Delta T_{max} = (T_H - T_C)_{max} = \frac{1}{2} Z T_C^2. \quad (1.73)$$

Z defined in Eqn. 1.72 is the property of a specific thermocouple taking into account the relative dimensions of the thermoelements. For material science an absolute definition would be preferable. To maximize the figure of merit in equation 1.72 the factor KR has to be minimized according to its geometry. This results in the following relation

$$\frac{L_n A_p}{L_p A_n} = \left(\frac{\rho_p \lambda_n}{\rho_n \lambda_p} \right)^{1/2} \quad (1.74)$$

Now Z becomes independent of the geometric dimensions and describes the thermoelectric figure of merit for a pair of materials in the following way.

$$Z = \frac{(S_p - S_n)^2}{[(\lambda_p \rho_p)^{1/2} + (\lambda_n \rho_n)^{1/2}]^2} \quad (1.75)$$

To estimate the thermoelectric quality of a single material the equation above is modified as follows

$$Z_{p,n} = \frac{S_{p,n}^2}{\rho_{p,n} \lambda_{p,n}}, \quad (1.76)$$

but only in the special case when p- and n- branch are very similar in S , ρ and λ this value can be related to the general Z from definition 1.75. Z has the dimension K^{-1} and it has become common to use ZT , as it is a dimension-less parameter for the characterization of thermoelectric materials.

$$ZT = \frac{S^2 T}{\rho \lambda}, \quad (1.77)$$

According to Eqn. 1.77 the ideal thermoelectric material should possess large thermopower, low electrical resistivity and low thermal conductivity. As it was shown in 1.1.2 ρ and λ_e are correlated by the Wiedemann-Franz law (1.37) so an optimization of λ is restricted to minimizing λ_{ph} .

Chapter 2

Experimental techniques

2.1 Sample preparation

Ce, Pd, Rh and Ag, each of 99.9% purity and ^{11}B of 99.9999 purity were used as starting materials. To synthesize CePd_3 and CeRh_3 the starting elements were weighed roughly and molten in a high frequency induction furnace under 99.999% pure Ar atmosphere with 0.4 bar overpressure on a water-cooled copper groove, to fumigate any volatile impurities. Then the elements were weighed in exact stoichiometric proportions and melted together. In the next step the resulting border phases were brought to fusion in the proper percentage to get a sample set of $\text{Ce}(\text{Pd}_{1-x}\text{Rh}_x)_3$ with the variable grade of substitution x . For the CePd_3B_y - and $\text{Ce}(\text{Pd}_{1-x}\text{Rh}_x)_3\text{B}_{0.05}$ -series the suitable amount of B was added to the finished CePd_3 specimens and melted together. The $\text{Ce}(\text{Pd}_{0.94-x}\text{Rh}_x\text{Ag}_{0.06})_3$ -samples were produce using CeRh_3 as master alloy which was brought together in one step with suitable amounts of pure Ce, Pd and Ag. For each fusion the samples were melted several times. Between the liquefaction the specimens were flipped over and every second time they were fragmented into several pieces, the outer parts moved to inside positions prior to remelting to guarantee homogeneous samples. After the synthesis the specimens were sealed in silica capsules under vacuum and were heat treated at 700°C for 100 h followed by quenching in water. Afterward the samples were cut into pieces suitable for the particular measurement setup using either a diamond wheel saw or a diamond wire saw.

2.2 Structure analysis

Phase conditions of the samples were checked at room temperature using X-ray powder diffraction data, which were obtained using a Huber Guinier powder camera and monochromatic CuK_α -radiation with an image plate recording system. Precise lattice parameters were calculated by least squares fit

of the indexed 4Θ -values obtained from X-ray film recordings using Ge as internal standard ($a_{\text{Ge}}=0.5657906$ nm). For quantitative refinement of the atom positions, X-ray intensities were collected in transmission from a flat specimen in a Guinier image plate camera. Rietveld refinements were carried out by employing the program package FULLPROF (see also [45]).

2.3 Electrical resistivity measurements

$\rho(4.2 - 300 \text{ K})$

Calibration measurements to get absolute values of the electrical resistivity in the temperature range from 4.2 K to room temperature were carried out in a liquid nitrogen shielded ^4He cryostat on bar-shaped samples with a length of 5-10 mm and a cross-section of about 1 mm^2 . The specific resistivity was measured via a DC four point technique realized by four gold needles, pressed against the specimen with springs, serving as electrical contacts. The voltage drop is measured once in one current direction and than in the other to compensate any thermo voltages. The temperature is detected by a thermocouple (AuFe0.07%/Chromel) which uses a thermos bottle filled with sludge as reference. After the first series of $\text{Ce}(\text{Pd}_{1-x}\text{Rh}_x)_3$ and the measurement of CePd_3B_y the cryostat has been changed and instead of the DC four point technique a new setup employing an *AC resistance bridge 370* by *LakeShore* with an additional low resistance scanner (Model 3716L) was used. For temperature measurements resistive sensors of Ge and Pt for $T < 30 \text{ K}$ and $T > 30 \text{ K}$, respectively, were used.

$\rho(0.4 - 150 \text{ K})$ as a function of an external magnetic field

To measure $\rho(T)$ between 0.4 and 150 K a ^3He -cryostat by *Cryogenics* was used. The ^3He insert is mounted in a liquid N coated ^4He vessel which contains a superconducting magnet which provides magnetic fields up to 14 T. The samples can be contacted either by gold needles as described above or by point welding, where wires of 99.996% Au with a diameter of 0.05 mm are point welded using a welding unit *UIP1000* by *Schmidt Instrumente*. The resistance was measured via DC four point technique as described above. The temperature was detected by a calibrated *Cernox* temperature sensor supplied by *Lakeshore*. In the course of back fitting the calibration measurement setup, an AC resistance bridge by *LakeShore* was implemented into this equipment.

$\rho(1.5 - 300 \text{ K})$ in dependence of pressure

Pressure dependent resistivity measurements between 1.5 and 300 K were made up to about 23 kbar. The samples which were about 4 mm long had

a cross-section of about $0.5 \times 0.5 \text{ mm}^2$ and were point welded and mounted on the sample holder which is part of a piston cylinder cell made out of MP35N using petroleum as pressure transmitting medium. Again a DC four point technique was used to measure the resistivity. The sample holder is introduced into a *variable temperature insert* (VTI), which is connected to a ^4He bath cryostat.

$\rho(300 - 900 \text{ K})$

For temperatures between room temperature and 800°C a dc four point measurement technique is used. Such high temperatures cause many problems in contacting the sample properly. A method which gives very reasonable results is to twine four contact wires around the sample and fix them with a drop of liquid silver. The sample holder is inserted in a steel tube which is part of a *NABER R70/9* furnace and the measurement is done under vacuum, to avoid oxidation of the samples.

2.4 Thermal conductivity

$\lambda(4.2 - 300 \text{ K})$

Thermal conductivity measurements between 4 and 300 K were performed in a flow cryostat working on ^4He . The cuboid-shaped samples were ideally $\approx 10 \text{ mm}$ long and had a quadratic cross section of 1.5 mm edge length. The bottom of the sample was fixed onto a copper panel mounted on the heat exchanger of the cryostat serving as heat sink. On the top of the sample a strain gauge was glued using superglue. This strain gauge served as heater and was powered by a constant current supply *J152 Knick*. Thus a temperature difference ΔT_S along the sample establishes. Measuring the voltage drop on the strain gauge, the applied power and thus the thermal flux Q can be deduced. The temperature gradient ΔT_S over a distinct sample length l was determined using a differential thermocouple (AuFe0.07%/Chromel) which had its reference temperature from a Pt and Ge thermometer stacked into a hole in the heat sink. ΔT_B is the temperature gradient between the heat sink and the lower thermocouple (see Fig. 2.1). Using these temperatures the average sample temperature T_S becomes

$$T_S = T_0 + \frac{\Delta T_S}{2} + \Delta T_B \quad (2.1)$$

and the thermal conductivity λ is calculated like follows

$$\lambda = \frac{l}{A} \frac{Q}{\Delta T_S}. \quad (2.2)$$

A is the sample cross-section which is determined before measurement. Sample and copper panel are surrounded by three radiation shields, the inner most is held on the same temperature as the heat sink. At elevated temperatures radiation losses during the measurement process contribute in a non negligible way to the signal resulting in a seemingly higher λ -values. The heat loss due to radiation is given by the Stefan Boltzmann law:

$$Q = \varepsilon\sigma_{SB}A(T_S^4 - T_0^4), \quad (2.3)$$

where T_S is the sample temperature, T_0 is the temperature of the heat sink and the surrounding radiation shield and A is the surface of the sample. The Stefan Boltzmann constant $\sigma_{SB} = 5.7 \times 10^{-8} \text{ Wm}^{-2}\text{K}^{-4}$ and the emissivity ε ranges between 0 and 1. It follows that

$$Q_{rad} = 2\varepsilon\sigma_{SB}AT_S^3\Delta T_S = aT_S^3 \quad (2.4)$$

and thus radiation effects manifest themselves in a T^3 -dependence of $\lambda(T)$ at elevated temperatures [46, 47]. To prove the accuracy of the method, we have measured the thermal conductivity of an austenitic steel-standard (Standard reference material 1461) provided by the National Bureau of Standard (NBS). Two samples (#1 and #2) with the same cross section but different tapping-length (0.728 and 0.145 cm) were tested and the results are plotted in Fig.

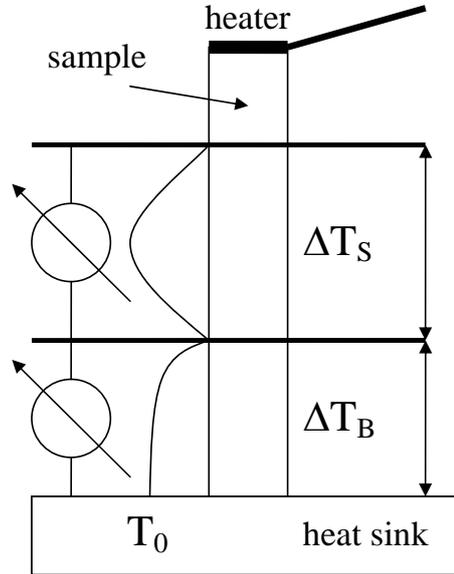


Figure 2.1: This is a sketch of the λ -measurement setup.

2.2. The distance between the thermal contacts is measured under microscope using a cross table with digital length measurement unit. With decreasing tapping length the absolute error increases and therefore one sees in Fig. 2.2 that the measured curve for sample #2 lies lower than the reference data. Assuming an offset of -12% the curve is shifted to fit the reference. The curves of blue circles, which show the difference between the measured $\lambda(T)$ -values and the reference data, were fitted according to Eqn. 2.4 and the resulting curve are plotted as purple solid. It is evident that the radiation losses are smaller for shorter tapping lengths. The fit-parameters a are $1.47 \cdot 10^{-6}$ and $0.44 \cdot 10^{-6}$ mW/cmK⁴ for sample #1 and #2, respectively. For easy sample handling and in order to keep the absolute error small a tapping length of about 0.5 cm is recommended and all samples of a series should have a comparable length.

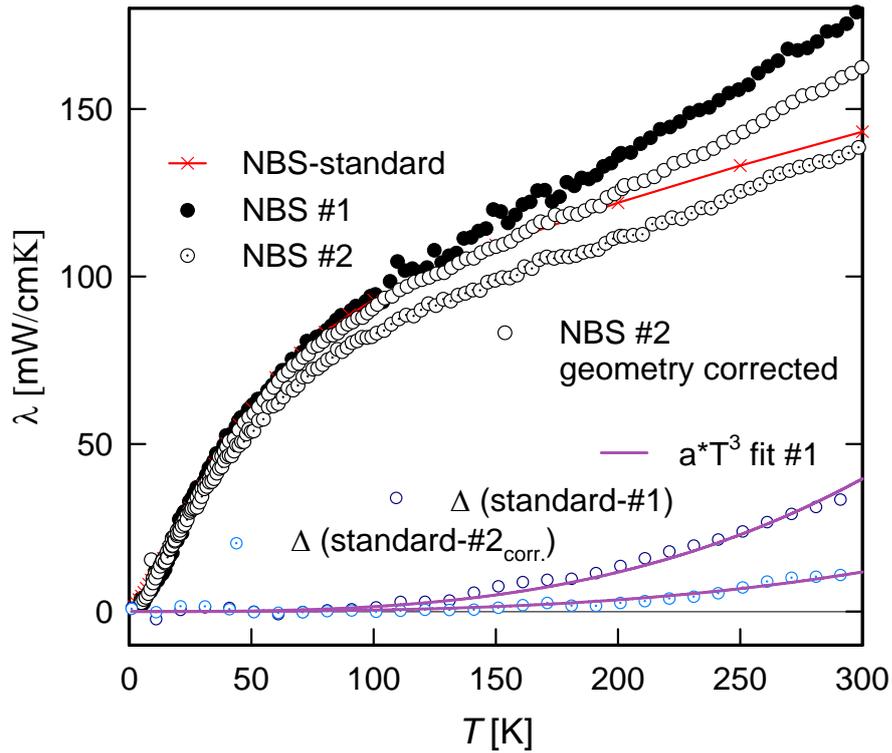


Figure 2.2: The diagram shows measured $\lambda(T)$ -curves of NBS-steel samples #1 and #2 with a tapping-distance of 0.728 and 0.145 cm, respectively. The data are compared to the reference data. Additionally the differences between the standard values and the measured are plotted (blue circles) and fit curves according to Eqn. 2.4 are shown (purple solid).

$\lambda(300 - 900 \text{ K})$

The Xenon flash system *Flashline 3000* by Anter Corporation was used to achieve thermal diffusivity α and heat capacity c_p data at elevated temperatures. λ can be computed from measured values of α and c_p , with the additional knowledge of material density ρ according to

$$\lambda = \alpha \rho c_p. \quad (2.5)$$

2.5 Thermopower

$S(4.2 - 300 \text{ K})$

In the *low temperature range* from 4 to 300 K the Seebeck coefficient was measured in a VTI which was inserted in a ^4He bath cryostat. In contrast to ρ - and λ -measurements where an accurate determination of the sample dimensions is necessary, the sample shape has no effect on the thermopower. The only restriction by our measurement setup is that the specimen should have two parallel plane faces with about 6 mm distance. The samples were clamped between two Au-plates. Each of these plates are contacted to two different thermocouples, one pair of Pb and AuFe0.07% for temperatures below 10 K the other for $T \geq 10$ made from Chromel/Pb. On the bottom of the sample holder a heater provides the necessary temperature gradient (see Fig. 2.3a). The voltages between the thermocouple wires of the same

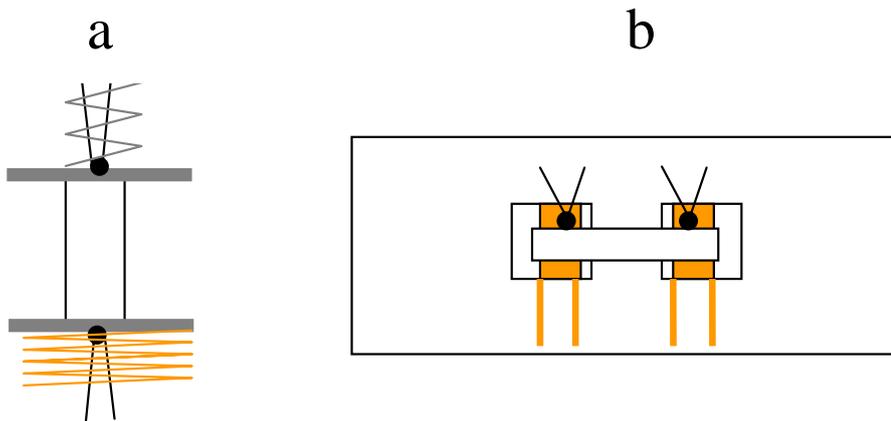


Figure 2.3: The left picture shows a sketch of the old fashioned S -measurement setup using a two point measurement technique (the black zigzag line on top symbolizes a spring). Figure b is a scheme of the new four point technique setup. In both sketches the heaters are marked orange.

sort were measured in both directions and averaged. The sample temperature was measured with Pt and Ge sensors. With the acquired data the Seebeck coefficient can be calculated using the following equation:

$$S_x = S_A - \frac{V_A}{V_A - V_B}(S_A - S_B) \quad (2.6)$$

S_A is the absolute thermopower of AuFe0.07% or Chromel and S_B represent the absolute thermopower of Pb and V_A and V_B are the voltages along the AuFe0.07% or Chromel and Pb circuits, respectively. This technique is a two point technique where the temperature gradient has always the same direction; this is comparable to a resistivity measurement with the current always flowing in one direction (DC-mode). A second measurement setup was revitalized in the scope of this work which is using a four point technique. This setup has two heaters which can raise a temperature gradient in two directions (comparable to the AC-mode in resistivity measurement). The sample holder is made of Cu where two strain-gauges are glued on two detached spots, in a distance of 3 mm, serving as heaters (see Fig. 2.3b). Bar-shaped samples with at least 5 mm length are needed. On each end of the sample a Constantan/Chromel thermocouple is fixed (either soldered or glued with epoxy-silver paste). The samples were glued on the heating panels using G.E.-varnish. A problem is that the wires of the thermocouples tend to distort the temperature on the measurement spot. Therefore the sample should be mounted in a way that the thermocouple contacts also touch the heaters. The measured voltages are averaged over both temperature gradient directions and Eqn. 2.6 is used to determined S_x . The sample temperature is determined using a Pt100 between 30 K and room temperature and a Ge resistive sensor for $T < 30$ K.

S(300 – 900 K)

With the *high temperature setup* data from 300 to 1000 K can be acquired. The measurement arrangement follows the same principle as that described for the two point method in the low T range (see Fig. 2.3a). The difference is that only one sort of thermocouple (Pt/PtRh10%) was welded onto Pt plates, which both measure the absolute temperature in reference to 0°C provided by sludge in a thermo flask. The heater was realized by a thermo coax wire. With this arrangement the thermopower can be calculated by

$$S_x = S_{Pt}(T) - \frac{V_{Pt,x}}{\Delta T}. \quad (2.7)$$

S_{Pt} denotes the absolute thermopower of platinum and $V_{Pt,x}$ the thermally induced voltage across the sample depending on a temperature difference ΔT .

Chapter 3

The CePd₃ system

CePd₃ crystallizes in the cubic AuCu₃ structure (Pm3m), where Ce occupies the 1a site and Pd the 3c sites (compare Fig. 3.1). It is an intermetallic compound with intermediate Ce valence of about 3.45 [48] and exhibits one of the highest Seebeck coefficients (up to 110 to 120 $\mu\text{V}/\text{K}$ at a broad maximum around 150 K) [49] within Ce based intermetallics. Such strongly enhanced $S(T)$ values are referred to an intense Kondo interaction responsible for a characteristic temperature T_K of about 240 K [50]. Enhanced values of T_K

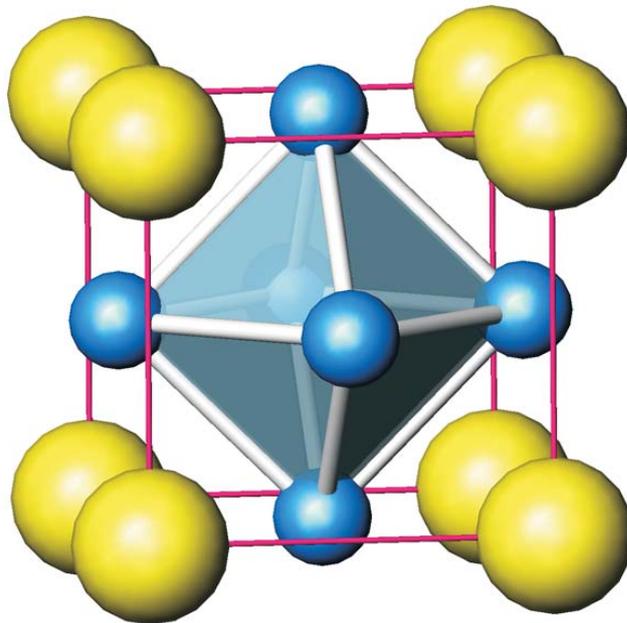


Figure 3.1: Crystal structure of CePd₃, where Ce is symbolized by yellow and Pd by blue balls.

are a fingerprint of a strong $4f$ - s, p, d hybridization which in turn promotes an intermediate electronic configuration of the Ce ion. Simultaneously, a high electron density of states at the Fermi level, associated with the Abrikosov Suhl resonance, provides the base requisite for an extraordinarily large Seebeck effect. Theoretically, this relationship follows within the scope of the single impurity Anderson model, which says that the density of states at the Fermi energy, expressed by the Sommerfeld value, is the relevant parameter driving the Seebeck effect in Kondo type materials. The resistivity of CePd_3 resembles the behavior of a Kondo lattice and exhibits a pronounced sensitivity for smallest deviations in the Ce/Pd-ratio as described manifold in literature (e.g. [48, 51, 3]). From the Ce-Pd phase diagram one can learn, that there is an extended stability region around the ratio 1:3 which also allows non-stoichiometric compounds like $\text{CePd}_{3+\epsilon}$ to build a single phase AuCu_3 -structure, in which Pd enters Ce-places and vice versa. Sthioul et al. [11] tested $\text{CePd}_{3+\epsilon}$ and found, that $\rho(4.2 \text{ K})$ varies from about 10 to 170 $\mu\Omega\text{cm}$ with ϵ from -0.08 to +0.08. A decrease of thermopower was reported also for increasing ϵ . Another crucial point is the thermal treatment after synthesis which also can have an enormous effect on the transport properties as Schneider et al. (1981) [51] have demonstrated. Contrary to that stands a publication by Besnus et al. (1983) [3] in which no effects of heat treatment on the resistivity are reported. Data from this paper are used in Fig. 3.2 to point out the effect of smallest deviations in stoichiometry on $\rho(4.2 \text{ K})$. The Ce concentrations taken from the paper are corrected by subtraction of 0.5 at% as it was described in the discussion of the same paper. From this data one can see the change of $\rho(T)$ with respect to the Ce concentration and that in Pd rich samples $\rho(4.2 \text{ K})$ -values even become larger than $\rho(300 \text{ K})$. Substitutions of Pd in CePd_3 by elements as Rh and Ru further enlarge the Kondo temperature T_K via enhanced hybridization and thus trigger significant deviations from integer valency. This was demonstrated quantitatively for CeRh_3 from a resonant inverse photo emission study, locating the position of the $4f^1$ peak at about 1 eV [52]. Since the maximum contribution in $S(T)$ occurs at a temperature roughly proportional to T_K [53], the substitution of Pd by Rh was expected to tune $S^{max}(T)$ over a broad range of temperatures. This group of materials exhibits generally good electric conduction as well as good thermal conductivity because the thermal conductivity part arising from the charge carriers can be directly related to the electrical conductivity via the Wiedemann-Franz law. The phonon part of the thermal conductivity can be reduced toward the theoretical minimum value via three major mechanisms: i) simple substitution introducing atom disorder; ii) phonon scattering on almost each lattice site by inserting atoms in the large cages of the structure thereby allowing extraordinary large thermal displacement parameters (rattling modes); iii) scattering of the heat carrying phonons on

valence fluctuating electrons of atoms with valence instabilities (breathing modes). The AuCu₃-structure, which is, in fact, an unfilled perovskite, provides the opportunity of filling the interstitial 1b site with rattling atoms like B, C, Si, Al and Ga. Such an atom insertion shifts the Fermi level and as a result, the Seebeck coefficient alters. A decrease of thermopower was observed for CePd₃B_y by Houshiar et al. [12], but for CePd₃Ga_x an increase of ZT was published [54]. Other studies have shown that pressure applied to CePd₃B_y regains the high absolute thermopower values of CePd₃ [55] and thus compensates the reduction due to the insertion of B. A similar observation was made for Ce(Pd_{1-z}Ag_z) [11] where this recovery is attributed to a continuous pressure induced transition to a more intermediate valence (IV) state. It is possible that the substitution of Pd by Rh in the context of the insertion of B, C, Si . . . may keep the charge carrier count unchanged, thus we expected that the absolute thermopower values recover at zero pressure. All effects outlined in i) to iii), the transition metal substitution, the rattling mode of the inserted B atoms as well as possible additional phonon scattering due to valence fluctuations of the Ce, should act together efficiently to minimize the thermal conductivity. With a thermopower nearly unchanged

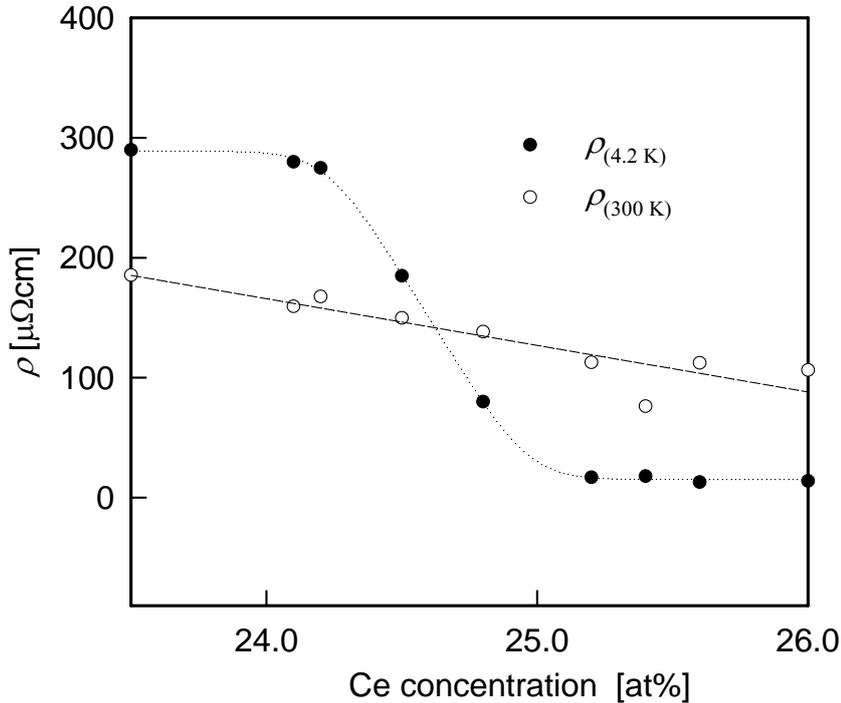


Figure 3.2: The picture shows data taken from Besnus et al. [3] (1983) to point out the effect of deviations in the Ce concentration on the resistivity at 4.2 and 300 K. The dotted and dashed lines are guides for the eye.

and a slightly reduced electrical resistivity a increase of ZT seems possible. The following chapters will elucidate the effect of substitution and doping on the thermoelectric properties on CePd₃.

3.1 CePd₃ sample series

In the scope of sample preparation five sample series were synthesized.

- CePd₃B_{*y*}
with B concentrations $y = 0.05, 0.10, 0.15, 0.20, 0.25, 0.30, 0.40$
- Ce(Pd_{1-*x*}Rh_{*x*})₃
with Rh concentrations $x = 0.0, 0.1, 0.2, 0.4, 0.6, 0.8, 0.9, 1$
- Ce(Pd_{1-*x*}Rh_{*x*})₃
with Rh concentrations $x = 0.00, 0.03, 0.06, 0.09, 0.15$
- Ce(Pd_{1-*x*}Rh_{*x*})₃B_{0.05}
with Rh concentration of $x = 0.00, 0.03, 0.06, 0.09, 0.15$
- Ce(Pd_{0.94-*x*}Rh_{*x*}Ag_{0.06})₃
with Rh concentration of $x = 0.00, 0.03, 0.06, 0.09$
and an additional CePd₃ sample

Three different CePd₃ samples were synthesized as border phases for the different sample series. X-ray diffraction measurements were used to test the samples for phase purity and from that data the three samples are nearly identical as evidenced from the extracted lattice parameters. Nevertheless $\rho(T)$, $\lambda(T)$ and $S(T)$ differ a lot as it is shown in Fig.3.3. The left panel of that figure shows the measured values of $\lambda(T)$, which reveals at temperatures $T > 150$ K an oversized increase due to radiation losses. The λ_{ph} -curves are calculated by applying the Wiedemann-Franz law (1.37) and subtracting the radiation losses assuming a T^3 -dependence (a detailed description of this procedure can be found in chapter 3.2). At low temperatures the resistivity of CePd₃⁽³⁾ has a more significant shoulder than CePd₃⁽¹⁾ and the maximum is slightly increased and shifted to lower temperatures. Also the $S(T)$ values are slightly higher at lower temperatures and the maximum is shifted to lower temperatures as well. λ_{max} stays at the same temperature, but its value is halved due to a significant decrease of λ_{ph} . CePd₃⁽²⁾ is characterized by a much higher $\rho(T)$ over the entire temperature range and $S(T)$ is significantly decreased. A $\lambda(T)$ measurement of CePd₃⁽²⁾ was not possible, because the sample broke. The reason for this large deviations is the sensitivity of CePd₃ to smallest changes in the stoichiometry as it is described above. From weighing the samples before and after the synthesis no preparation mistakes

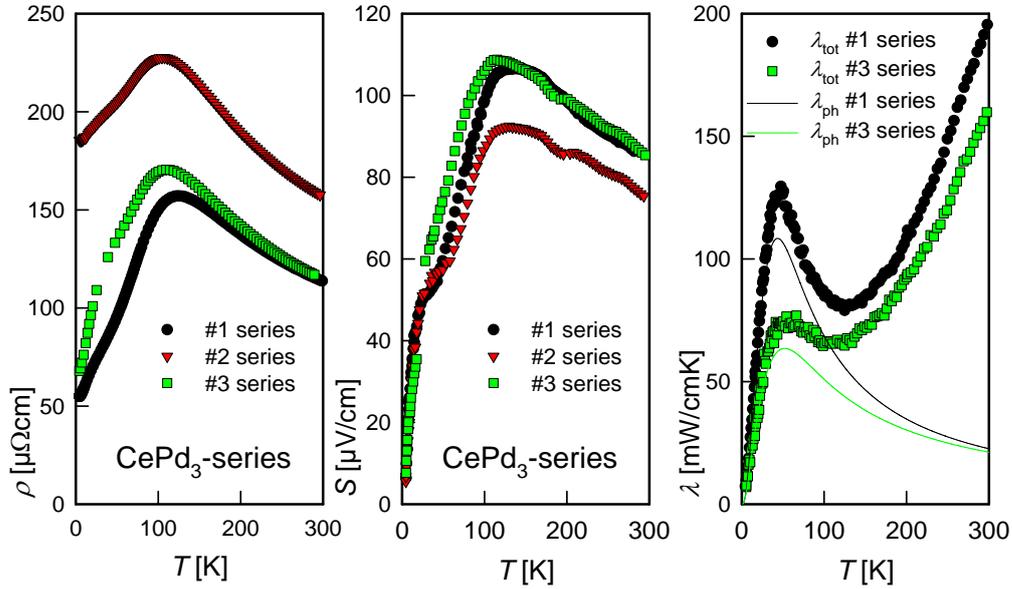


Figure 3.3: $\rho(T)$, $S(T)$ and $\lambda(T)$ data for the different CePd₃ samples.

became evident and all samples were heat treated in a similar manner. To investigate the deviations between the different sample compositions electron probe micro-analysis (EPMA) were performed employing a *Carl Zeiss DSM 962*. It was found, that all samples have the same composition of CePd₃, within the accuracy of the equipment, but in sample CePd₃⁽²⁾ small precipitations of a Ce-rich phase, most probably CeO₂ were found, which can be a reason for the discrepancy of the transport properties. Micrographs of metallurgically prepared surfaces of representative samples of the different series are mapped in Fig. 3.4, where one can see the Ce-rich precipitations as dark points in the lower left panel. CePd₃⁽¹⁾ shows large areas of differently colored phases separated by a darker phase. From the analysis no difference between the large phases can be deduced, but the dark border phase is Pd enriched. Because the absolute values of the compositions deduced by this method were not granted, a second test was performed using a *Philips XL-30 ESEM*. With this instrument the overall surface of the selected samples was analyzed to reassure that the Ce/Pd ratio has not changed during the preparation. Within the accuracy of the method the samples are not distinguishable and show a Ce/Pd ratio of 1:3.

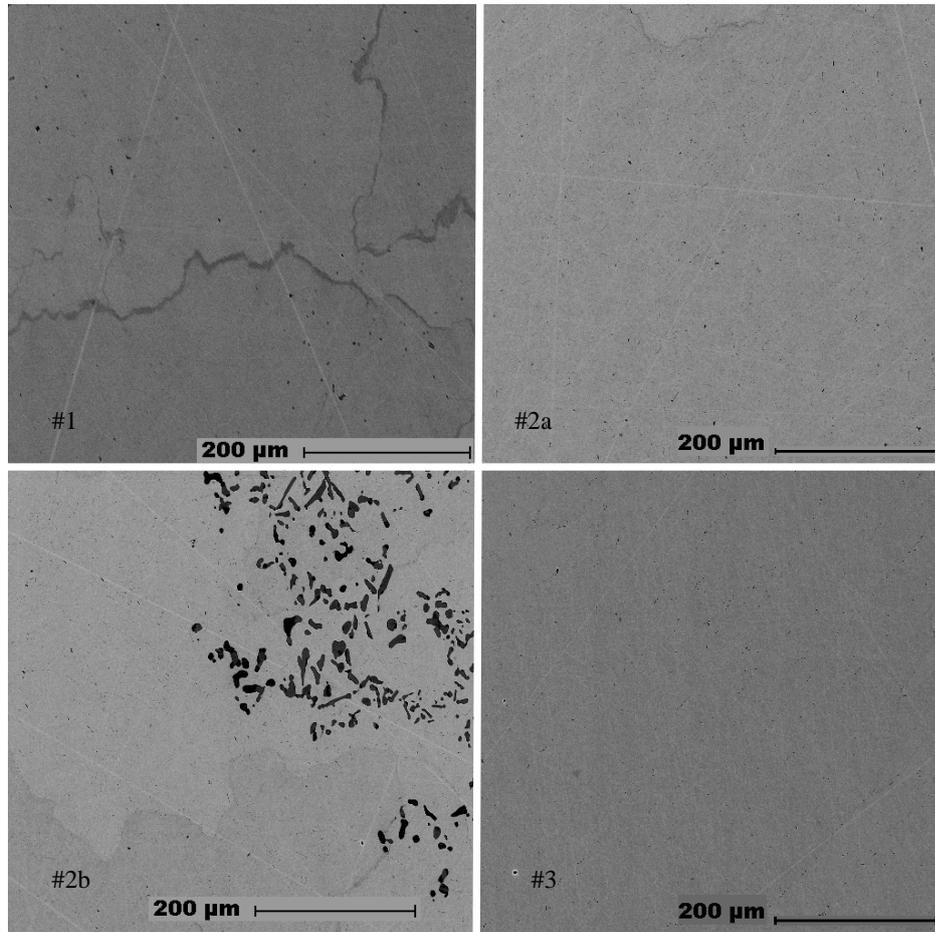


Figure 3.4: Micrographs taken with a *Carl Zeiss DSM 962* show metallurgically prepared surfaces of three samples, representing the different samples series. $\text{CePd}_3^{(1)}$ shows large areas of differently colored phases with similar Ce/Pd ratio separated by a darker Pd-rich phase. $\text{CePd}_3^{(2)}$ has very homogeneous regions (see panel #2a) but also Ce rich phases like in panel #2b. $\text{CePd}_3^{(3)}$ shows the most homogeneous sample surface

3.2 CePd_3B_y

The introduction of boron into CePd_3 causes an increase of the lattice constant a and the Ce valence is tuned from about 3.45 to its 3+ state [56]. Regarding the X-ray diffraction data the samples are single phased and the extracted lattice constants (compare Fig. 3.5) are in good agreement with data from literature [9], where it is assumed that the B enters most likely the 1b site of the crystal structure. The fact that the lattice constant doesn't change above B concentrations of $y \geq 0.25$ can either mean that a small boron

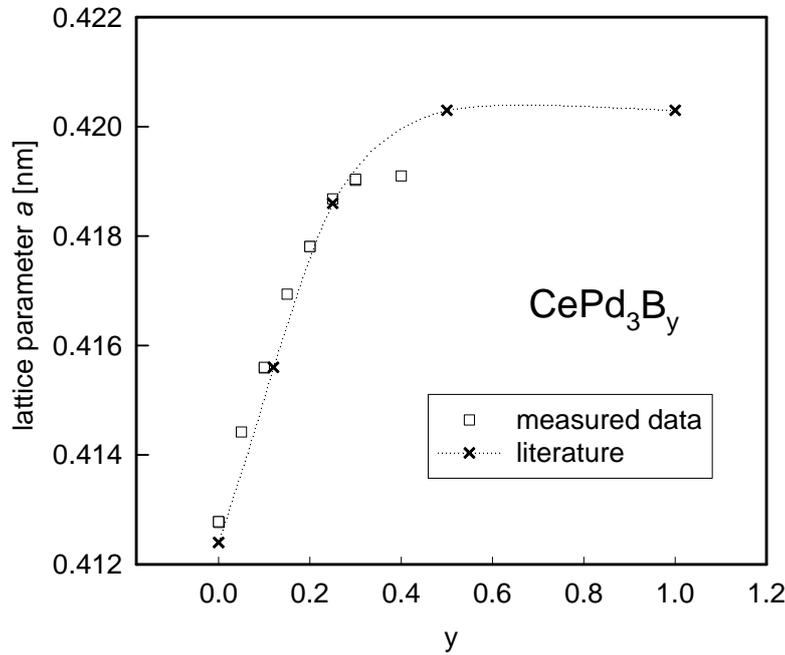


Figure 3.5: Lattice constants of CePd_3B_y in dependence of the B concentration y . The dotted line is a guidance for the eye following the data from literature.

concentration expands the lattice so much that additional B has enough space within the lattice. A second description could be that the solubility of B in CePd_3 is restricted, like it is for the other elements of group 13, and the residual B is accumulated between grain boundaries. The second interpretation stands in contrast to conclusions by Dhar et al. [9], but X-ray diffraction has not the resolution to point out the B position and no neutron diffraction data were collected up to now, which could clarify this matter. On sample $\text{CePd}_3\text{B}_{0.4}$ an additional investigation using a Philips CM 200 transmission electron microscope (TEM) operating at 200 kV, has been made to find out if there exists a superstructure like it has been found for $\text{CeRh}_3\text{B}_{0.5}$ (tetragonal system, space group $I4/mmm$) by K. Yubuta et al. [57]. We observed neither superlattice reflections at $1/2 \ 1/2 \ 1/2$ positions nor satellites around the Bragg reflections, therefore we conclude that $\text{CePd}_3\text{B}_{0.4}$ still adheres to space group $\text{Pm}\bar{3}\text{m}$.

3.2.1 Electrical resistivity

In the range of small B content the resistivity data show impressively how T_K decreases and vanishes for a boron content of about $y = 0.2$. At concentrations $y \leq 0.2$, where the system can be described using the Kondo lattice model, the right shoulder of the maximum was approximated with the sum of a residual resistance ρ_0 , a phonon scattering term ρ_{ph} calculated using Bloch Grüneisen equation 1.14 and a logarithmic temperature dependent term coming from Eqn. 1.32, like in the following equation with c denoting a scaling constant.

$$\rho(T \gg T_{max}) = \rho_0 + \rho_{ph} + c * \ln[T] \quad (3.1)$$

Theoretically the logarithmic term is proportional to $\ln[\frac{T}{T_K}]$ (compare Eqn. 1.32), but the T_K can not be figured out by this method, because mathematically ($\ln[\frac{T}{T_K}] = \ln[T] - \ln[T_K]$) it enters into ρ_0 , which can't be split. While $\rho(T)$ of CePd₃ can also be fitted applying Eqn. 1.34, this model can not produce a satisfying match of the $\rho(T)$ -behavior of the CePd₃B_y-series. With higher doping ($y > 0.2$) the $\rho(T)$ curves show a linear increase for $T > 10$ K and the straight lines are parallel so that they fall on one line when normal-

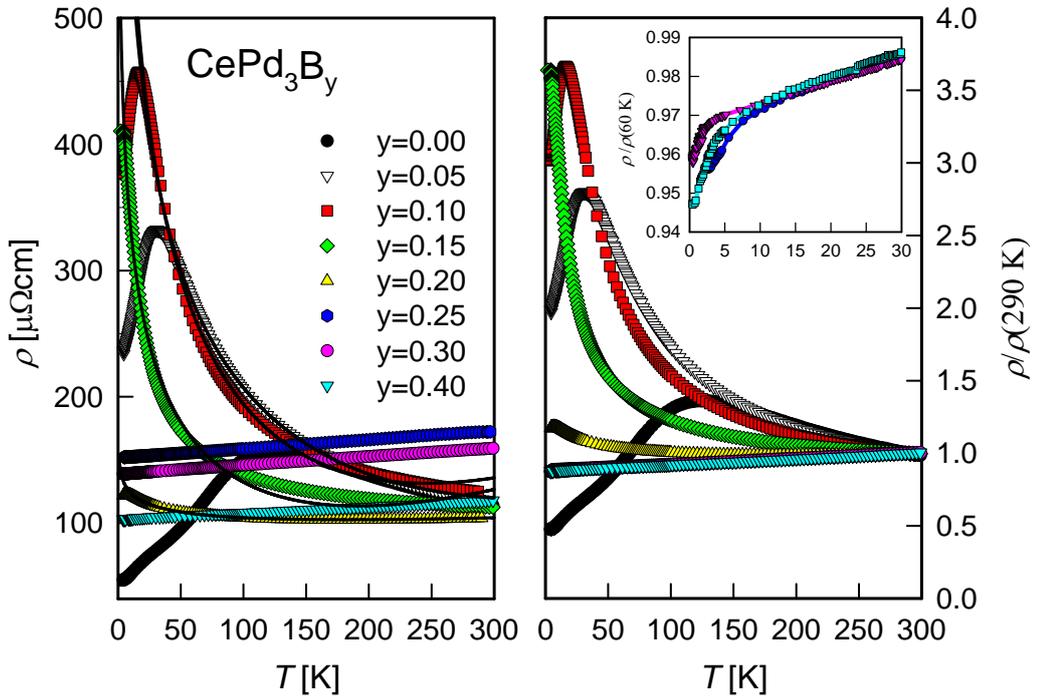


Figure 3.6: The left panel shows the temperature dependent resistivity $\rho(T)$ in dependence of the B concentration y . Solid lines are fit-curves based on Eqn. 3.1. The right panel shows the data normalized to the resistance at 290 K.

ized to $\rho(290\text{ K})$ as it is mapped in the left panel of Fig. 3.6. With increasing y the offset declines. At lowest temperatures $T < 10\text{ K}$ the slope of $\rho(T)$ decreases more rapidly, as it is depicted in the inset of Fig. 3.6, which could be due to a spin-glass transition also reported in [58]. The magnetic field dependence of the resistivity down to 0.5 K was also tested, but there is no remarkable change with external fields up to 12 T .

3.2.2 Thermopower

Absolute values of the characteristic temperatures T_0 and T_f , which correspond to T_K , can be extracted from the thermopower data. Fig. 3.7 displays the measured $S(T)$ -curves with additional solid black lines which represent fit curves according to the formula by M. Koterlyn (*M.K-model* see Eqn. 1.65)

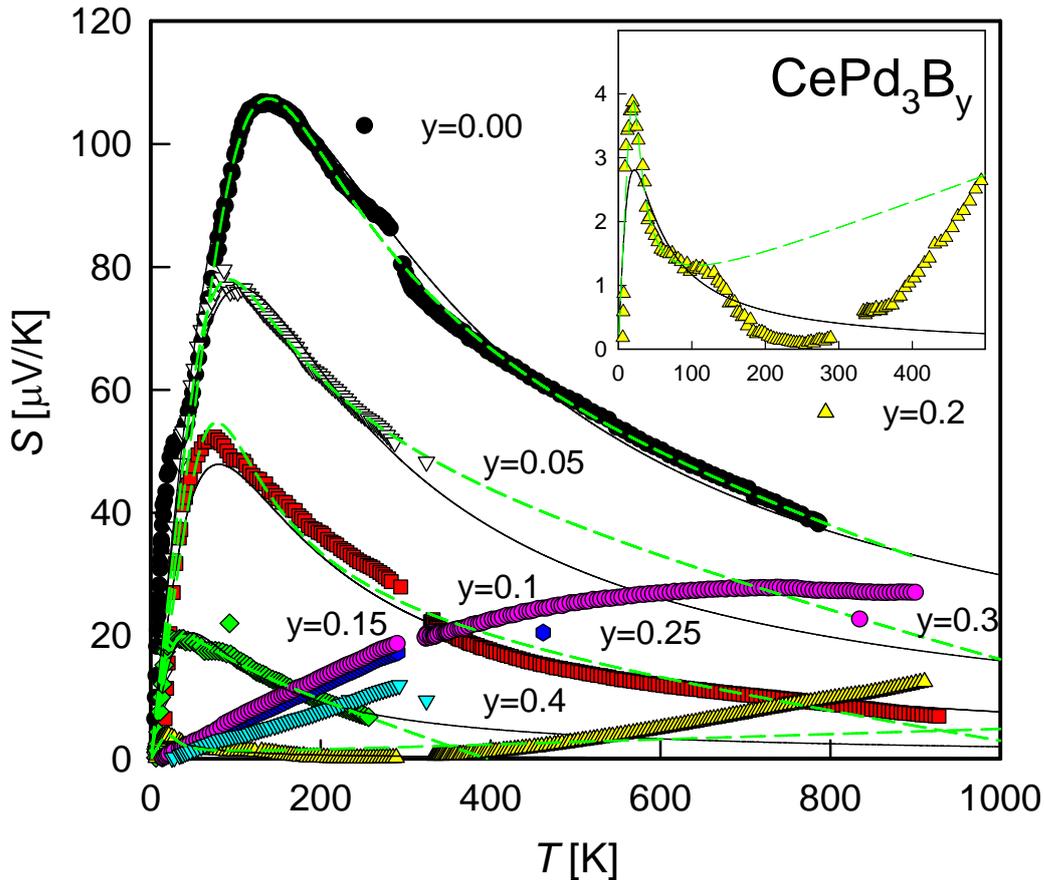


Figure 3.7: Thermopower of CePd₃B_y for various concentrations of B. The solid black lines are fit curves obtained from Koterlyn's equation. The green dashed lines are the result of a fit according to the model by Freimuth.

where a further dimensionless scaling parameter k was multiplied to the term, to reproduce the magnitude of the values, while N_f was kept constant 6. The dashed green lines in the diagram represent curves generated by the model by A. Freimuth (*A.F-model* compare Eqn. 1.64). A feature which can not be reproduced by both procedures is the negative Seebeck coefficient at lowest temperatures. Data have been collected between 4.2 to 900 K where at about 300 K the measurement setup is changed. Therefore some points are missing and the connection of the curves is not completely smooth. The decrease of $S(T)$ due to B doping as well as the shift of T_{max}^S to lower temperatures is associated with the crossover from intermediate to integer valence (3+) for $y \geq 0.25$. The $S(T)$ -behavior of CePd₃B_{0.2} is depicted in the inset of Fig. 3.7. Its low temperature dependence is similar to that of the samples with lower B content; the distinct maximum is followed by a decrease of $S(T)$, but there is a shoulder at the right flank of the peak, which is absent at the other samples. At about 300 K a shallow minimum establishes and for temperatures above 500 K the thermopower increases almost linearly. The extracted

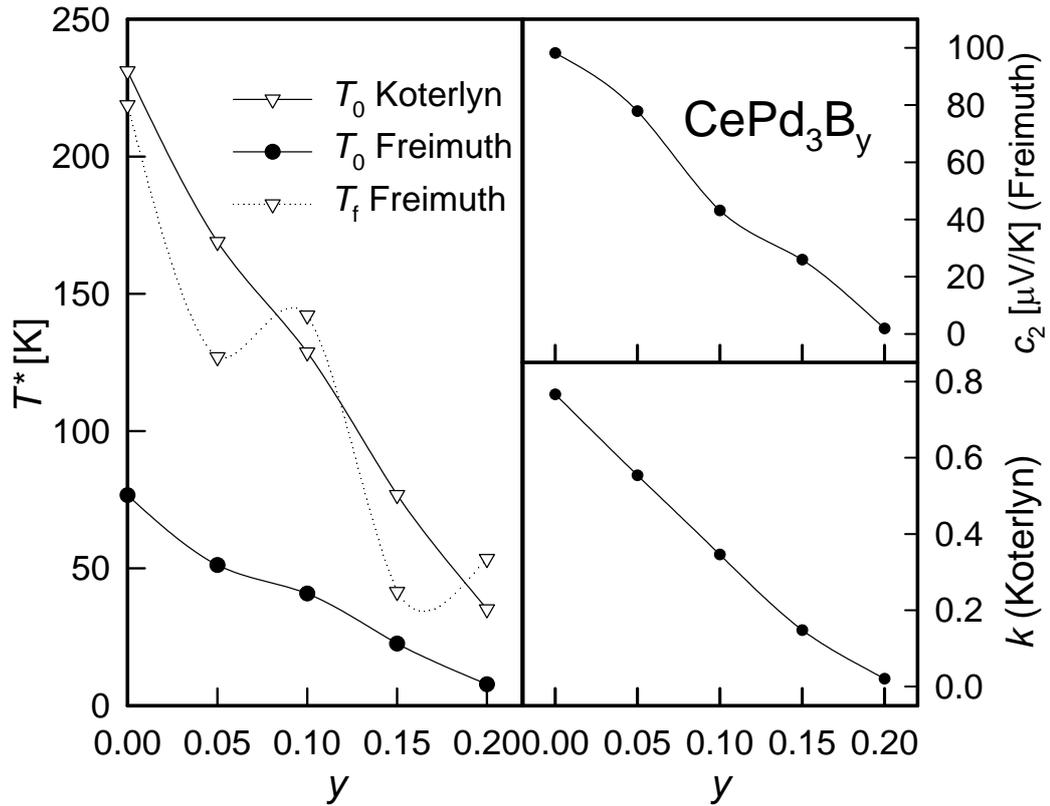


Figure 3.8: T_0 , T_f , c and c_2 of CePd₃B_y determined using the models by Koterlyn and Freimuth in dependence of the B concentration y .

characteristic temperatures are depicted in Fig. 3.8 together with the scaling parameter c . It becomes evident that T_0 from the *M.K-model* coincide rather with T_f from the *A.F-model* although both use the same definition for T_0 . The application of the *M.K-model* results in a linear decrease of both, T_0 and the scaling parameter c up to a B concentration of 20%. The very special curvature and the increase of thermopower at high temperatures for CePd₃B_{0.2} can not be reproduced by the *M.K-model*. The *A.F-model* also reflects the decrease of the characteristic temperatures and the scaling parameters, but the extracted values are not in line, which may be mainly due to the lack of high temperature data for some samples and therefore an improper extrapolation. The *M.K-model*, however, seems not to be distinctly effected by this problem. On the other hand the *A.F-model* is able to emulate tendencies of the complicated $S(T)$ -behavior of CePd₃B_{0.2} (compare Fig. 3.8).

3.2.3 Thermal conductivity

The temperature dependence of the thermal conductivity has also been measured for the complete sample set and the results are displayed in Fig. 3.9. The change in thermal conductivity is not continuously with increasing B concentration as it has been observed for the $\rho(T)$ or the $S(T)$ measurements. It has been expected that the B is loosely bound in the center of the AuCu₃-structure and increases scattering of phonons due to so called rattling modes. Indeed $\lambda_{tot}(T)$ shows a distinct decrease with increasing B concentration up to 10%. Most notably is the suppression of the maximum at about 50 K. But for $y \geq 0.10$ no further dramatic changes in the behavior of $\lambda_{tot}(T)$ occurs. For $y=0.15$ and 0.2 the total thermal conductivity is higher than for the sample with $y=0.10$. This increase is due to a enhancement of λ_{ph} with increasing B content which is opposite to the expected behavior. The lowest lying $\lambda(T)$ -curve shows CePd₃B_{0.3}. The left panel of Fig. 3.9 shows the measured data with an oversized slope of the curves at higher temperatures due to radiation losses. As discussed in the experimental part the losses can be compensated using Eqn. 2.4. $\lambda_{tot}(T)$ can be separated into the lattice and the electronic part, $\lambda_{ph}(T)$ and $\lambda_e(T)$, respectively, according to formula 1.35. The standard approach uses the Wiedemann-Franz law (*WF-l* Eqn. 1.37) to deduce the electronic thermal conductivity $\lambda_e(T)$ from the electrical resistivity $\rho(T)$. By subtracting $\lambda_e(T)$ from $\lambda_{tot}(T)$ the phonon contribution $\lambda_{ph}(T)$ is obtained and further interpreted by using the model from Callaway, Eqn. (1.45). The right panel of Fig. 3.9 shows fit-curves of $\lambda_{tot}(T)$ derived using the *WF-l* and corrected with respect to radiation losses. A second model based on Wilson's equation (*W-Eqn* 1.39) is introduced to fractionate $\lambda_{tot}(T)$ and therefore cross check the reliability of the results. This was done by simple adding Eqn. 1.39 to Callaway's term and fitting $\lambda_{tot}(T)$ within one step. As discussed above an additional T^3 -term was introduced in both procedures

to estimate the radiation losses. Figure 3.10 shows the measured $\lambda_{tot}(T)$ of CePd₃⁽¹⁾ and how the applied models reproduce the different contributions. The *W-Eqn* doesn't take into account Kondo effect or other magnetic contributions to λ_e , therefore it generates a structureless curve at low temperatures and underestimates $\lambda_e(T)$ compared to the *WF-l* which produces a distinct shoulder below 100 K. This lowered $\lambda_e(T)$ is compensated by an inflated $\lambda_{ph}(T)$ emulated by *W-Eqn*. Both models independently estimate nearly the same radiation losses. Even at room temperatures λ_{ph} is 3.6 times larger than λ_{min} . In the upper panels of Fig. 3.12 fitting results of the $\lambda_e(T)$ data sets, based on the *W-Eqn* (right panel) and the *WF-l* (left panel) are displayed. It is remarkable, that both models provide comparable values. For $y=0.25$ and 0.3 the curves derived by *WF-l* are completely different to the rest of the data, which is due to the small electrical resistivity of these compounds. The more astonishing is that for $y=0.3$ even this change of the curvature is repro-

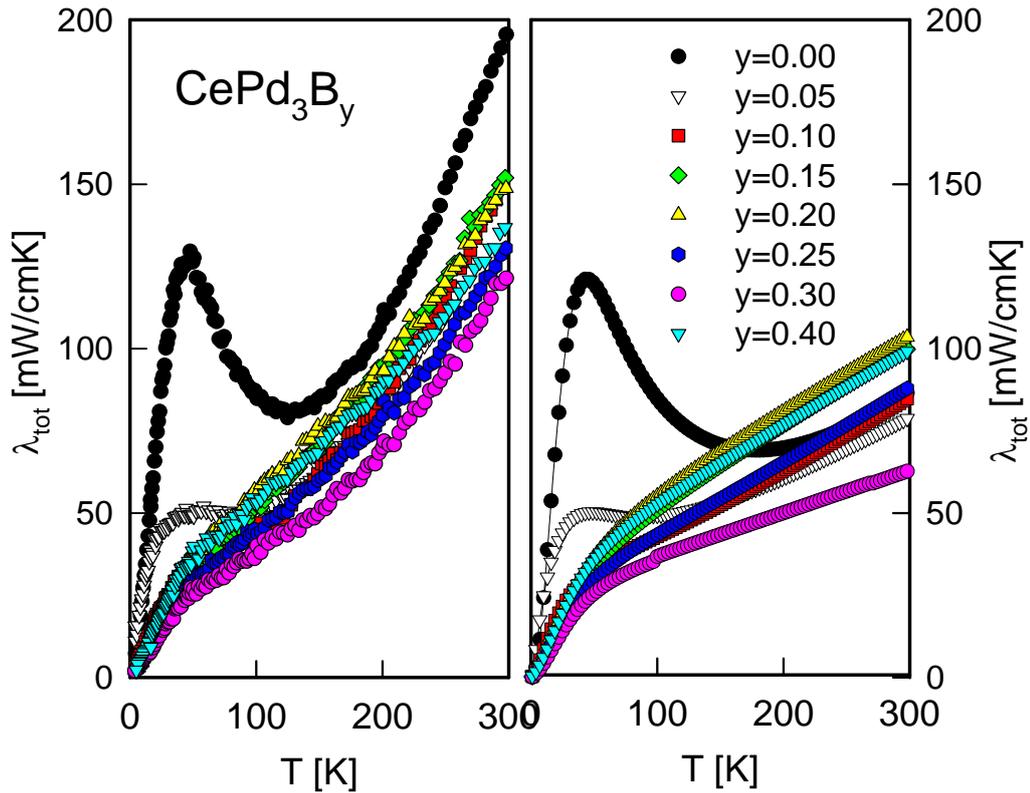


Figure 3.9: The left panel displays the measured thermal conductivity of CePd₃B_y in dependence of the B concentration y . The right panel shows fit-curves of $\lambda_{tot}(T)$ derived using the *WF-l* and corrected with respect to radiation losses.

duced by the fit using *W-Eqn*. Inspecting the data, compared for $\lambda_{ph}(T)$ in Fig. 3.12, the lower panels, reveals again a general agreement. Both models clearly point out a substantial decrease of $\lambda_{ph}(T)$ with rising B content. The curvature of $\lambda_{ph}(T)$ for $y \geq 0.15$ is changed in comparison to $y < 0.15$ if one uses the *WF-l*, while an interpretation applying the *W-Eqn* produces only two different shaped $\lambda(T)$ -curves for $y = 0.15$ and 0.2.

From this insight it can be concluded, that with B doping the maximum of $\lambda_{ph}(T)$ at about 50 K is reduced by a factor of approximately 3.5, at 150 K λ_{ph} is halved after all, while at room temperature in some cases it is even increased. Keeping in mind the bisection of $S(T)$ with 10% B content, this results will bring no improvement of thermoelectric properties. Nevertheless an analysis of $\lambda_{ph}(T)$ in terms of different scattering contributions can give an interesting insight on the dominating mechanisms. As both fit procedures

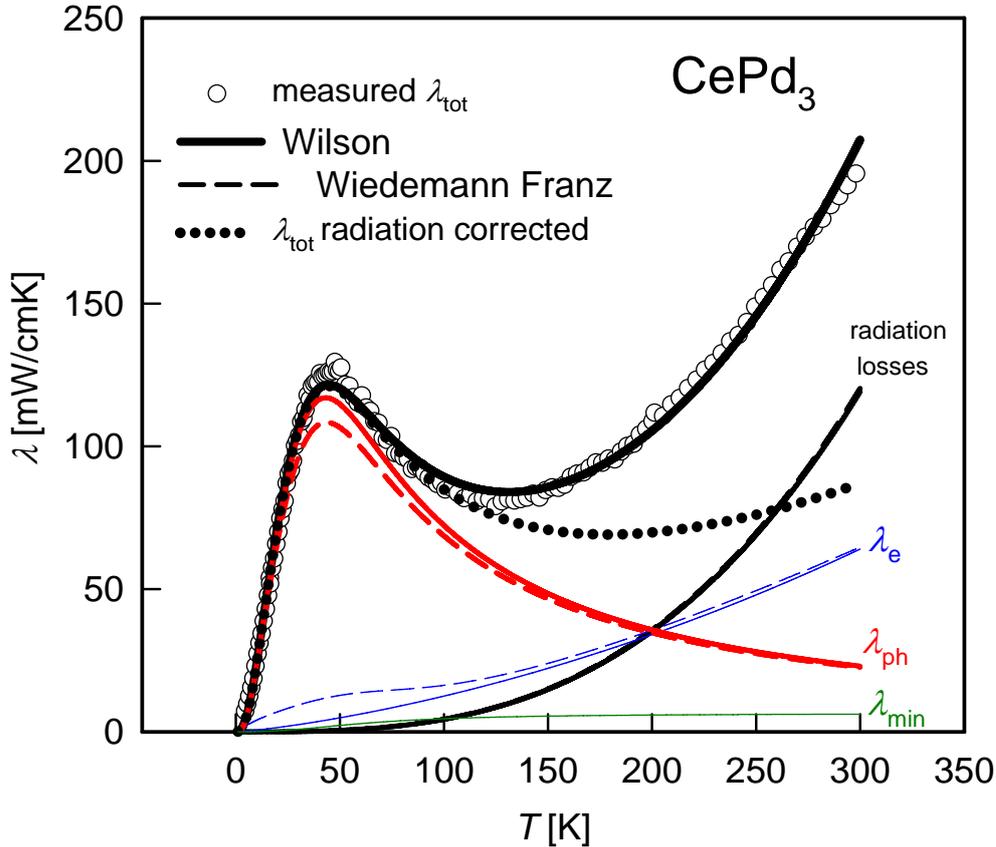


Figure 3.10: The picture shows the measured $\lambda(T)$ and the different contributions $\lambda_{ph}(T)$, $\lambda_e(T)$ with an additional share related to radiation losses evaluated using Wiedemann-Franz law or Wilson's equation. The dark green line corresponds to λ_{min} (see Eqn. 1.59)

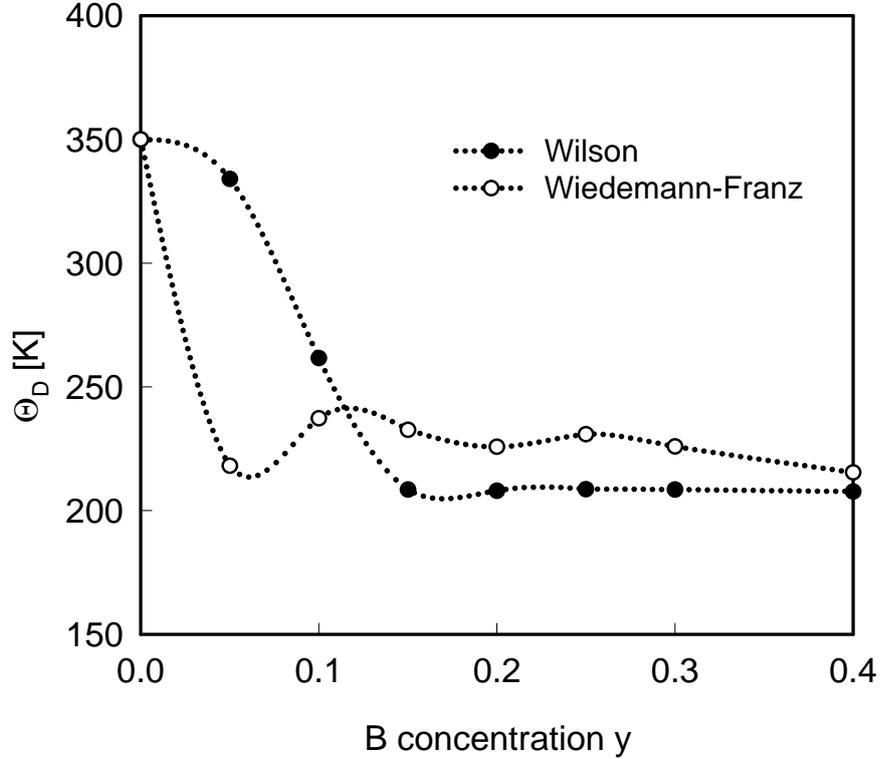


Figure 3.11: The Debye temperature θ_D in dependence of the B concentration y in CePd₃B _{y} evaluated applying Wilson's equation or Wiedemann-Franz law, denoted by black and white circles, respectively, in combination with Callaway's model.

were based on the Callaway's theory [23, 59] described in detail in section 1.1.2, the derived fit parameters should reflect, at least, tendencies how the doping affects $\lambda_{ph}(T)$. We have used the relaxation time approximation with an averaged relaxation time $\tau_c^{-1} = \tau_U^{-1} + \tau_D^{-1} + \tau_B^{-1} + \tau_{ph-el}^{-1}$, where τ_U , τ_D , τ_B and τ_{ph-el} denote Umklapp processes, point defect scattering, boundary scattering and scattering of phonons by electrons. For every scattering mechanism one fit parameter has been taken into account, furthermore the Debye temperature θ_D and an additional parameter regarding the radiation losses are necessary. Thus six fit-parameters are used, which can result, of course, in rather vague results. Nevertheless developments in the governing scattering processes due to the doping can be deduced. For the matching procedure the program *TableCurve 2D 5.01* was used (a detailed description of the procedure is given in A.3). For θ_D both approaches gave reasonable results, which

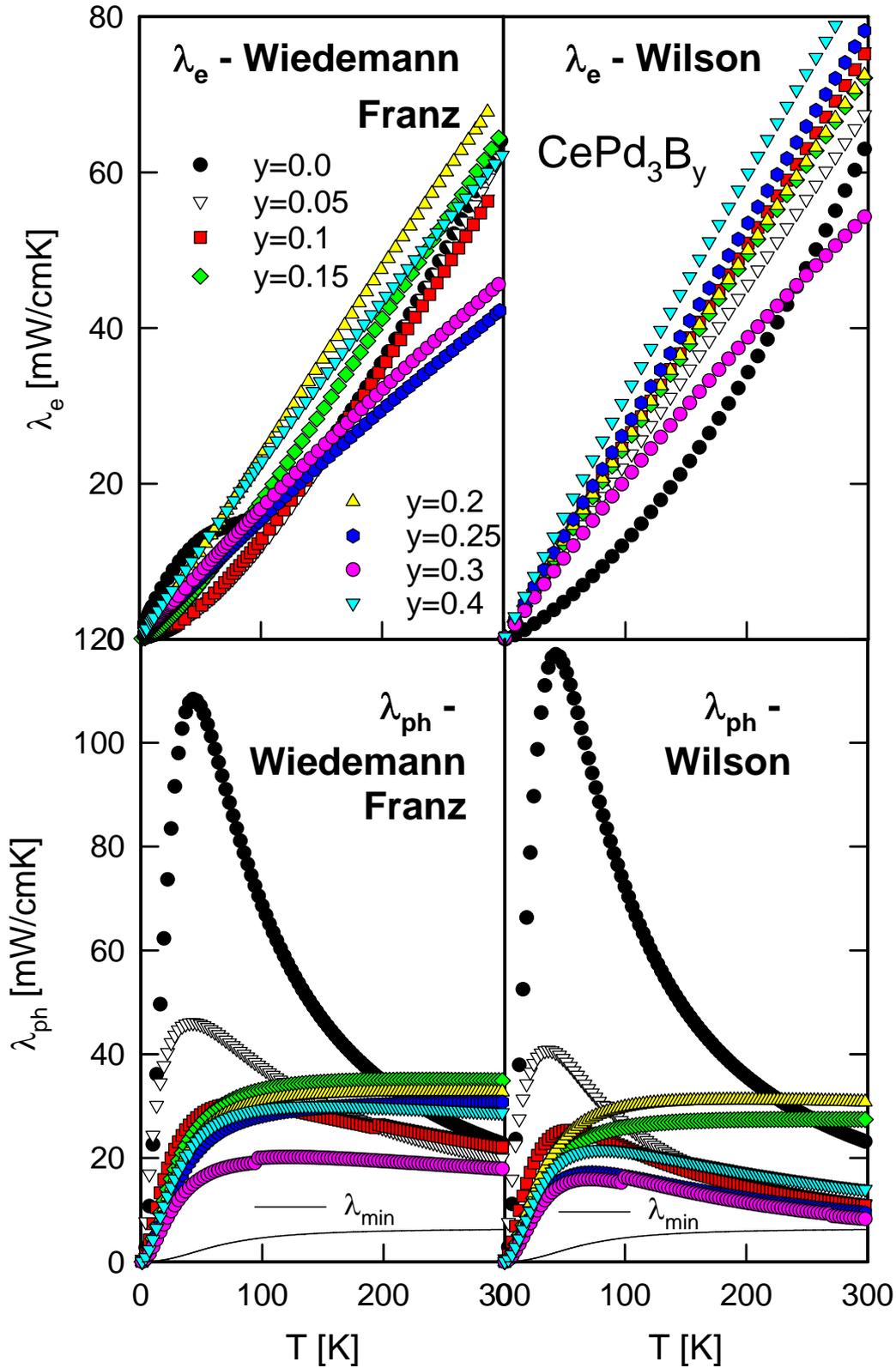


Figure 3.12: Comparison of $\lambda_e(T)$ and $\lambda_{ph}(T)$ gained by Wiedemann Franz law (left panels) and Wilson's equation (right panels). The curves for various B concentrations y in CePd_3B_y show a remarkably good agreement.

are reported in Fig. 3.11. θ_D tends to decrease with increasing B content. Interesting is the inflated value of about 350 K of pure CePd₃ which is reproduced by both procedures. θ_D calculations by C.-K. Loong et al. [60], who used the phonon density of states, resulted in a temperature dependent behavior, where θ_D decreases from ≈ 320 K at 0 K to ≈ 220 K at 70 K. From heat capacity measurements published by M.J. Besnus et al. [3] $\theta_D \approx 300$ K. The large discrepancy of θ_D at $y=0.05$ for the different models can not be ex-

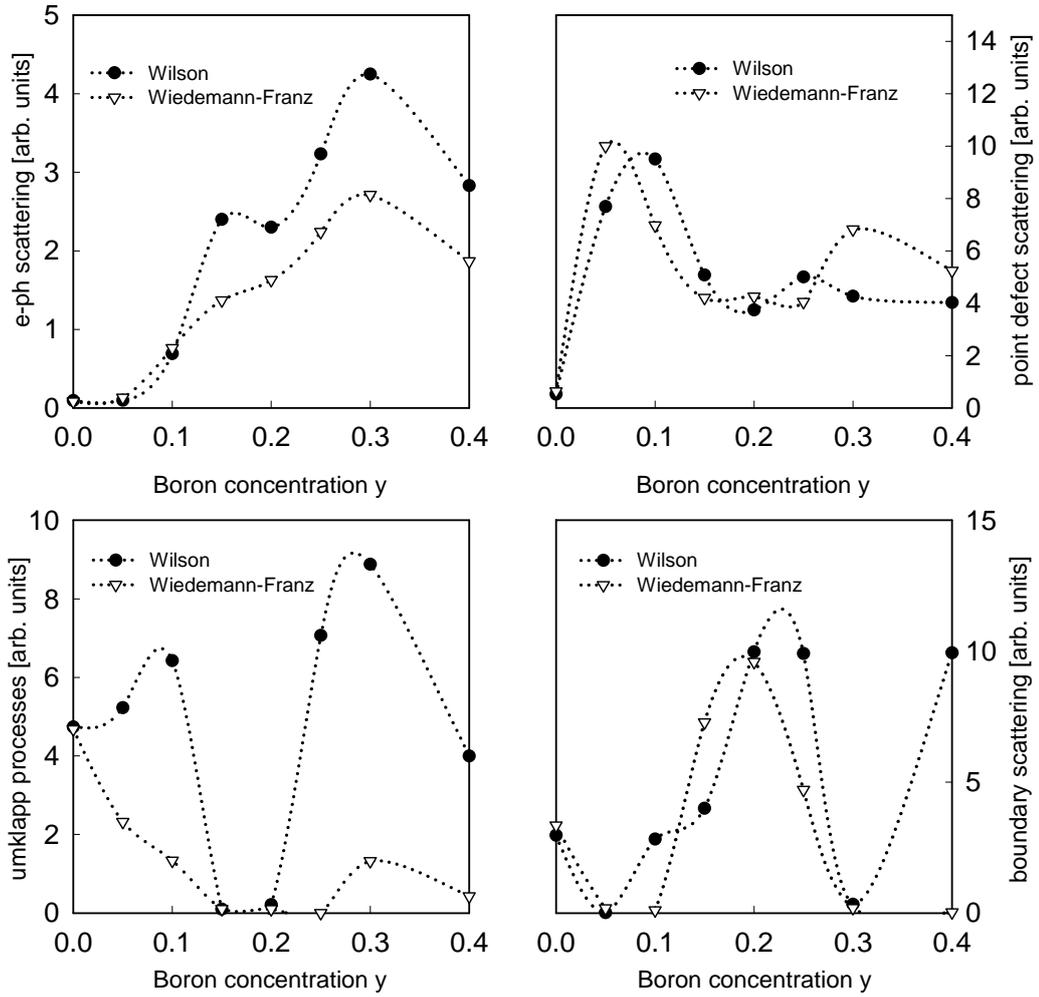


Figure 3.13: The four diagrams show the interrelationships between the B concentration y and the governing scattering mechanisms based on Callaway's model. The black circles represent values gained from treatment with *W-Eqn*, while the white triangles stand for data derived by *WF-l*. The dotted lines are a guide to the eye.

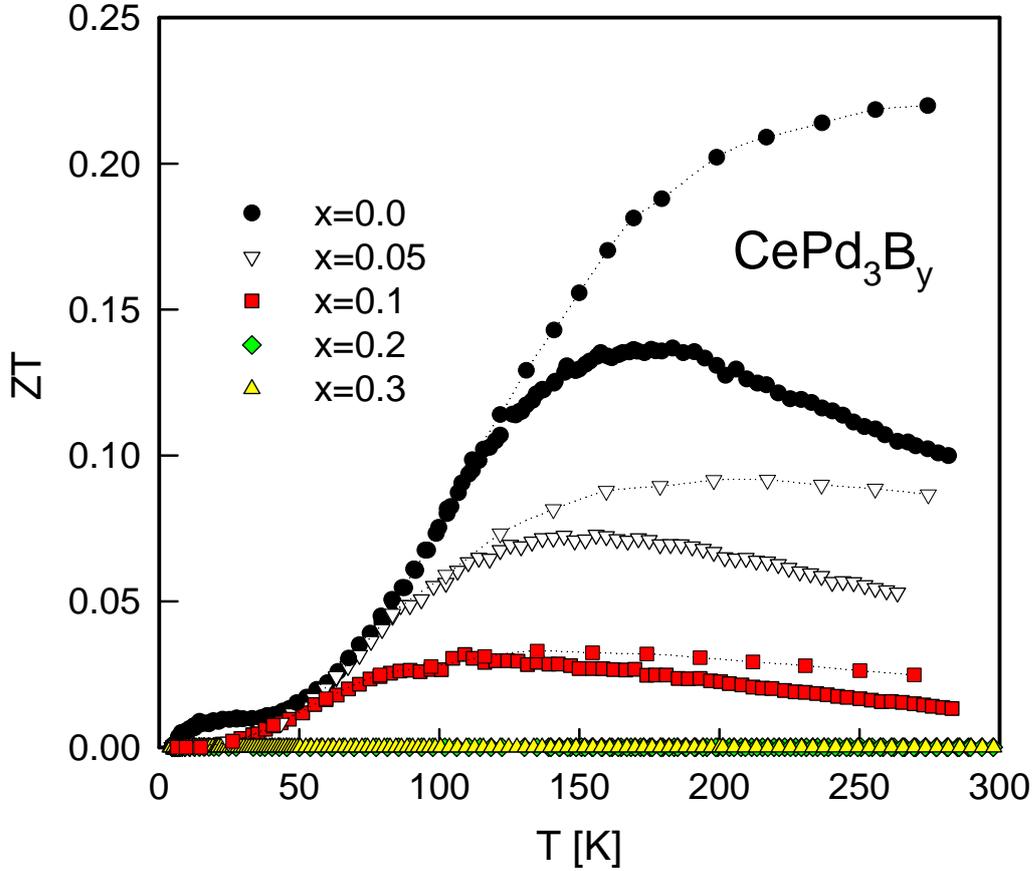


Figure 3.14: The thermoelectric figure of merit ZT of CePd_3B_y for various B concentrations y in dependence of the temperature. The solid symbols represent transport data taken from measurement, while the dotted lines regard a $\lambda(T)$ correction due to radiation losses data.

plained yet. We tried also to apply Wilson's model with starting values gained by $WF-l$ and vice versa, but the parameters were rather unstable. This problem was faced several times, although a general analogy is found comparing $WF-l$ with $W-Eqn$. The effect of B doping on the four principal scattering contributions is shown in Fig. 3.13, where arbitrary units are used to keep up convenience. The curvature of λ_{ph} gained by applying $WF-l$ on the measured data of $y=0.15, 0.2$ and 0.25 refers to a minor contribution of τ_U as it is also confirmed by Wilson's model for the two samples with lower B content. For $y = 0.25$ the parameters again become unstable. The data were fitted several times and it was not possible to reproduce the result of $WF-l$. Possibly this is a problem originated from the large number of fitting parameters. The fitting procedure results in a mathematically best match, which may be a

unphysical solution. A further uncertainty of both is that in fact $WF-l$ is not valid for Kondo-systems especially not for IV systems [30, 28, 27] and that $W-Eqn$ also does not take any magnetic or IV interactions into account.

3.2.4 Figure of merit

Finally the thermoelectric figure of merit ZT was calculated by applying equation 1.77 to the measured values of $S(T)$, $\rho(T)$ and $\lambda(T)$. Whereupon a second evaluation was done, using radiation corrected $\lambda(T)$ values. All data are illustrated in Fig. 3.14 and it becomes evident that doping with boron has no positive effect on the thermoelectric performance of CePd₃ as it was already anticipated from the Seebeck data. An improvement seems only possible by keeping the thermopower on a high level which means in this case to stay in the intermediate valence regime. Generally the figure of merit of CePd₃ exhibits a flat slope at lowest temperatures followed by an upturn, which shifts to lower temperatures as the Rh content increases. For the curve which is not corrected with respect to radiation losses, a maximum is formed at about 170 K. The introduction of B lowers the amplitude of ZT and shifts the maximum to lower temperatures. The corrected ZT -values increase monotonously with a slightly reduced slope without reaching a maximum up to room temperature. It has to be mentioned that there are several attempts with various dopants. Most of the group 13 and 14 elements form a superstructure of (CePd₃)₈M (M=Al, Ga, In, Si, Ge, Sn, Pb)[61] and a doping with Ga even increases ZT [54].

3.3 Ce(Pd_{1-x}Rh_x)₃

To examine the effects of substitution on the Pd site by Rh two sample sets were synthesized. In a first step the Rh concentration x was increased in steps of 0.2 with additional samples of $x = 0.1$ and $x = 0.9$. As thermoelectric interesting behavior was observed only for samples with $x < 0.2$ a second series with smaller Rh contents $x = 0.00, 0.03, 0.06, 0.09, 0.15$ was prepared. The pure CePd₃ sample was synthesized for the reason of comparability. In section 3.1 the differences between CePd₃⁽¹⁾ and CePd₃⁽²⁾ have already been discussed. The series shows a large discrepancy in the absolute values of transport properties as well as in parts of their curvature. Nevertheless a comparison of the samples and conclusions regarding the thermoelectric properties should be possible. By the substitution of Pd by Rh the Ce valence shifts toward 4+ [6], which drastically affects the thermoelectric properties of the compound. As mentioned earlier, the differences can not be figured out by X-Ray diffraction data, from which all samples are single phased and the lattice constants suit nicely together. One observes in Fig. 3.15 that the

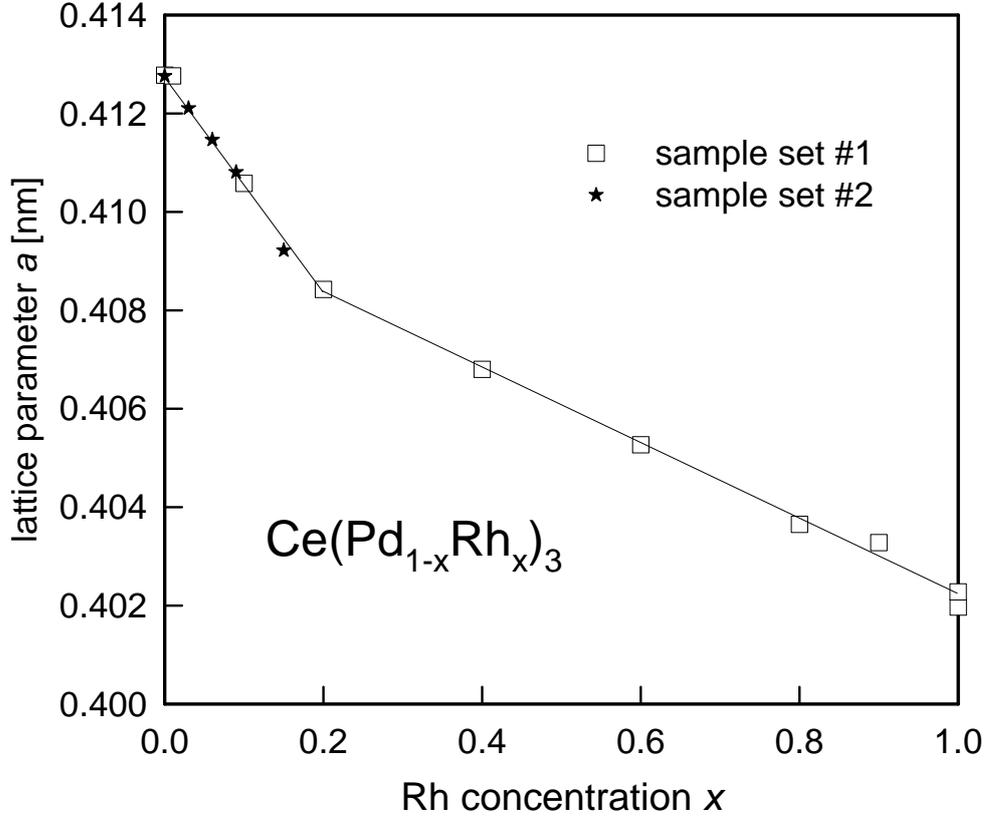


Figure 3.15: Lattice constant of $\text{Ce}(\text{Pd}_{1-x}\text{Rh}_x)_3$ in dependence of the Rh concentration x . The solid lines are a guidance for the eye.

extracted lattice parameter is reduced with increasing Rh content, but it does not follow Vergard's law of linearity, but shows a kink at a concentration of about $x=0.2$, which separates the line into two linear sections. This kink is a signature for reaching the 4+ valency of the Ce ion [8]. For samples with concentrations $x > 0.2$ transport properties evidence simple metallic behavior. $\rho(T)$ loses its Kondo-lattice peak and follows strictly a Bloch-Grüneisen law (eqn. 1.14). $S(T)$ decreases to normal metallic values and $\lambda(T)$ also shows a distinct change with concentrations higher than 0.2.

3.3.1 Electrical resistivity

The measured resistivity curves from 4.2 to 300 K for both sample sets as well as the fit curves generated by the *A.F.-model* are depicted in Fig. 3.16. As the stoichiometry of the CePd₃-basic material for the second sample set (from now on marked CePd₃⁽²⁾) is not ideal, its resistivity is generally higher

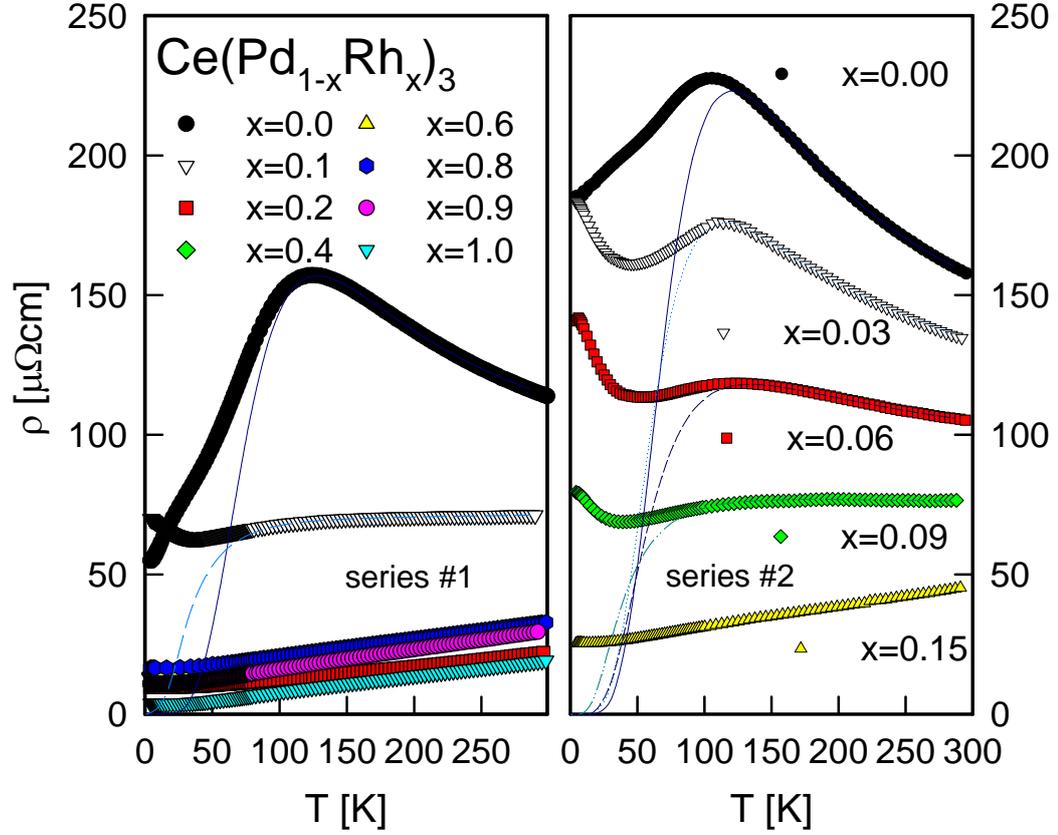


Figure 3.16: Temperature dependent resistivity $\rho(T)$ of $\text{Ce}(\text{Pd}_{1-x}\text{Rh}_x)_3$ for various concentrations of Rh. The left panel shows data from the first sample set. The right one displays the results of sample set #2. The solid lines are fit curves according to the *A.F.-model*.

than that of $\text{CePd}_3^{(1)}$ and the temperature dependence is slightly changed. The most evident difference is that for $\text{CePd}_3^{(2)}$ $\rho(290 \text{ K}) < \rho(4.2 \text{ K})$, while for $\text{CePd}_3^{(1)}$ $\rho(290 \text{ K})$ is about 3 times larger than $\rho(4.2 \text{ K})$. Furthermore, the maximum in $\rho(T)$ at 123 K for $\text{CePd}_3^{(1)}$ is slightly shifted down to 105 K for $\text{CePd}_3^{(2)}$. On the other hand, the resistivity data from the sample with $x = 0.09$, belonging to the second series, suits nicely to the one with $x = 0.1$ of the first set. Thus it can be concluded that the general effect of substitution can be attained using data from the second series. With lowest concentrations of Rh the resistivity is effectively reduced, T_{max}^ρ shifts to higher temperatures, while the amplitude of the peak diminishes and the negative slope of $\rho(T)$ above T_{max}^ρ becomes flatter. At lower temperatures a new minimum emerges and the resistivity increases with decreasing temperature. This negative slope at very low temperatures decreases with larger Rh content. The

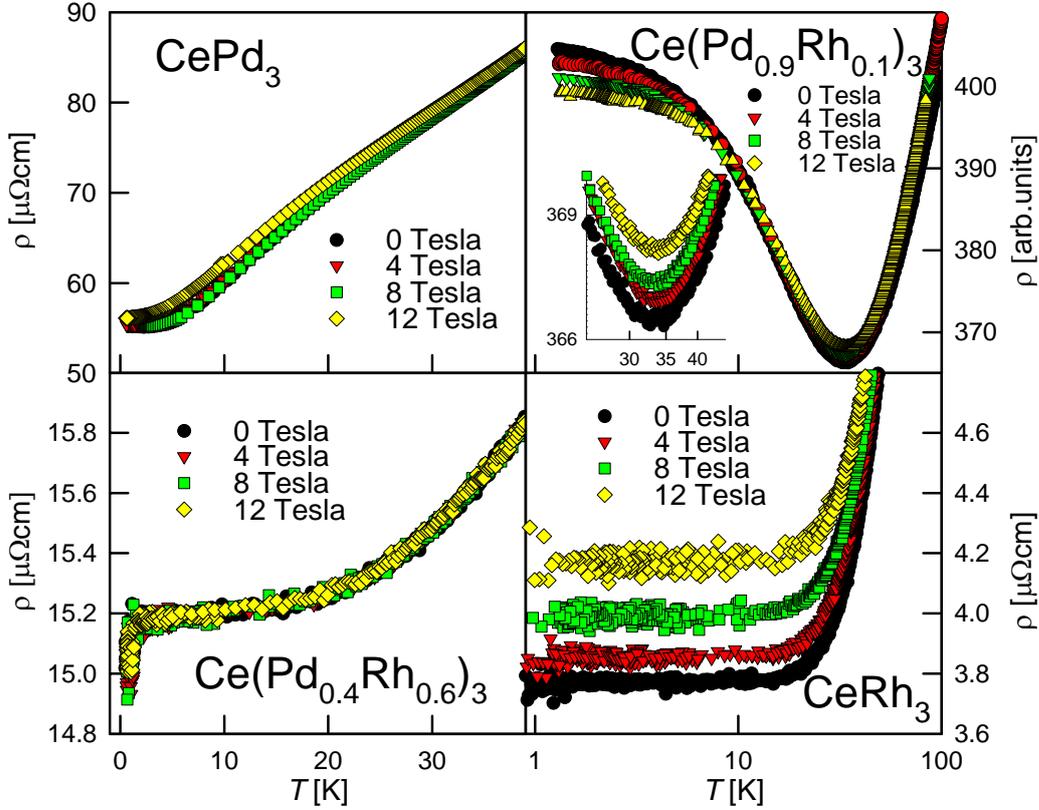


Figure 3.17: $\rho(T)$ measured at four constant magnetic fields on samples of $\text{Ce}(\text{Pd}_{1-x}\text{Rh}_x)_3$ with $x = 0, 0.1, 0.6$ and 1 . Remind that the right panel has a logarithmic temperature scale.

sample with $x = 0.09$ exhibits a positive slope of $\rho(T)$ above T_{max}^ρ and the former maximum forms only a weak shoulder. At Rh concentrations of $x \geq 0.2$ the curvature of $\rho(T)$ is suppressed, but the behavior does yet not follow the Bloch-Grüneisen-law. For concentrations $x \geq 0.4$ this law is applicable, but the slopes and residual resistances do not evolve according to the increasing Rh content. The increase of T_{max}^ρ , which should be proportional to the characteristic temperature T_K , was expected as the valence shifts toward $4+$, but by fitting with the *A.F.-model*, decreasing characteristic temperatures T_0 and T_f are extracted. The characteristic temperatures and scaling parameters achieved by the procedure are depicted in Fig. 3.20, where they are compared to values extracted from thermopower data fitting.

Magnetic field dependence of the electrical resistivity

The influence of an external magnetic field B up to 12 T on the resistivity $\rho(T)$ down to 0.5 K was also measured for the first series. The effect, which is rather small, is depicted in Fig. 3.17 for the samples with $x=0, 0.1, 0.6$ and 1. The electrical resistivity of CePd₃ (left upper panel) is almost unaffected by the magnetic field over the whole temperature range. The $\rho(T)$ -curvature of Ce(Pd_{0.9}Rh_{0.1})₃ (right upper panel) is reduced. T_{min}^ρ keeps approximately 35 K and the value of ρ_{min} increases; furthermore the resistivity decreases at temperatures below 10 K with increasing magnetic field. From 4.2 to 300 K the sample with $x = 0.6$ shows a simple metallic behavior, but below 2 K some ordering takes place (lower left panel), which was not observed so far for any other sample. The magnetic field has only small influence on the $\rho(T)$ -curvature of this sample. Pure CeRh₃ also follows Bloch-Grüneisen-law over the whole temperature range, but below 35 K the sample has a positive magneto resistance (lower right panel), as it can be expected for a simple metal.

Pressure dependence of the electrical resistivity

External pressure should reduce the elementary cell volume and therefore drive the Ce valency toward the 4+ state, consequently the $\rho(T)$ behavior under increasing pressure is estimated to resemble the performance with increasing Rh content. Pressure dependent measurements are very elaborate and often the experiment fails. Two samples with concentrations of $x = 0.1$ and $x = 1$ were measured successfully over the complete attainable pressure range. The achieved data are displayed in Fig. 3.18 where one can see the $\rho(T)$ behavior of CeRh₃ in the left panel. The resistivity curves follow Bloch-Grüneisen-law and by fitting $\rho_0(p)$ was extracted. The inset in the left panel of Fig. 3.18 visualizes the linear decrease of ρ_0 with increasing pressure. The structure of $\rho(T)$ of Ce(Pd_{0.9}Rh_{0.1})₃ keeps unchanged with increasing pressure, but ρ_{min} at about 30 K and ρ_0 are diminished relative to $\rho(290\text{ K})$ (Fig. 3.18 right panel).

3.3.2 Thermopower

The thermopower data $S(T)$ are visualized in Fig. 3.19 and again the difference between the two production series is evident. The $S(T)$ -values of the second charge, which are depicted in the right panel, are lower, than that of the first (left panel). $S_{max} \approx 106\ \mu\text{V/K}$ of CePd₃⁽¹⁾ at $T_{max}^S \approx 135\text{ K}$ while CePd₃⁽²⁾ has its maximum at approximately the same temperature but only with $S_{max} \approx 92\ \mu\text{V/K}$. Most remarkable is the fact that with a substitution of $x = 0.03$ the $S_{max;(x=0.03)} \approx 112\ \mu\text{V/K}$, which is even higher than

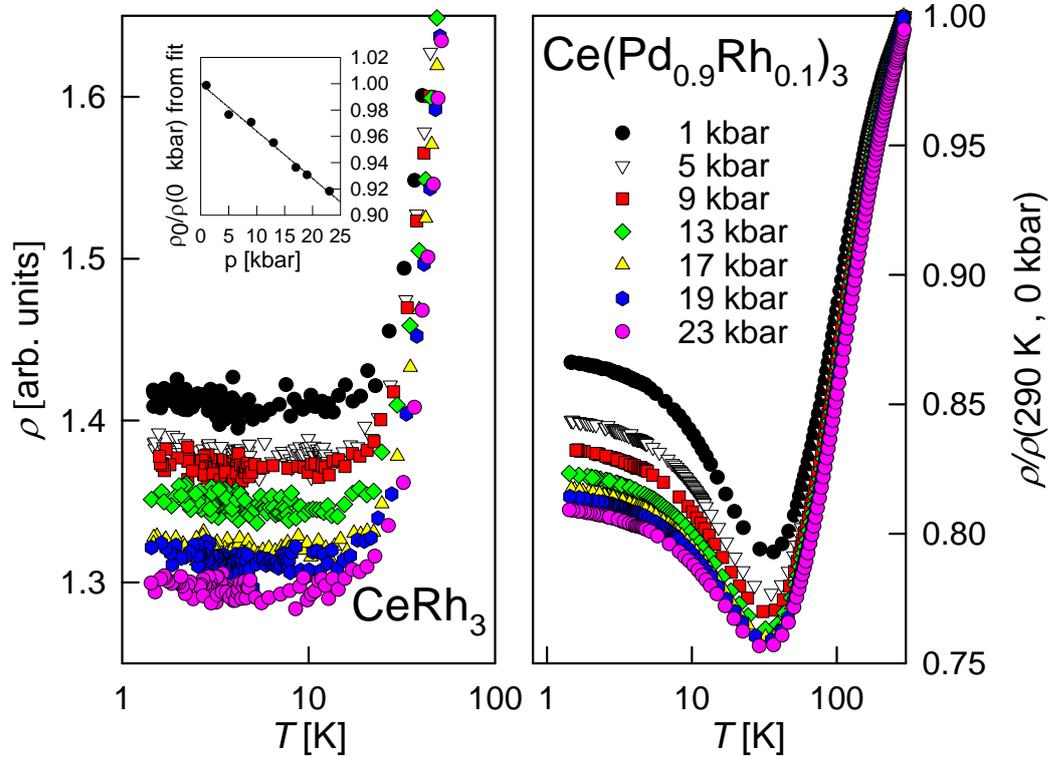


Figure 3.18: Pressure dependent $\rho(T)$ of $\text{Ce}(\text{Pd}_{1-x}\text{Rh}_x)_3$ for $x = 0.1$ and 1

the value of the pure $\text{CePd}_3^{(1)}$. Assuming that substitution has in percentage the same enhancement on more stoichiometric samples S_{max} -values of about $125 \mu\text{V}/\text{K}$ would result. The shift of T_{max}^S toward lower temperatures, as it was measured for increasing Rh concentrations up to $x = 0.06$ is unexpected, as it points to decreasing T_K values, but also the analysis of the resistivity data gives comparable results. Applying the *A.F.-model* as well as the *M.K.-model* reveals slightly decreasing characteristic temperatures for increasing Rh concentrations up to 0.09 followed by a step increase for $x = 0.15$ as it is depicted in Fig. 3.20. Due to this boost of the characteristic temperatures the maximum in $S(T)$ shifts to about 620 K for $x = 0.2$. The inset of the left panel of Fig. 3.20 maps the $S(T)$ -behavior from 4 to 900 K of the three samples with lowest Rh concentration of the first series. One sees that for $x=0.2$, T_{max}^S is shifted to 600 K. The models show a good agreement of thermopower and resistivity data. With higher Rh concentrations ($x \geq 0.4$) the magnitude of $S(T)$ becomes very small and negative over the whole measured temperature range with many structures in the curvature. Further increasing the Rh concentration enhances the $S(T)$ -values and for CeRh_3 the thermopower becomes positive for $T > 30$ K.

Second peak extension to *A.F-model*

The low temperature behavior of $S(T)$ is not well described by both, the *A.F-model* and the *M.K-model*. In fact the data from low temperatures were not used for the fit procedure. Examining the ascending curves of the thermopower of the different Ce(Pd_{1-x}Rh_x)₃ samples (Fig. 3.19) one might guess that the distinct shoulder of CePd₃⁽¹⁾ and CePd₃⁽²⁾ is shifted to higher temperatures and exhibits an enhanced amplitude with increasing Rh content. It seems as there sits a second maximum in the proximity of the main one. As there exist studies which propose two energy scales in CePd₃ [62, 63], we have tried to interpret the data as two superimposed peaks due to two characteristic temperatures. Following the *A.F-model*, we introduced formulae as

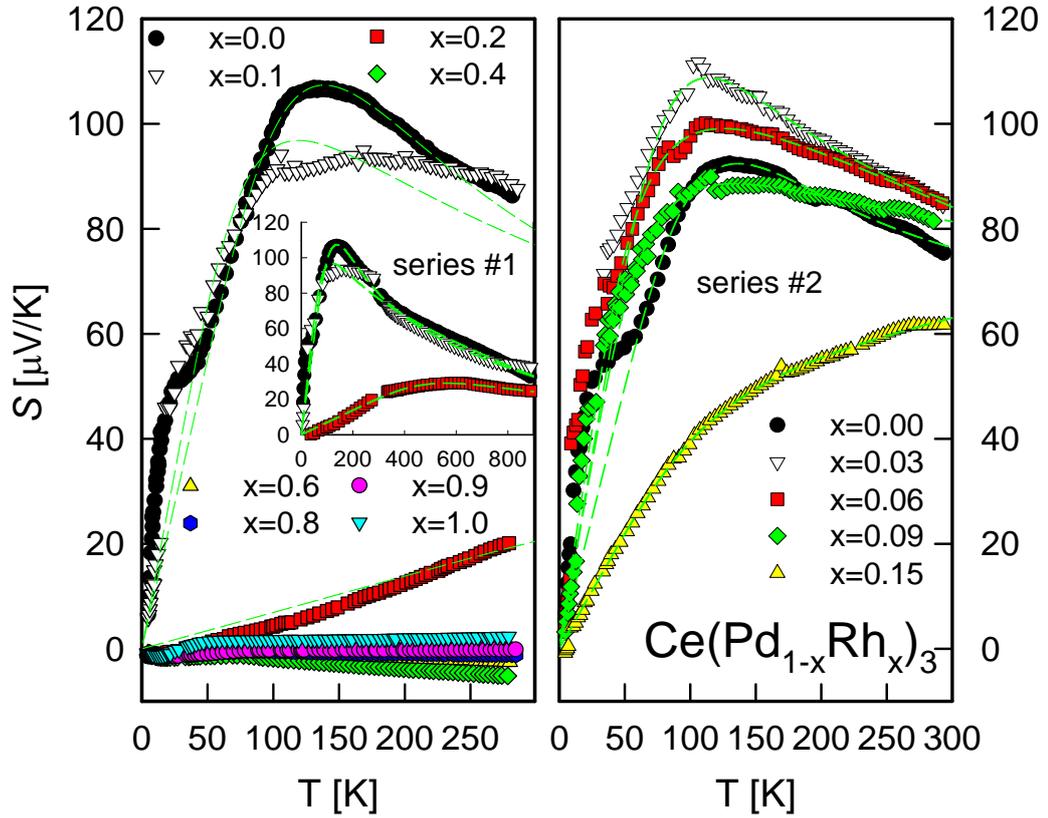


Figure 3.19: $S(T)$ of Ce(Pd_{1-x}Rh_x)₃ for various concentrations of Rh. The left panel denotes the results for the first sample series. The inset displays $S(T)$ of the three lowest Rh concentrations from 4 to 900 K. The right figure shows the data for the second series. The dashed green lines are fit curves based on the *A.F-model*.

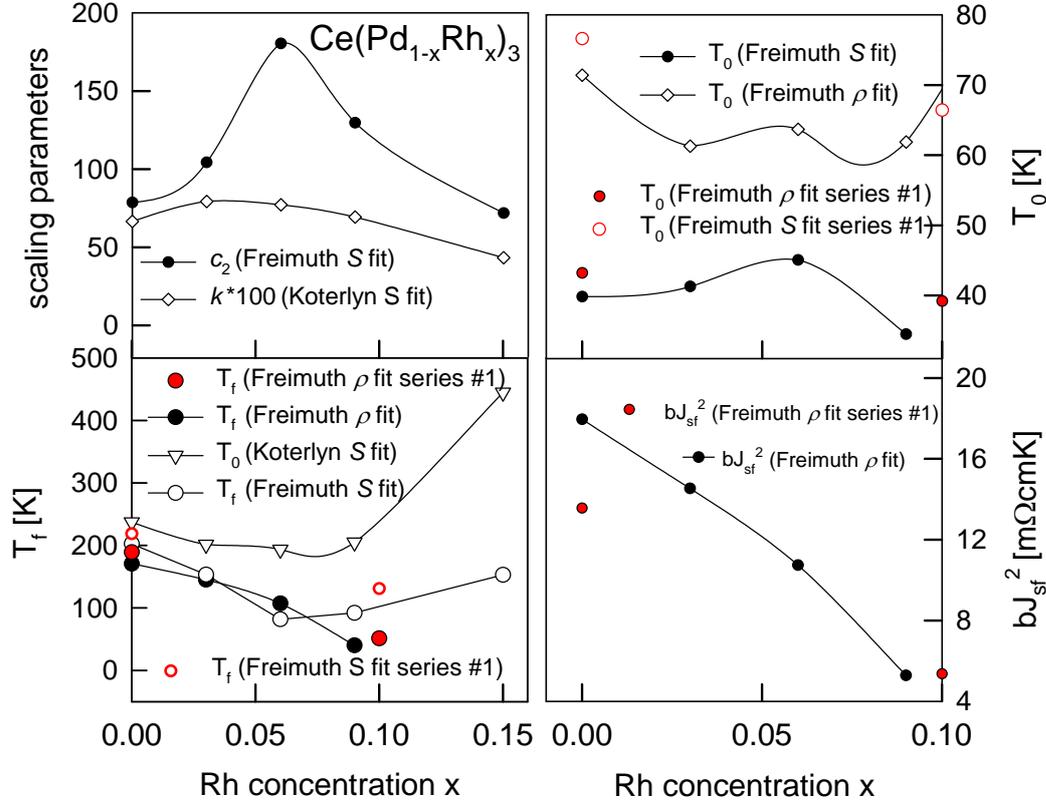


Figure 3.20: These three diagrams show the characteristic temperatures and scaling parameters extracted by applying the *M.K-model* and the *A.F-model* to thermopower and electrical resistivity data.

follows:

$$W_i(T) = T_{f,i} \exp(-T_{f,i}/T) \quad (3.2)$$

$$S_f(T) = c_1 * T + c_{2,1} * \frac{TT_{0,1}}{T_{0,1}^2 + W_1(T)^2} + c_{2,2} * \frac{TT_{0,2}}{T_{0,2}^2 + W_2(T)^2} \quad (3.3)$$

In Fig. 3.21 the results of this attempt are displayed. It is evident that one can fit the thermopower over the whole temperature region. The right shoulder of $S(T)$ is not affected by this method and the left is reproduced nicely. Inspecting the contributions of the three terms in Eqn. 3.3 to the total thermopower of $x = 0.0$ and $x = 0.06$ one detects, that a negative value of c_1 is essential to compensate the increasing values of thermopower due to the second and third term. The fit by the simple *A.F-model* generates even more negative linear contributions. By comparing the fit-parameters of both fit procedures as they are depicted in Fig. 3.22 one can learn, that taking a second peak into account does not change the general behavior of the

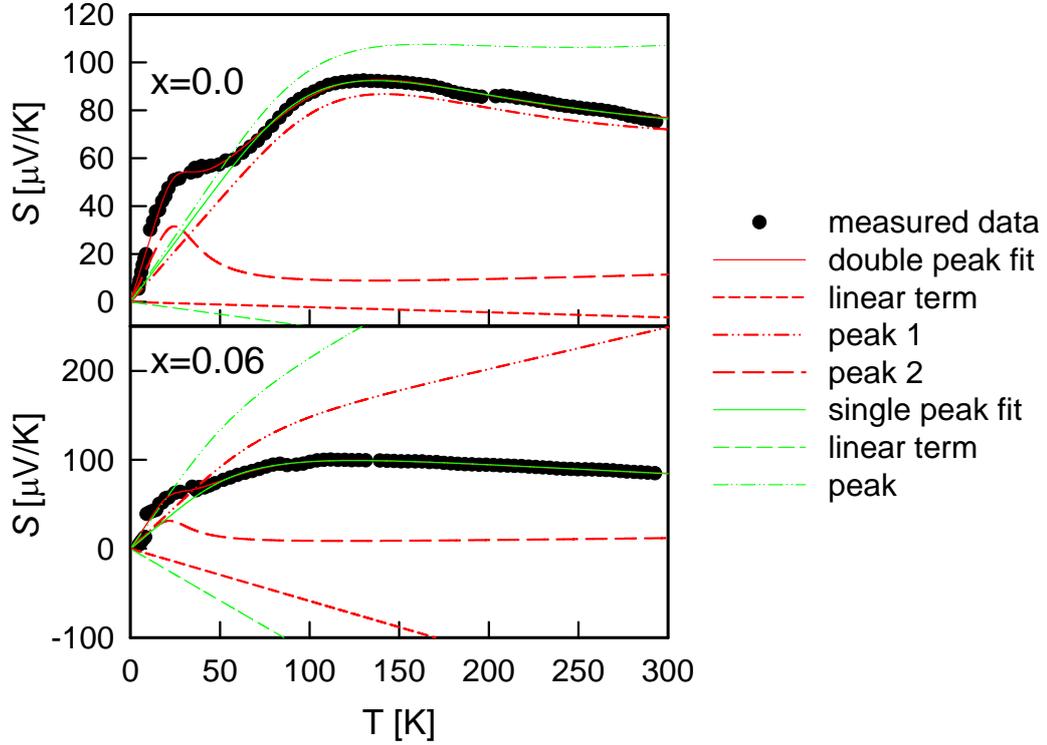


Figure 3.21: The upper and lower diagram show the results of fitting sample $x=0$ and $x=0.6$, respectively, using Eqn. 1.64 (green) and Eqn. 3.3 (red). Additionally the contributions due to the three terms of Eqn. 3.3 are depicted.

parameters describing the main peak and also the second peak parameters tend to follow the dependence of the main peak with reduced amplitude. It has to be emphasized again that also by interpreting the data using this method leads to a diminishing characteristic temperature T_f with increasing Rh content up to 6%, while T_0 stays rather constant. We have also tried to apply double peak fitting on the resistivity data but no improvement of reproducibility was gained.

3.3.3 Thermal conductivity

The acquired data of the thermal conductivity does not show differences of the sample sets due to dissimilar stoichiometry, as the curves of both series match each other nicely. Therefore the data were put together in Fig. 3.23. The left panel displays all curves as they were measured, while the right diagram denotes the $\lambda_{ph}(T)$ -curves of samples with $x \leq 0.2$ which were achieved by applying $WF-l$. With increasing Rh content up to $x = 0.1$ the maximum of $\lambda(T)$ at about 50 K is effectively suppressed, while the curvature beyond

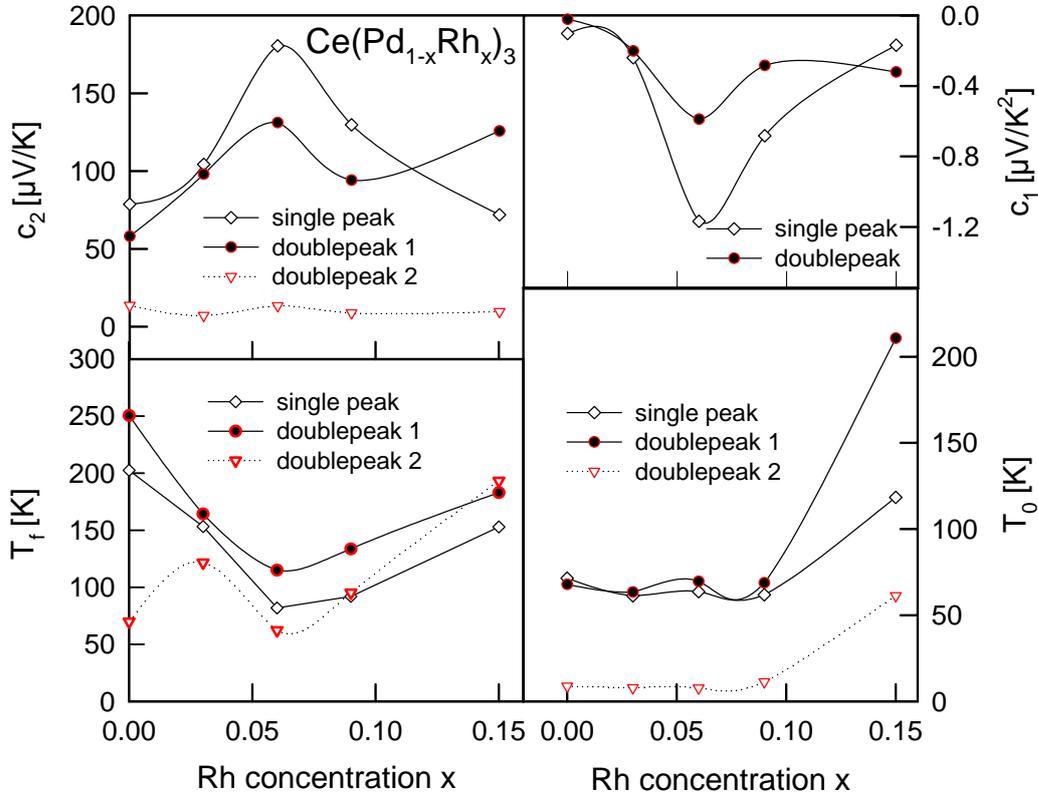


Figure 3.22: The four figures give a comparison of the evolution of fit-parameters according to Eqn. 1.64 and Eqn. 3.3 with increasing Rh content.

10 K keeps more or less unchanged. Still, λ_{min} , which is mapped in the right panel of Fig. 3.23, is about three times smaller at room temperatures and at T_{max}^λ it lies even 60 times lower. Additional Rh substitution results in a steep increase of $\lambda(T)$ and a general change of the behavior. For $x > 0.2$ the magnitude of the curves decreases again, but like for the electrical resistivity a distinct tendency is missing. The data of the first series have been treated using both fit-procedures, which are based on the $WF-l$ and $W-Eqn$, in addition to Callaway's model. The second sample set has only been analyzed in terms of $WF-l$. The extracted scattering parameters were normalized according to their value at $x = 0$ and are depicted in Fig. 3.24. The most apparent feature seen in this figure is the high congruence of the data for point defect scattering. The scattering rate due to this mechanism grows rapidly with increasing Rh content up to about 10% and with more Rh substitution this scattering contribution is reduced again. Also the boundary scattering parameter is well reproduced for both series and the different models. The oversized value for $x = 0.03$ may be a artificial compensation of the step

decay produced for the electron phonon scattering. Only by the fitting according to $WF-l$ such a decline of this scattering mechanism is produced. However, the analysis in the scope of $W-Eqn$ construes an shallow upward trend. From this data a theory, that valence fluctuations should significantly increase the electron-phonon scattering [31] can not be proven. Also for the umklapp processes the two models exhibit a different development with increasing Rh percentage. A possible explanation for this behavior may be that in Wilson's model this parameters have to compensate a misinterpretation of the electronic contribution to the thermal conductivity. The smaller values of the umklapp processes at 3 and 6% Rh content may be due to an oversized interpretation of radiation losses for this samples, because in the left panel of Fig. 3.23 one sees that the $\lambda_{tot}(T)$ -curves fall together at high temperatures but on the right panel the $\lambda_{ph}(T)$ -curves for $x = 0.03$ and 0.06 do not follow

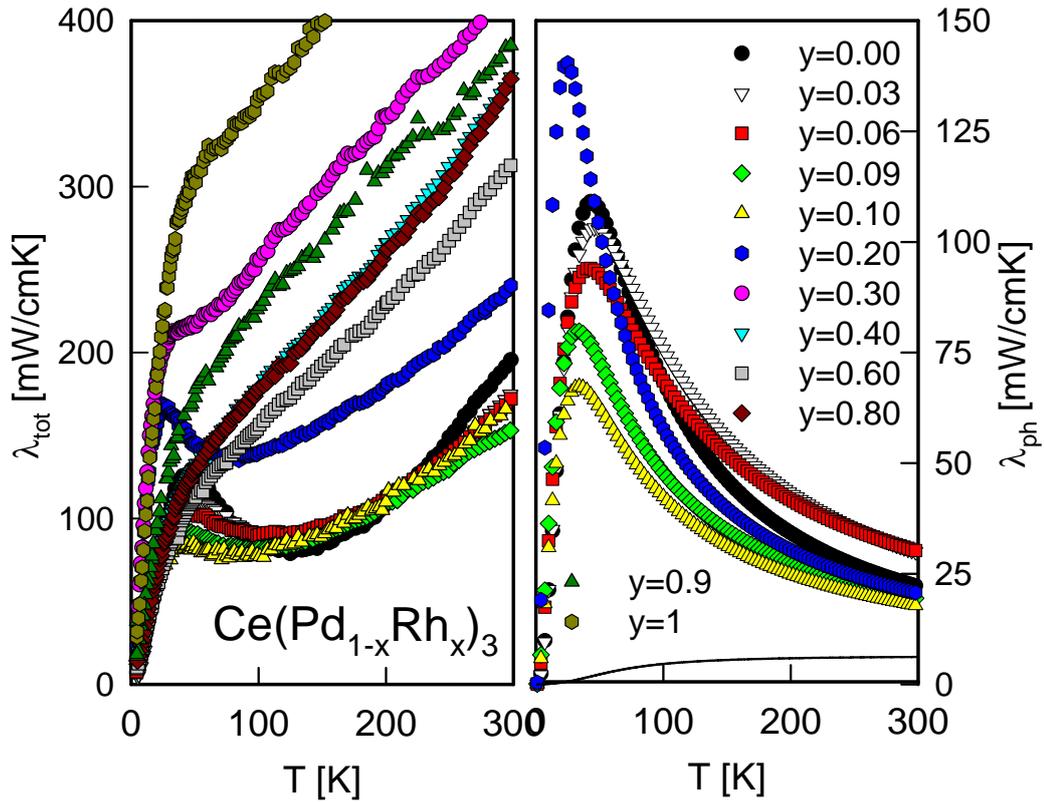


Figure 3.23: The left panel shows the measured data $\lambda_{tot}(T)$ of $\text{Ce}(\text{Pd}_{1-x}\text{Rh}_x)_3$ in dependence of the Rh concentration x (not radiation loss corrected). The right panel pictures $\lambda_{ph}(T)$ curves generated by applying the $WF-l$ including a radiation loss correction. The solid line corresponds to the calculated λ_{min} for CePd_3 .

the trend. Despite some trials with changing starting values, the fit-algorithm always ended at this values. In Fig. 3.25 the dependence of θ_D to the Rh concentration is marked. A general agreement can be found comparing the two fit-models and also the data for the second sample set suits nicely into the picture. The high θ_D -value for CePd₃ is reproduced for all curves and a general decrease is construed consistently.

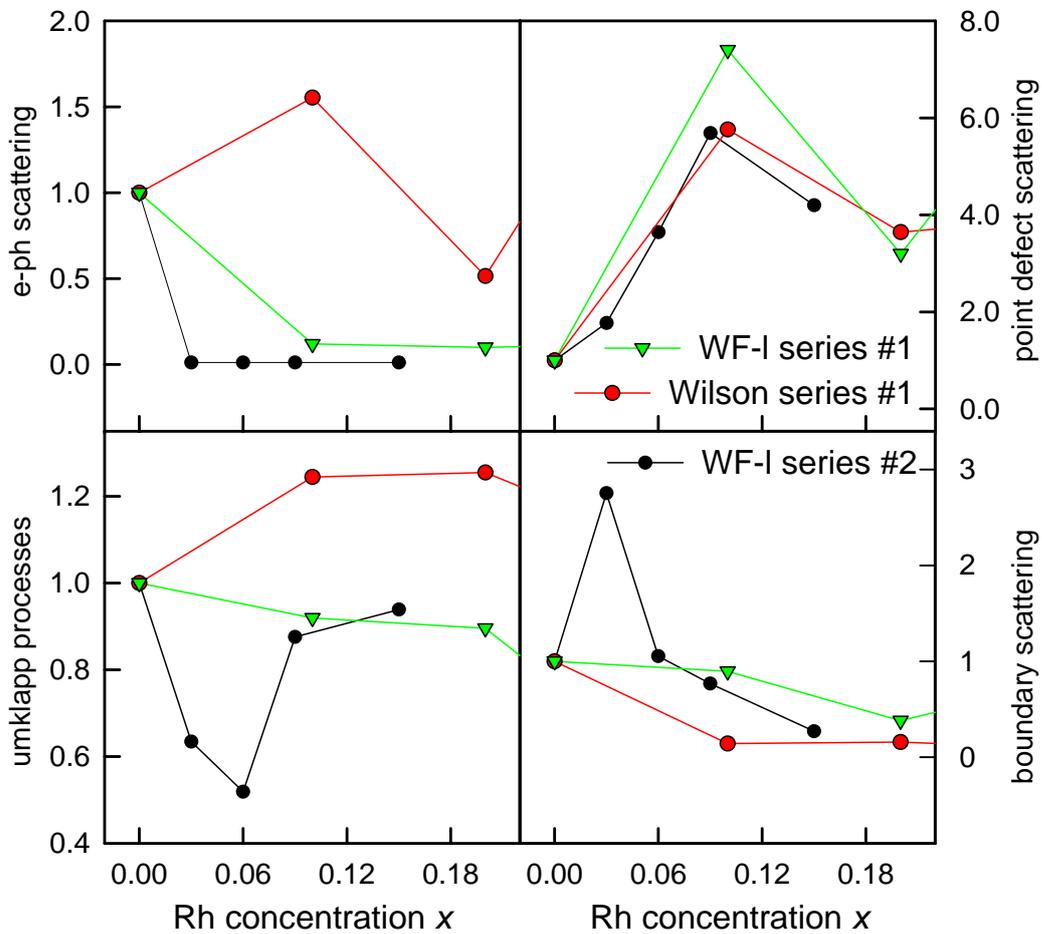


Figure 3.24: The four diagrams denote clockwise the scaling parameters of electron-phonon, point defect and boundary scattering and umklapp processes in dependence of the Rh concentration x . The green and black lines represent data from the first and second sample set, respectively, fitted according to *WF-l*. The red curves mark parameters of the first series on the bases of *W-Eqn*.

3.3.4 Figure of merit

For all samples the temperature dependence of the figure of merit ZT was calculated according to Eqn. 1.77. First, the measured data were put into the formula without radiation correction of $\lambda(T)$, then the corrected values were also used. The results are drawn in Fig. 3.26, where it is evident, that ZT_{max} of CePd₃⁽¹⁾ (left panel) is about twice than that of CePd₃⁽²⁾ (right figure). Generally the figure of merit exhibits a flat slope at lowest temperatures followed by an upturn, which shifts to lower temperatures as the Rh content increases. For the curves which are not corrected to radiation losses, a maximum is formed at about 170 K. The corrected ZT -values of most of the samples increase monotonously with a slightly reduced slope until a maximum around 300 K is reached. Ce(Pd_{0.9}Rh_{0.1})₃, which belongs to the first sample set, reaches $ZT_{max}=0.255$ at $T=260$ K. This maximum is the highest measured ZT for the whole sample set. Focusing on the second sample set one sees that for $x \geq 0.9$, $ZT(T)$ increases steadily for rising Rh concentra-

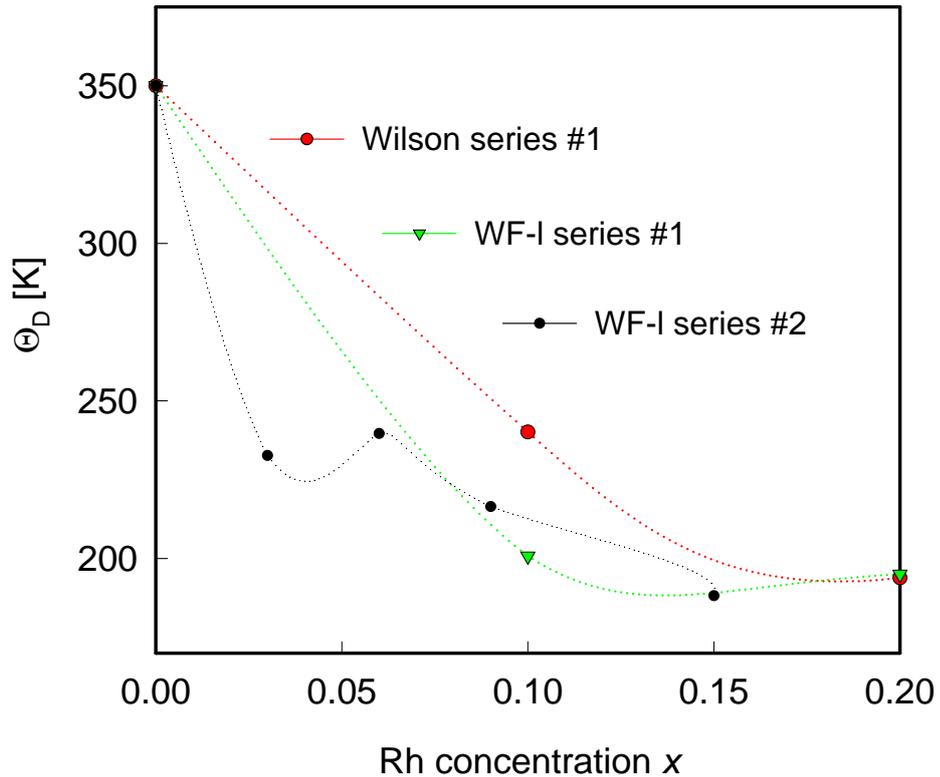


Figure 3.25: The green and black lines of this figure show the calculated values of θ_D according to $WF-l$ for the first and second sample set, respectively. The red curves plots the parameters of the first series on the bases of W -Eqn.

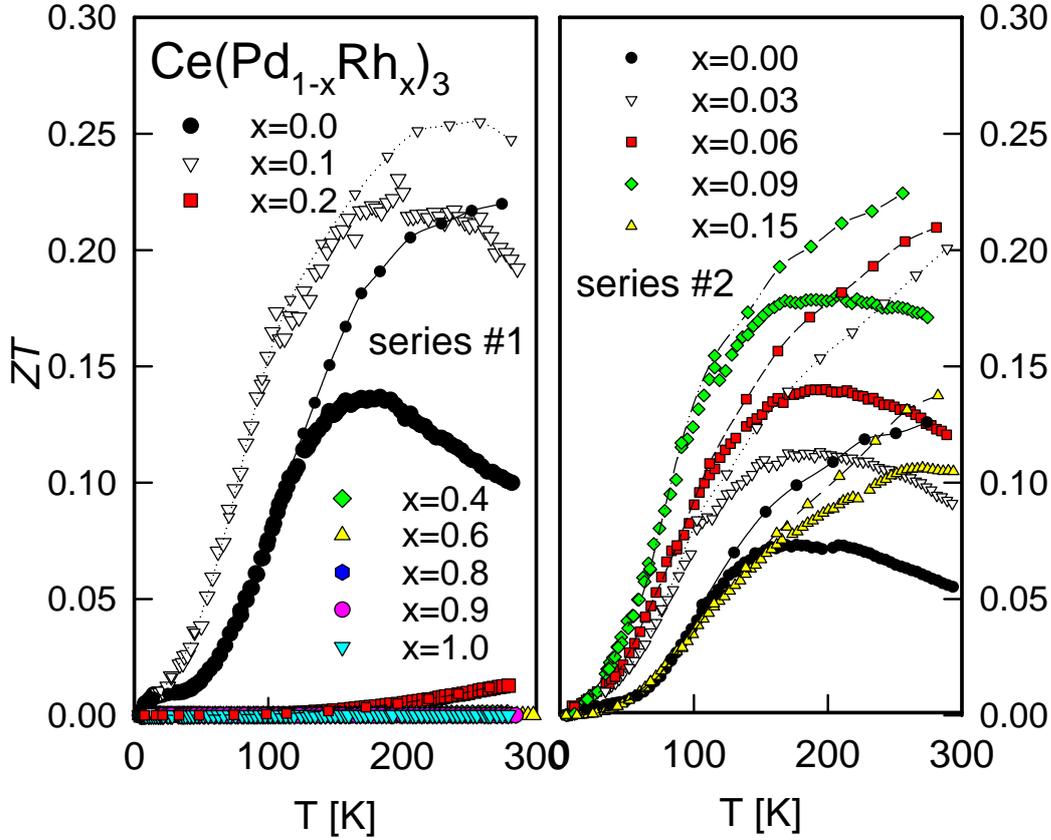


Figure 3.26: The left and the right diagram show the temperature dependence of ZT for sample set one and two, respectively. The lines with loose points denote the ZT taking a radiation correction of $\lambda(T)$ into account.

tion. For $x=0.9$ the room temperature value is almost doubled, but due to the low initial value it is still lower than ZT_{max} . For the samples $x=0.1$ and 0.09 the electrical resistivity and the thermal conductivity were nearly the same (compare Fig. 3.16 and Fig. 3.23, and only the absolute $S(T)$ values were different, while in relation to their CePd₃ base, the $x=0.9$ sample has a slightly higher thermopower (see Fig. 3.19). Having this in mind one concludes with caution that a substitution of Pd by Rh with $x \approx 0.09$ has the optimum effect on ZT .

3.4 Ce(Pd_{1-x}Rh_x)₃B_{0.05}

Conducted by the results of the previous sections a sample-set of Ce(Pd_{1-x}Rh_x)₃B_{0.05} was synthesized. It will be examined if it is possible to compensate the loss of thermopower due to B doping by the substitution of

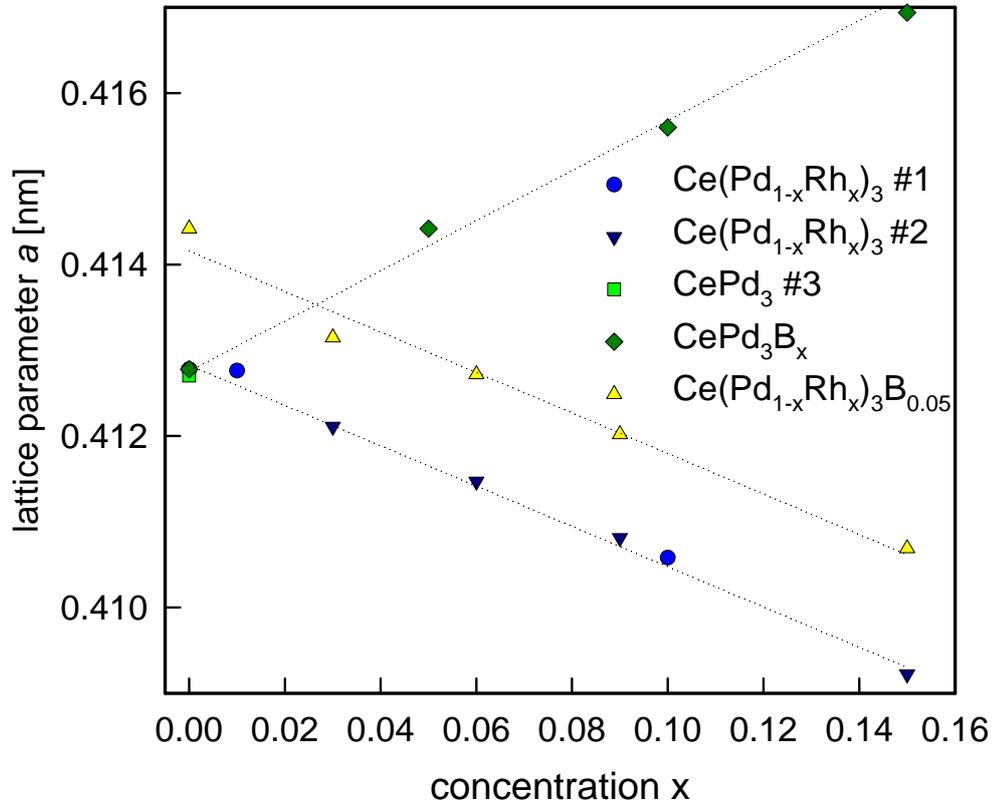


Figure 3.27: The diagram depicts the lattice constants of the $\text{Ce}(\text{Pd}_{1-x}\text{Rh}_x)_3\text{B}_{0.05}$ series in comparison with the former series. The dashed lines for $\text{Ce}(\text{Pd}_{1-x}\text{Rh}_x)_3$ and $\text{Ce}(\text{Pd}_{1-x}\text{Rh}_x)_3\text{B}_{0.05}$ are nearly exact parallel linear fits.

Pd by Rh without changing the low thermal conductivity. In other words the shift of Ce valency toward 3+ as a result of the B insertion should be reversed due to the Rh substitution. The series was synthesized using $\text{CePd}_3^{(2)}$ as basic material, thus the results are directly comparable to the results of the second $\text{Ce}(\text{Pd}_{1-x}\text{Rh}_x)_3$ series. On the basis of the X-ray diffraction data the samples are single phased and the lattice parameter shows a nearly linear decrease with increasing x as it is mapped in Fig. 3.27. The value for $x=0$ equals the value of $\text{CePd}_3\text{B}_{0.05}$ for the first sample set and the downward slope with increasing x is nearly exactly parallel to the decrease of the $\text{Ce}(\text{Pd}_{1-x}\text{Rh}_x)_3$ -series. From this affinity it seems true, that the B doping acts really as a negative offset of the Ce valency, which is again increased with increasing Rh content.

3.4.1 Electrical resistivity

The measured $\rho(T)$ behavior of this sample set is displayed in Fig. 3.28 where additionally the resistivity curves of CePd₃⁽¹⁾, CePd₃B_{0.05}⁽¹⁾ and CePd₃⁽²⁾ are mapped to enable comparison. As expected the electrical resistivity of the plain CePd₃B_{0.5} sample belonging to this sample set (CePd₃B_{0.05}⁽²⁾) is higher than the corresponding sample of the CePd₃B_y-series, but the relation between the resistivity curves of CePd₃B_{0.05}⁽¹⁾ to CePd₃⁽¹⁾ is equal to CePd₃B_{0.05}⁽²⁾ to CePd₃⁽²⁾. With increasing substitution of Pd by Rh T_{max}^{ρ} is shifted to lower temperatures and ρ_{max} is diminished in size. Normally this behavior can be interpreted by a decreasing Kondo temperature as it has been observed

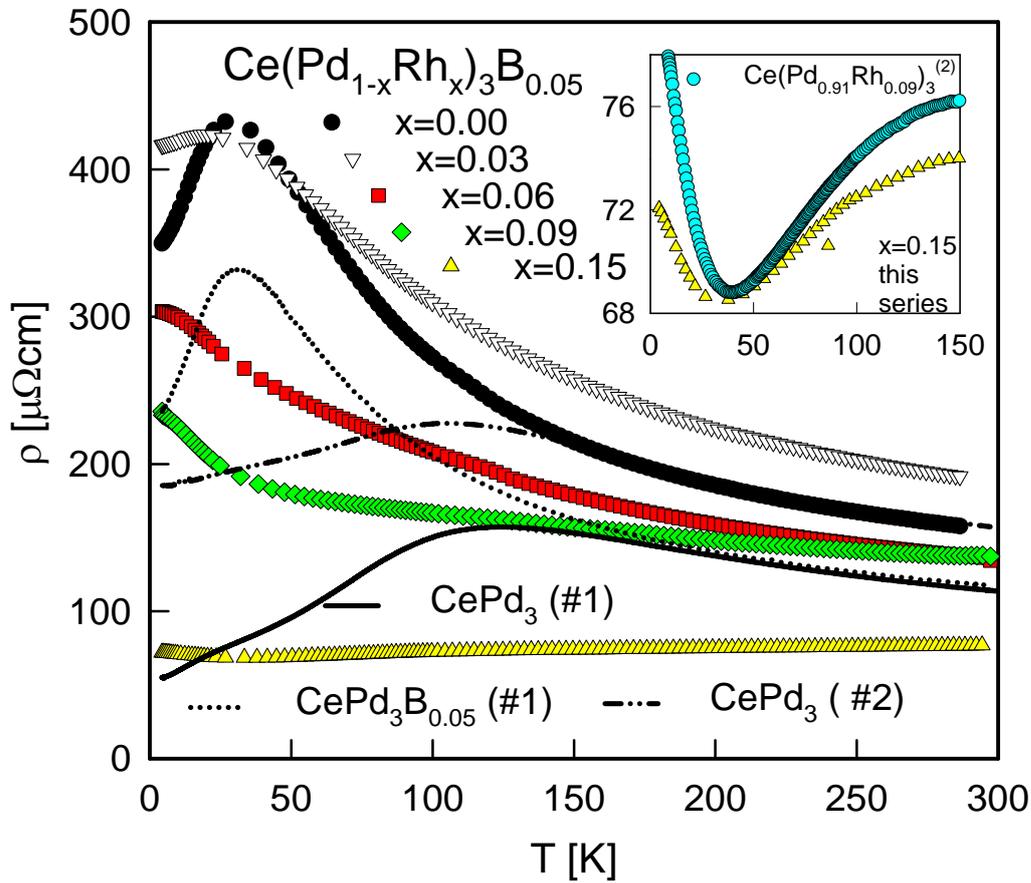


Figure 3.28: This diagram shows the measured $\rho(T)$ of the Ce(Pd_{1-x}Rh_x)₃B_{0.05}-series. Additionally the curves of CePd₃⁽¹⁾, CePd₃B_{0.05}⁽¹⁾ and CePd₃⁽²⁾ are displayed by the solid, the dotted and the dashed-double dotted line, respectively. The inset compares the $\rho(T)$ -behavior of sample Ce(Pd_{0.85}Rh_{0.15})₃B_{0.05} and Ce(Pd_{0.91}Rh_{0.09})₃⁽²⁾

in the $\text{Ce}(\text{Pd}_{1-x}\text{Rh}_x)_3$ -series. With $x=0.03$ the room temperature resistivity is increased about 20%, but a further enlargement of the Rh content leads to decreasing $\rho(T)$ values over the complete measured temperature range. $\text{Ce}(\text{Pd}_{0.85}\text{Rh}_{0.15})_3\text{B}_{0.05}$ exhibits a resistivity curve which strongly resembles $\text{Ce}(\text{Pd}_{0.91}\text{Rh}_{0.09})_3$ as can be seen in the inset of Fig. 3.28. This similarity in $\rho(T)$ may originate from a comparable Ce valency, which is also confirmed by the nearly equal lattice parameters of the samples. This would also corroborate the idea that the Ce valency which is lowered by the B doping is shifted back to higher values by the substitution with Rh. The slope of $\rho(T)$

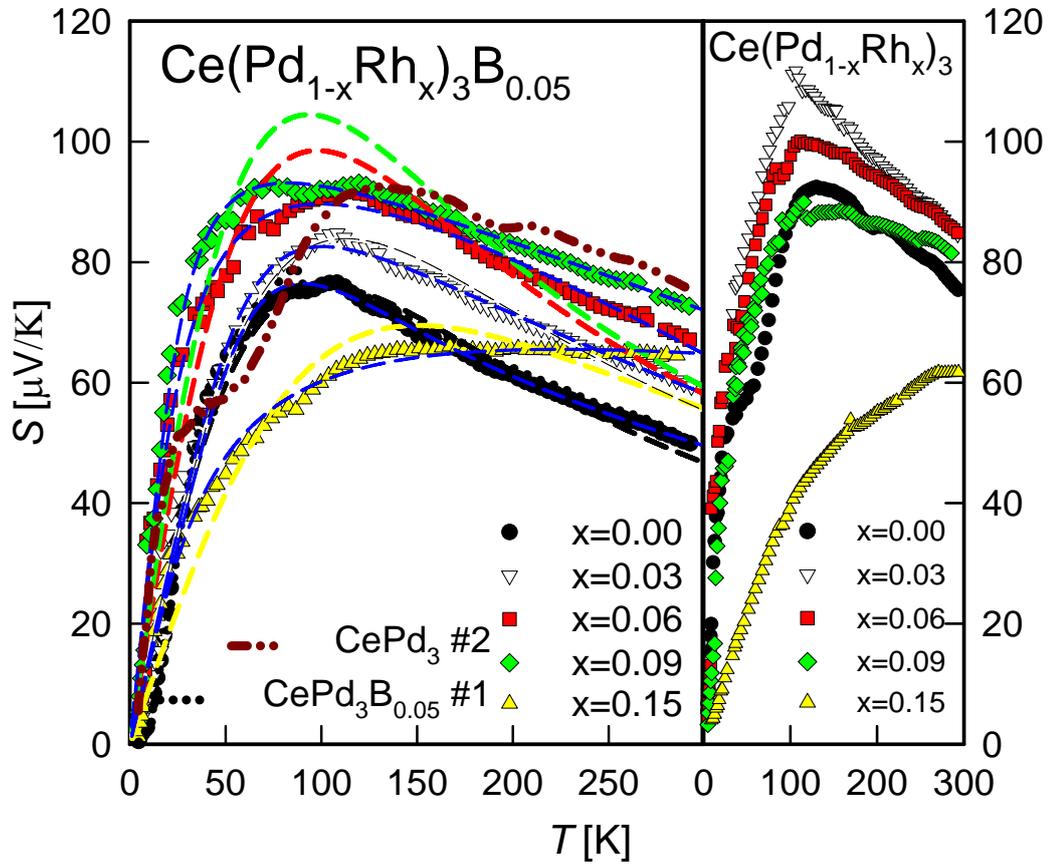


Figure 3.29: In the left panel the colored pointed lines show the $S(T)$ -behavior of the $\text{Ce}(\text{Pd}_{1-x}\text{Rh}_x)_3\text{B}_{0.05}$ -series. Additionally the fit curves generated with the $M.K$ -model model are denoted as colored dashed lines, while the blue dashed curves represent fit-curves by the $A.F$ -model. For comparison the data for $\text{CePd}_3^{(2)}$ (dark red, dash double-point) and for $\text{CePd}_3\text{B}_{0.05}^{(1)}$ (black pointed) are depicted. The right panel denotes the $S(T)$ -curves of the $\text{Ce}(\text{Pd}_{1-x}\text{Rh}_x)_3$ -series

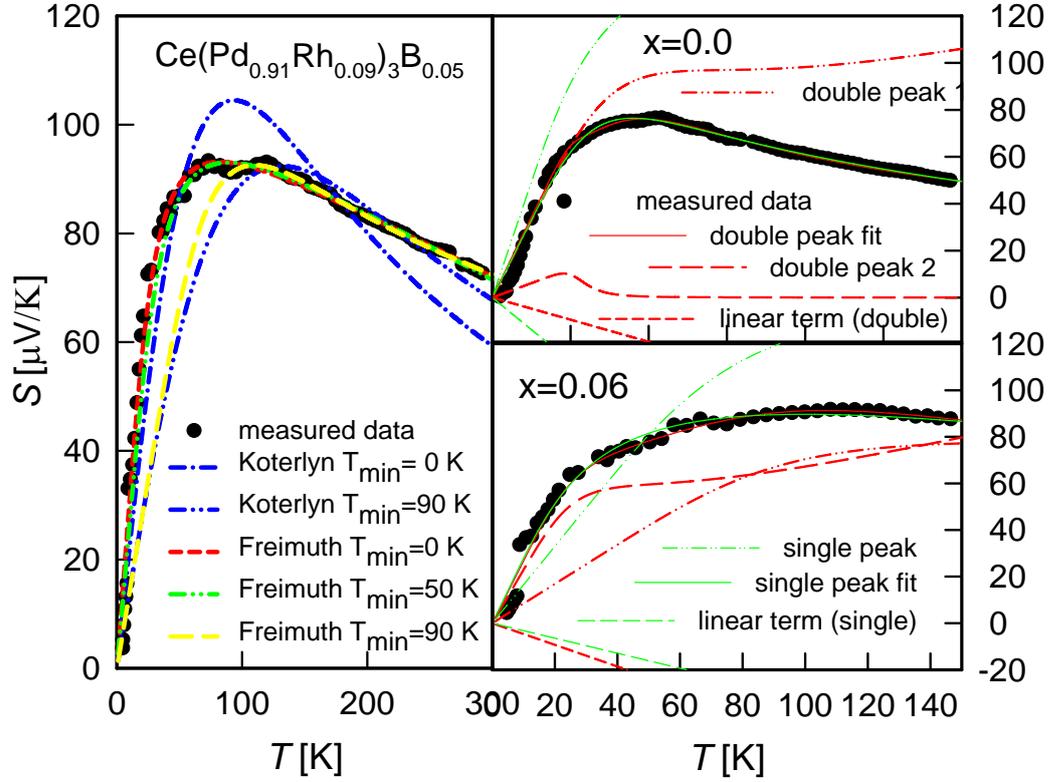


Figure 3.30: The left figure shows the effect of shifting the starting temperature of the data used for fitting. The diagrams on the right show the contributions of the single fit terms according to Eqn. 1.64 and Eqn. 3.3 .

with rising temperature decays logarithmically and can be fitted according to Eqn.3.1 for samples with $x \leq 0.06$, but the *A.F.-model* is not applicable, as it was not for the CePd₃B_y-series.

3.4.2 Thermopower

In Fig. 3.29 it can be observed that the thermopower of Ce(Pd_{1-x}Rh_x)₃B_{0.05} is enhanced over the whole temperature range with increasing Rh content up to $x = 0.09$ as it was expected. The $S(T)$ of Ce(Pd_{0.85}Rh_{0.15})₃B_{0.05} is strongly reduced in comparison to lower Rh concentrations, but it is larger than that of the corresponding sample without B doping. It shows a steep increase at low temperatures followed by a plateau from 120 K up to room temperature, where it reaches a value comparable to the sample with $x = 0.15$ without B doping (the resistivity of this sample resembled rather that of $x=0.09$). At temperatures below about 150 K the $S(T)$ -curves for $x \leq 0.09$ are even higher than that of the corresponding CePd₃⁽²⁾, but up to room tempera-

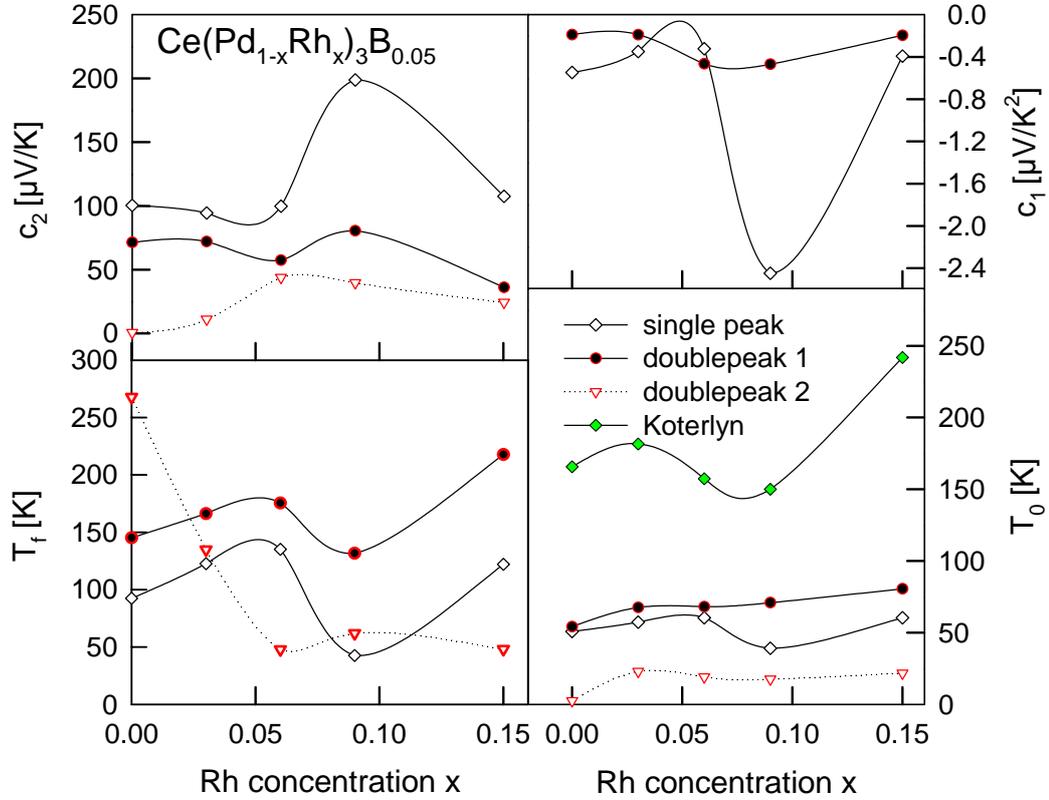


Figure 3.31: The diagrams show the development of the characteristic temperatures T_f and T_0 as well as the scaling parameter c_1 and c_2 the according to the *M.K-model* and the *A.F-model* using single- and double peak fitting .

ture the pure sample has the highest thermopower. A general comparison to the $\text{Ce}(\text{Pd}_{1-x}\text{Rh}_x)_3$ -series shows, that S_{max} is successively increased with increasing Rh content for $\text{Ce}(\text{Pd}_{1-x}\text{Rh}_x)_3\text{B}_{0.05}$ and recovers the values of pure CePd_3 nearly for $x=0.09$, while in the $\text{Ce}(\text{Pd}_{1-x}\text{Rh}_x)_3$ -series the thermopower is increased with the lowest prepared Rh concentration to the absolute maximum and only decreases over the whole temperature range with increasing Rh content and reaches the level of CePd_3 at a concentration of about $x = 0.09$. It remains an open question if the real maximum in $S(T)$ occurs at $x < 0.03$ or between $0.03 < x < 0.06$. The evolution of the $S(T)$ -curves with increasing Rh content of $\text{Ce}(\text{Pd}_{1-x}\text{Rh}_x)_3\text{B}_{0.05}$ exhibits some peculiar features. With 10% Rh substitution the slope at $T = 0$ is nearly the same as for $x = 0.00$ and T_{max}^S is shifted to higher temperatures. A further enhancement of Rh increases the slope at $T = 0$ and T_{max}^S is reduced while the width of the maximum is increased. One sees indications that the same double peak structure as described in the section 3.3.2 is present in this sample series, too. The low

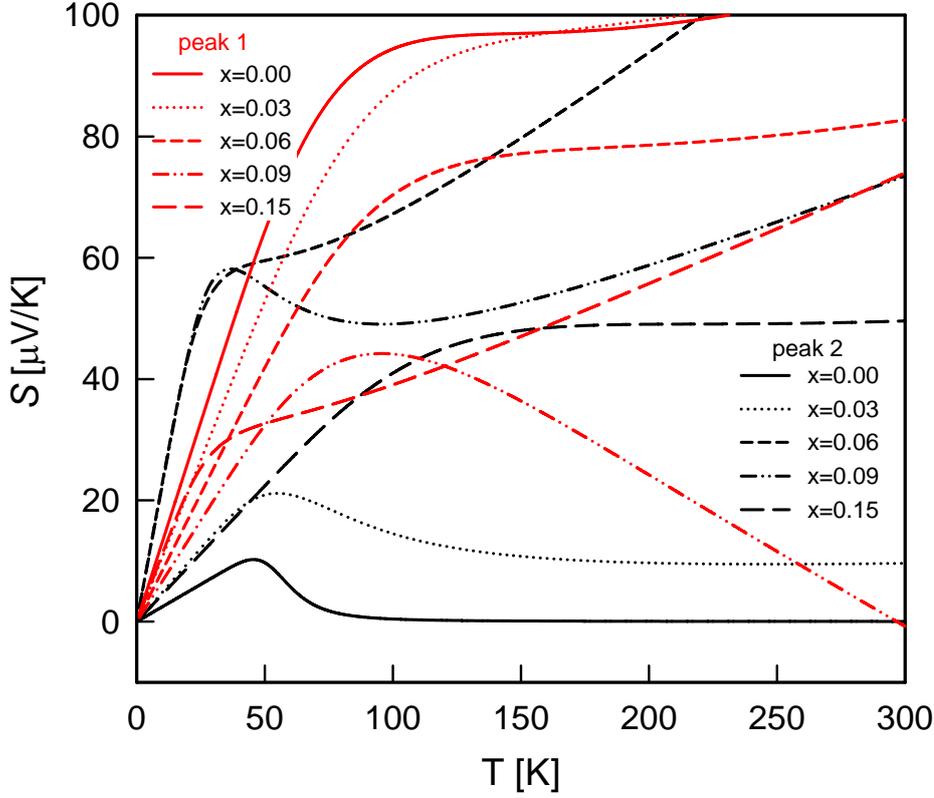


Figure 3.32: The diagrams show the development of the characteristic temperatures T_f and T_0 as well as the scaling parameter c_1 and c_2 the according to the *M.K-model* and the *A.F-model* using single- and double peak fitting .

temperature shoulder observed at CePd₃ may still be present for the other samples. It is not clearly evident from the data, but the shoulder seems to be next to S_{max} creating nearly a double maximum. It looks as if the shoulder shifts to higher temperatures with increasing Rh content up to $x = 0.03$ and then again to lower T for $x = 0.06$ and 0.09 , while the maximum due to Kondo interaction monotonously shifts to higher temperatures with increasing Rh concentration. This would be an interpretation for the widening of the total maximum. First we have interpreted the data according to the simple *A.F-model* and the *M.K-model*, for which the fit curves are depicted in Fig. 3.29. As in the former series the data at lowest temperature are not reproduced and for Rh concentrations of more than 3% the *M.K-model* gives only poor fit-curves. To generate good fit curves the low temperature data had to be skipped before the fit process. In some cases the achieved fit parameters strongly depend on the temperature from which the data were used for fitting, as it is visualized in the left panel of Fig. 3.30. The fit curves in Fig. 3.29

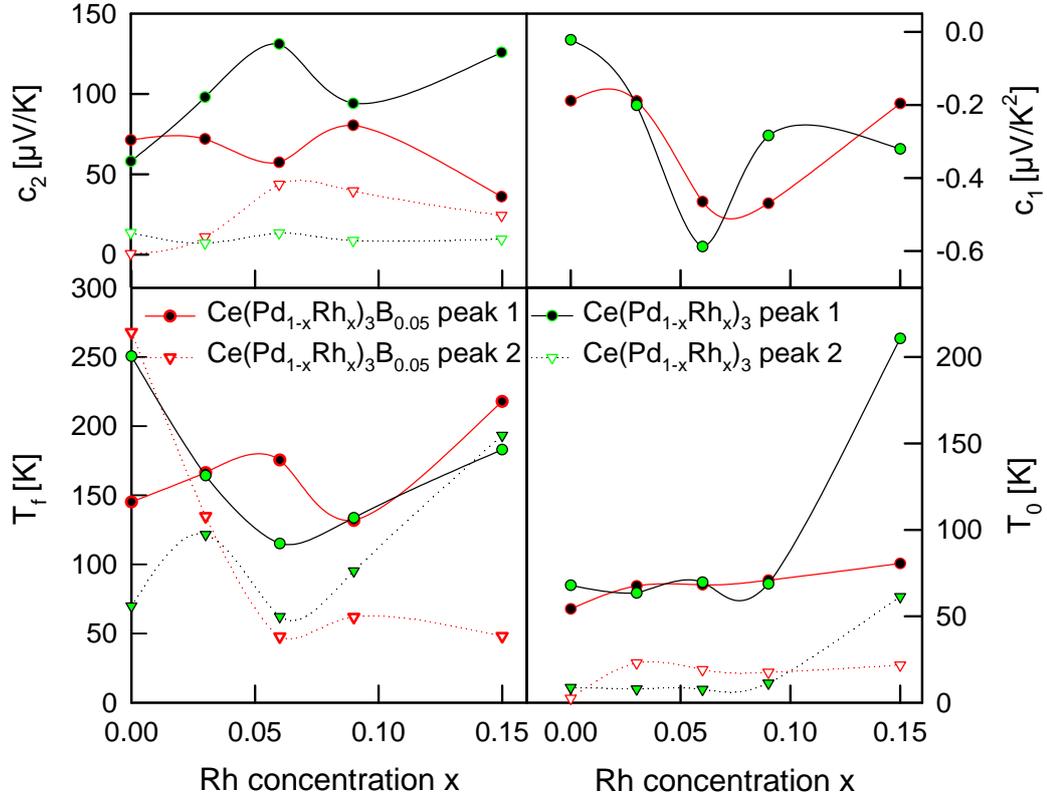


Figure 3.33: The diagrams show the development of the characteristic temperatures T_f and T_0 as well as the scaling parameter c_1 and c_2 the according to the *M.K-model* and the *A.F-model* using single- and double peak fitting .

take into account the whole measured temperature interval and the extracted fit parameter T_0 (pictured in Fig. 3.31 shows the same tendency for both models). T_F decreases for concentrations up to 6% and stays then constant, while T_0 is rather unaffected at low Rh concentrations and increases distinctly for $x = 0.15$. A second fit procedure was started following the description in section 3.3.2. A comparison of the curves for $x = 0.00$ and $x = 0.06$ is denoted in the right panels of Fig. 3.30. One sees that the curvature is reproduced much better by the double peak structure, than by the single *A.F-model*. Of course this is to expected if three more fit-parameter are used, but there seems to be a real physical background. A comparison of the evolution of the fit-parameters according to an increasing Rh content (see Fig. 3.31 evidences that the introduction of a second peak generally decreases the linear term and smoothes its dependence to x . Of course $c_{2,1}$ is also generally smaller, but the tendency with increasing Rh content is comparable to c_2 as it is for T_f and T_0 . The very low values of $c_{2,2}$ at $x = 0$ and 0.03 damp the rather

high $T_{0,2}$ values at this concentrations. Looking at the development of the peaks with enhanced Rh percentage pictured in Fig. 3.32 the assumption made above, that the main maximum (peak 1) is shifted to higher temperatures successively, while peak 2 dominates the low temperature behavior and for Rh concentrations higher than 3% peak 2 also shows higher values than peak 1 at high temperatures. Finally we want to compare the behavior of fit-parameters for the Ce(Pd_{1-x}Rh_x)₃- and Ce(Pd_{1-x}Rh_x)₃B_{0.05}-series for which the obvious difference in the development of the maximum in $S(T)$ is also reflected in the evolution of the characteristic temperatures. For comparison the fit-parameters of both series are plotted in Fig. 3.33 and one sees that the linear coefficient c_1 has a comparable response to an enhancement of Rh. For the Ce(Pd_{1-x}Rh_x)₃-series the ratio between $c_{2,1}$ and $c_{2,2}$ is generally much larger than it is for Ce(Pd_{1-x}Rh_x)₃B_{0.05} that means that for Ce(Pd_{1-x}Rh_x)₃ peak 1 is more dominant than for Ce(Pd_{1-x}Rh_x)₃B_{0.05}. A peculiar feature in the development of the different $T_{f,i}$ with increasing Rh content is that for Ce(Pd_{1-x}Rh_x)₃ the curvature of $T_{f,1}$ vs. x looks similar to the curvature of $T_{f,2}$ vs. x of the Ce(Pd_{1-x}Rh_x)₃B_{0.05}-samples. But the development of $T_{f,2}$ of Ce(Pd_{1-x}Rh_x)₃ has a comparable structure as $T_{f,1}$ vs. x of Ce(Pd_{1-x}Rh_x)₃B_{0.05}. This peculiarity is not originated by the double peak fitting because as described above the $T_{f,1}$ -values strongly correlate to the values of T_f generated by single *A.F-model*. In contrast to that the evolution of $T_{0,i}$ is very similar for both sample series even with respect to the absolute values. $T_{0,1}$ and $T_{0,2}$ are nearly constant and show comparable values for both series with increasing Rh percentage. Only for $x = 0.15$ of the Ce(Pd_{1-x}Rh_x)₃-series both values are enhanced according to the change of its $S(T)$ -behavior.

3.4.3 Thermal conductivity

At low temperatures the thermal conductivity of CePd₃B_{0.05} is somewhat increased by the substitution of Pd by Rh but for $T > 150$ K all $\lambda_{tot}(T)$ -curves for $0.06 \leq x < 0.15$ fall together. The analysis according to *WF-l* shows, that the decreasing electrical resistivity and therefore increasing $\lambda_e(T)$ compensates the reduction of $\lambda_{ph}(T)$. Only Ce(Pd_{0.97}Rh_{0.03})₃B_{0.05} exhibits a smaller λ_{tot} at high temperatures due to the increased $\rho(T)$. The sample with $x = 0.15$ shows an enhanced $\lambda_{tot}(T)$ due to the high electronic contribution and an increased peak in λ_{ph} . In Fig. 3.35 a comparison of the $\lambda_{ph}(T)$ -curves, according to *WF-l*, of the Ce(Pd_{1-x}Rh_x)₃- and the Ce(Pd_{1-x}Rh_x)₃B_{0.05}-series below 150 K is given. At $x = 0$ the low temperature peak in $\lambda_{ph}(T)$ of the B doped material is more than halved. But with Pd/Rh substitution λ_{max} for Ce(Pd_{1-x}Rh_x)₃ is decreased monotonically up to $x = 0.09$, while for Ce(Pd_{1-x}Rh_x)₃B_{0.05} the peak increases by about 50% with $x = 0.03$ and then is downsized again. At $x = 0.09$ λ_{max} of Ce(Pd_{1-x}Rh_x)₃ is less than

40% higher than that of Ce(Pd_{1-x}Rh_x)₃B_{0.05}. At temperatures around 150 K the differences are even smaller. In Fig. 3.36 the fit-parameters according to *WF-l* are plotted for both sample sets. The parameters were normalized to the values at $x = 0$ and show the development of the phonon scattering mechanisms with increasing Rh content. It has to be kept in mind that the doping with B enhances the point defect scattering of pure CePd₃ about a factor eight, decreases the boundary scattering and the scattering due to umklapp processes and keeps the electron-phonon contribution constant (see Fig. 3.13). From the evolution of the scattering parameters and the Debye temperature one can see that the increase of $\lambda_{ph,max}$ due to the Rh substitution of 3% is a result of decreased point defect scattering accompanied by reduced boundary and electron-phonon scattering. While the first and second of these scattering contributions generally scale down with enhanced Rh content, the point defect scattering is successively enhanced with increasing Rh content up

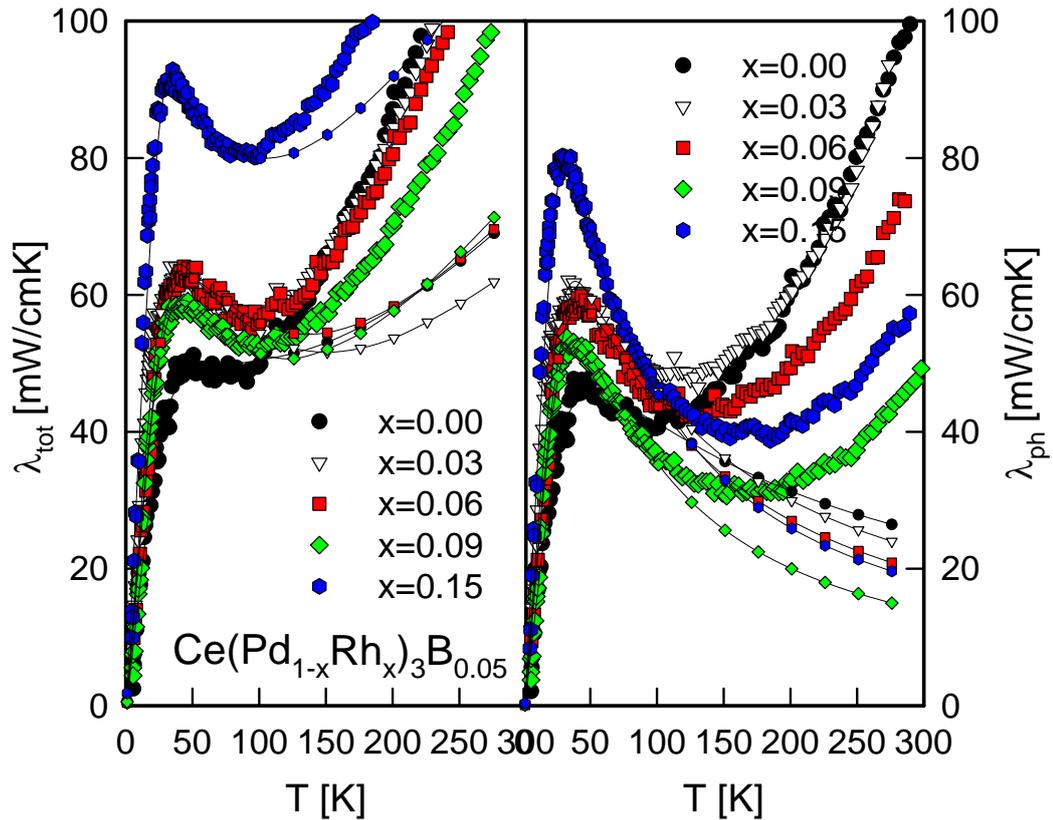


Figure 3.34: The left diagram shows the measured $\lambda(T)$ -behavior with additionally solid lines denoting radiation loss corrected $\lambda_{tot}(T)$ curves. By applying the *WF-l* and the Callaway model the $\lambda_{ph}(T)$ -curves of the left panel were generated, here solid lines also present radiation corrected data.

to 9% and the electron phonon term shows a drastic enhancement of a factor of five for $x = 0.06$ and 0.09 and is finally decreased to a value of about 1.5 times the starting point. For θ_D the fit algorithm shows the tendency to run to unphysical low values (about 150 K) so we limited the minimum to 200 K). This minimum value was reached for all samples except for $x = 0.03$, where a stable value of 226 K was found. This increased value may be a reason for the break down of the fit-parameter of the electron phonon interaction.

3.4.4 Figure of merit

Finally the figure of merit was calculated according to Eqn. 1.77 using the measured transport data. For $\lambda(T)$ the radiation loss corrected data were employed also. The results are plotted in the left panel of Fig. 3.37, which in the right diagram shows results for Ce(Pd_{1-x}Rh_x)₃ for comparison. In

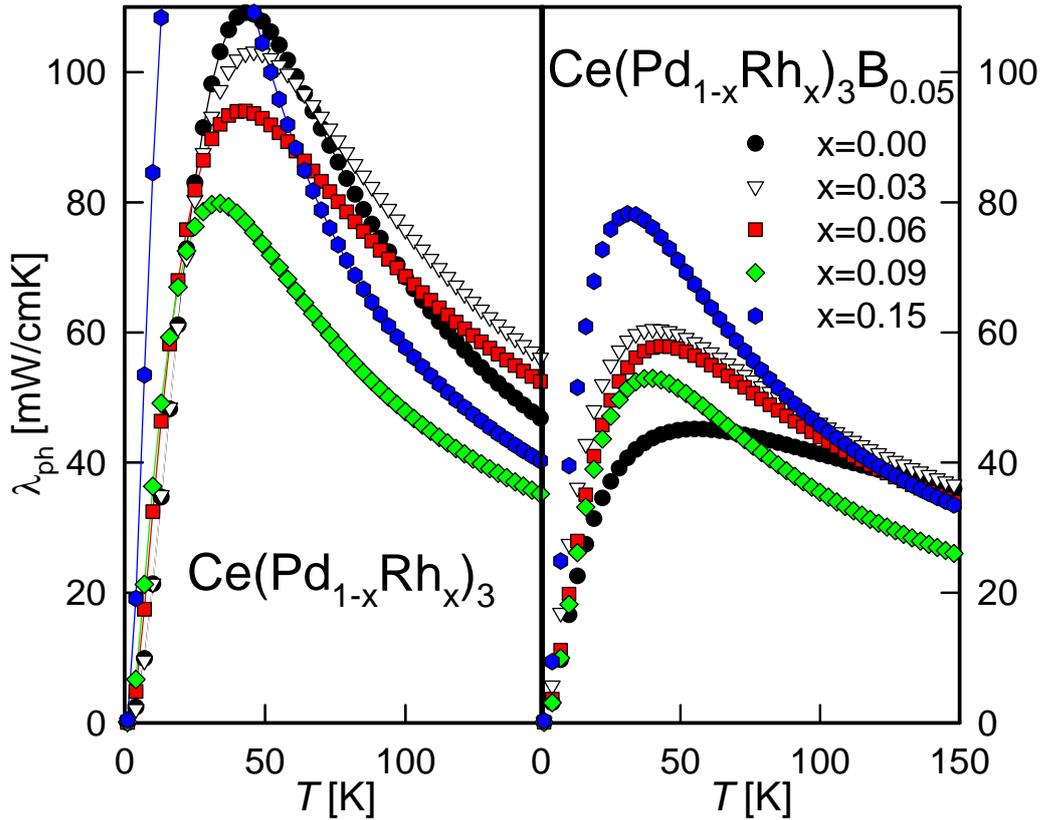


Figure 3.35: The left and right diagram contrast the $\lambda_{ph}(T)$ -curves (according to $WF-l$) of the Ce(Pd_{1-x}Rh_x)₃- and the Ce(Pd_{1-x}Rh_x)₃B_{0.05}-series, respectively.

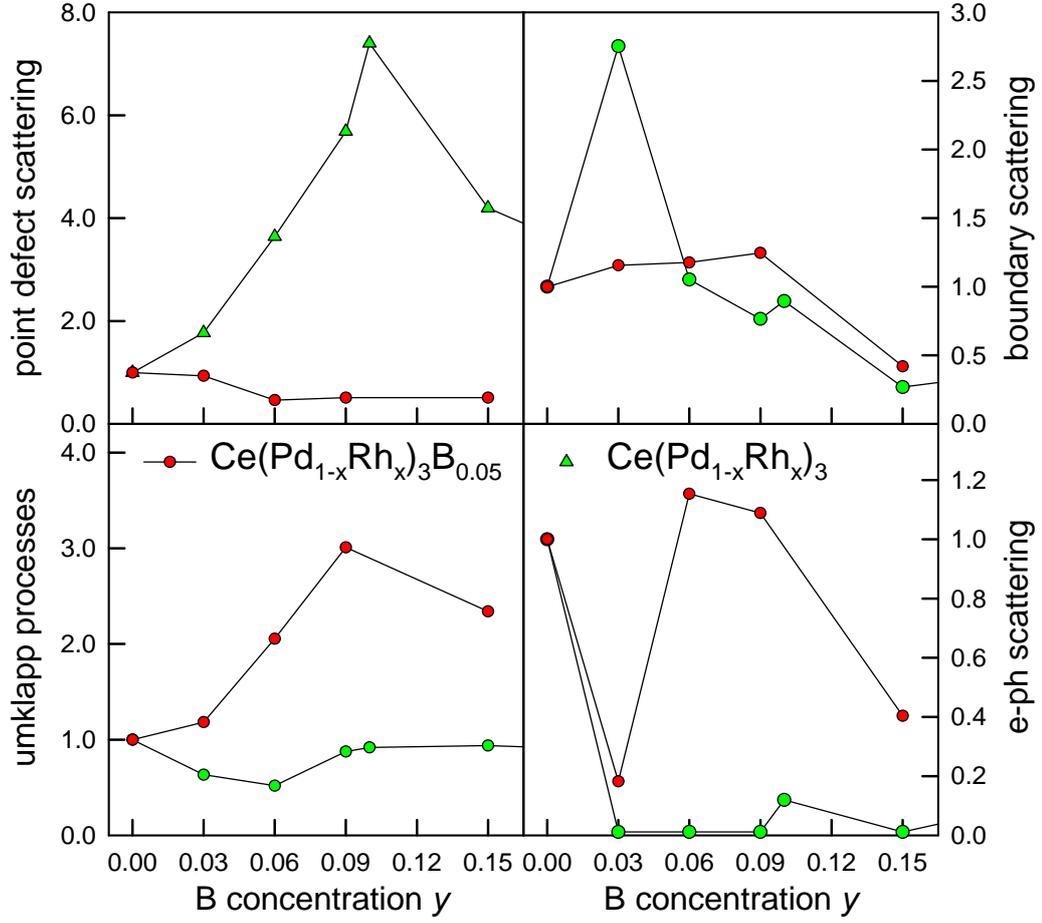


Figure 3.36: Clockwise, the diagrams show the development of the fit-parameters in terms of the $WF-l$ according to point defect, boundary and electron phonon scattering and umklapp processes. The red curves are the behavior of $\text{Ce}(\text{Pd}_{1-x}\text{Rh}_x)_3\text{B}_{0.05}$ and the green plots are related to $\text{Ce}(\text{Pd}_{1-x}\text{Rh}_x)_3$. The solid lines are a guide to the eyes.

both series ZT is positively affected by small substitutions of Pd by Rh. For $x \leq 0.09$ the figure of merit is enhanced continuously, followed by a decrease for $x = 0.15$. It seems that for $\text{Ce}(\text{Pd}_{1-x}\text{Rh}_x)_3$ the maximum ZT is reached in the range of 9% Rh, but for $\text{Ce}(\text{Pd}_{1-x}\text{Rh}_x)_3\text{B}_{0.05}$ the value at $x = 0.15$ is still very high so we assume that the maximum will be between $x = 0.09$ and 0.15, but looking at the single components of ZT this maximum will not outbalance the value for $\text{Ce}(\text{Pd}_{1-x}\text{Rh}_x)_3$ by far, if at all. The improvement of ZT with increasing Rh content in $\text{Ce}(\text{Pd}_{1-x}\text{Rh}_x)_3\text{B}_{0.05}$ is mainly due to the enhanced thermopower, because for $x = 0.03$ $\lambda(T)$ and $\rho(T)$ are even sized up. Contrary to that in $\text{Ce}(\text{Pd}_{1-x}\text{Rh}_x)_3$ the thermopower is decreased for $x > 0.03$ but still

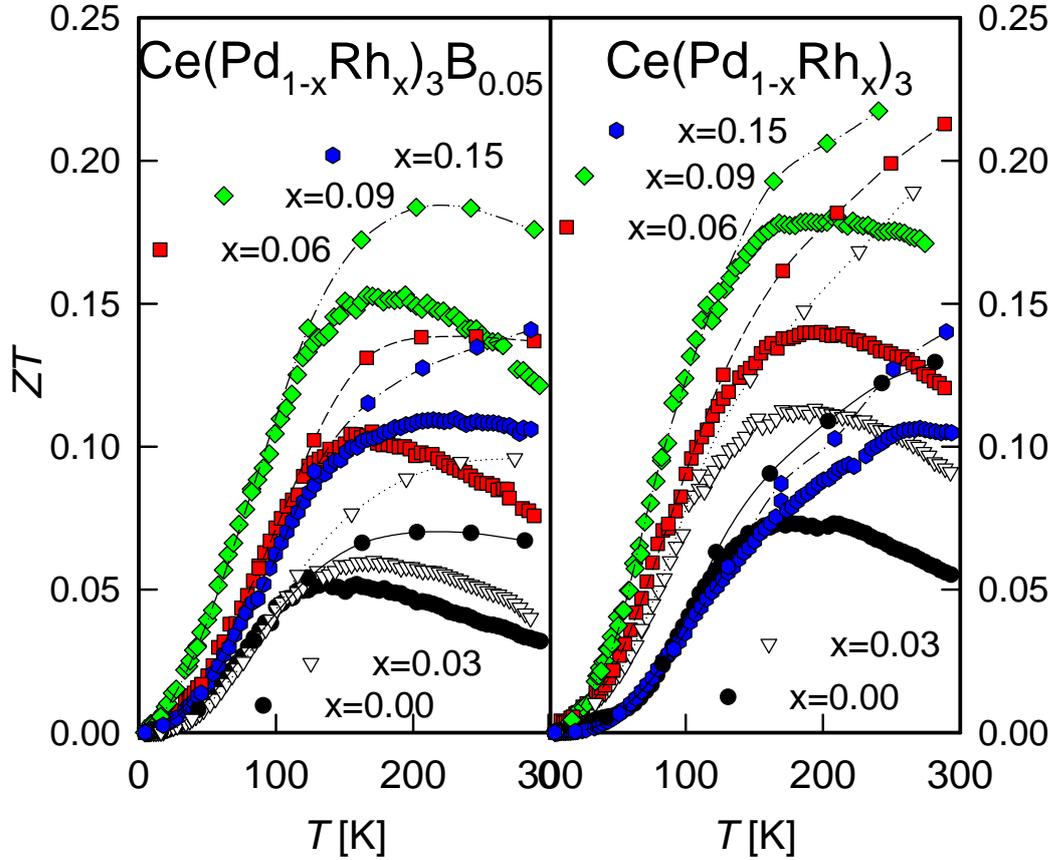


Figure 3.37: The two figures display the dependence of ZT on the Rh concentration in $\text{Ce}(\text{Pd}_{1-x}\text{Rh}_x)_3\text{B}_{0.05}$ and $\text{Ce}(\text{Pd}_{1-x}\text{Rh}_x)_3$. The lines with sporadic marks represent curves on the basis of radiation loss corrected $\lambda(T)$, while the dense data lines denote values due to pure measured data.

ZT exhibits growing values particularly due to the steady diminishing of $\rho(T)$. The changes of $\lambda(T)$ in dependence of the Rh concentration have only minor effects on ZT for $x \leq 0.09$ in both series. For $x = 0.15$ the extinct boost in $\lambda(T)$ accompanied by the diminished $S(T)$ is responsibly for the draw back of the figure of merit. It has to be concluded that B doping with simultaneous Rh substitution on CePd₃ shows no improvement of the thermoelectric figure of merit compared to pure Rh substitution.

3.5 $\text{Ce}(\text{Pd}_{0.94-x}\text{Rh}_x\text{Ag}_{0.06})_3$

As Ag has one electron more than Pd the substitution of Pd by Ag shifts the Ce valency toward 3+ [6]. Based on the same idea as for the

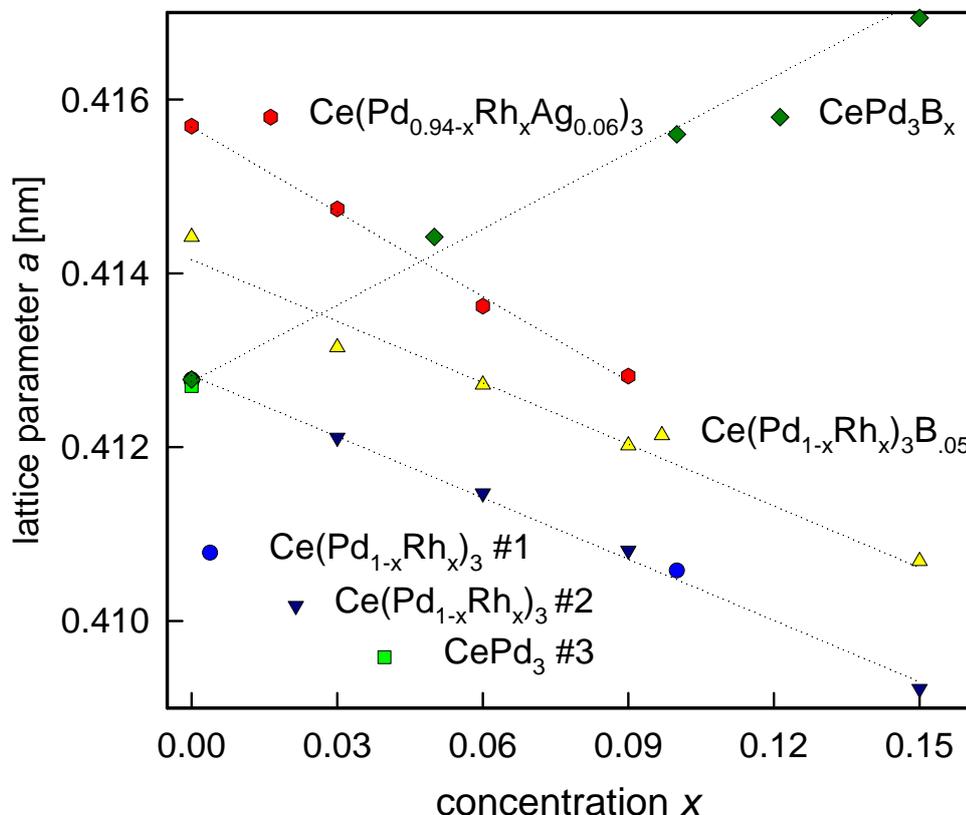


Figure 3.38: This diagram shows the evolution of the lattice-parameter of the various sample sets with increasing substitution or doping.

Ce(Pd_{1-x}Rh_x)₃B_{0.05}-series it should be tested, if the simultaneous introduction of Ag and Rh can improve the thermoelectric performance. In literature [11] a maximum solubility of about 40% has been found and it is assumed that the integer valence 3+ is reached at 13% Ag substitution [64]. We have synthesized a series of Ce(Pd_{0.94-x}Rh_xAg_{0.06})₃ with x=0, 0.03, 0.06 and 0.09 using newly synthesized CePd₃⁽³⁾ as starting material. In section 3.1 the properties of CePd₃⁽³⁾ were discussed already. From X-ray diffraction no secondary phases were determined. By the substitution of 6% Pd by Ag the lattice parameter is increased about twice that much as due to a doping with 5% B. The introduction of Rh decreases the lattice parameter linearly, but the slope seems to be steeper than for Ce(Pd_{1-x}Rh_x)₃ or Ce(Pd_{1-x}Rh_x)₃B_{0.05} as it can be seen in Fig. 3.38. Thus we can conclude that the lowered Ce valency due to the Ag-introduction is actually increased by the substitution of Pd by Rh.

3.5.1 Electrical resistivity

The temperature dependent curvature of the electrical resistivity due to the substitution of Pd by Ag is comparable to the behavior of B doped CePd₃. The broad maximum in $\rho(T)$ at about 110 K is shifted to a very pronounced maximum at about 14 K reaching $\rho_{max} \approx 530 \mu\Omega cm$. But in contrast to the CePd₃B_y-series the effect is more drastic, which means that ρ_{max} is higher and T_{max}^ρ is lower than for a comparable B concentration, but the curve of Ce(Pd_{0.94}Ag_{0.06})₃ strongly resembles the one of CePd₃B_{0.1}, which also has a similar lattice parameter and therefore probably the same Ce valence. A comparison of the resistivity behavior of the different sample sets is plotted in Fig. 3.39. One can see in the left upper panel that with increasing Rh content in Ce(Pd_{0.94-x}Rh_xAg_{0.06})₃ the maximum is shifted to lower temperatures and we just see its right flank within the measurement range of 4.2 to 300 K. The attempt to fit the curvature of this series using the *A.F-model* failed as it did at the Ce(Pd_{1-x}Rh_x)₃B_{0.05}-series and the decay also does not follow a purely logarithmic law like Eqn. 3.1 and therefore can not be interpreted as simple Kondo system. The room temperature resistivity is steadily decreased with enhanced Rh content in contrast to the Ce(Pd_{1-x}Rh_x)₃B_{0.05} series and the development of the curvature with increasing x shows also large differences between these sample sets.

3.5.2 Thermopower

The thermopower of CePd₃ is reduced significantly due to the insertion of Ag as it has been shown already by Sthioul et al. [11]. The data therein fit very nicely to the measured curves of the samples measured in the scope of this thesis. In contrast to the $\rho(T)$ curves the thermopower data of Ce(Pd_{0.94}Ag_{0.06})₃ are more comparable to the sample with $x = 0.5$ of CePd₃B_y than to the one with 10% B content. An introduction of Rh enhances the thermopower at room temperature, but T_{max}^S and S_{max} are not affected as much as in the sample sets (compare Fig. 3.41, which gives a comparison of the $S(T)$ -curves of all discussed sample-series). As the appearance of the $S(T)$ -curves of Ce(Pd_{0.94-x}Rh_xAg_{0.06})₃, Ce(Pd_{1-x}Rh_x)₃ and Ce(Pd_{1-x}Rh_x)₃B_{0.05} is rather dissimilar, it is astonishing that by using the double peak *A.F-model* one obtains fit parameters which suit the parameters for Ce(Pd_{1-x}Rh_x)₃ and Ce(Pd_{1-x}Rh_x)₃B_{0.05}. In Fig. 3.40 the evolution of the fit-parameter of the three sample series derived by the double peak *A.F-model* are compared. The parameters $T_{0,1}$ and $T_{0,2}$ of the three series are more or less in line with each other and show a linear dependence on x for $x \leq 0.09$. The parameters $c_{2,1}$ and $c_{2,2}$ of Ce(Pd_{0.94-x}Rh_xAg_{0.06})₃ and Ce(Pd_{1-x}Rh_x)₃B_{0.05} behave also very similar. $T_{f,1}$ and $T_{f,2}$ in principle exhibit the same tendency, but the values of the first are generally a little smaller for Ce(Pd_{0.94-x}Rh_xAg_{0.06})₃, while the

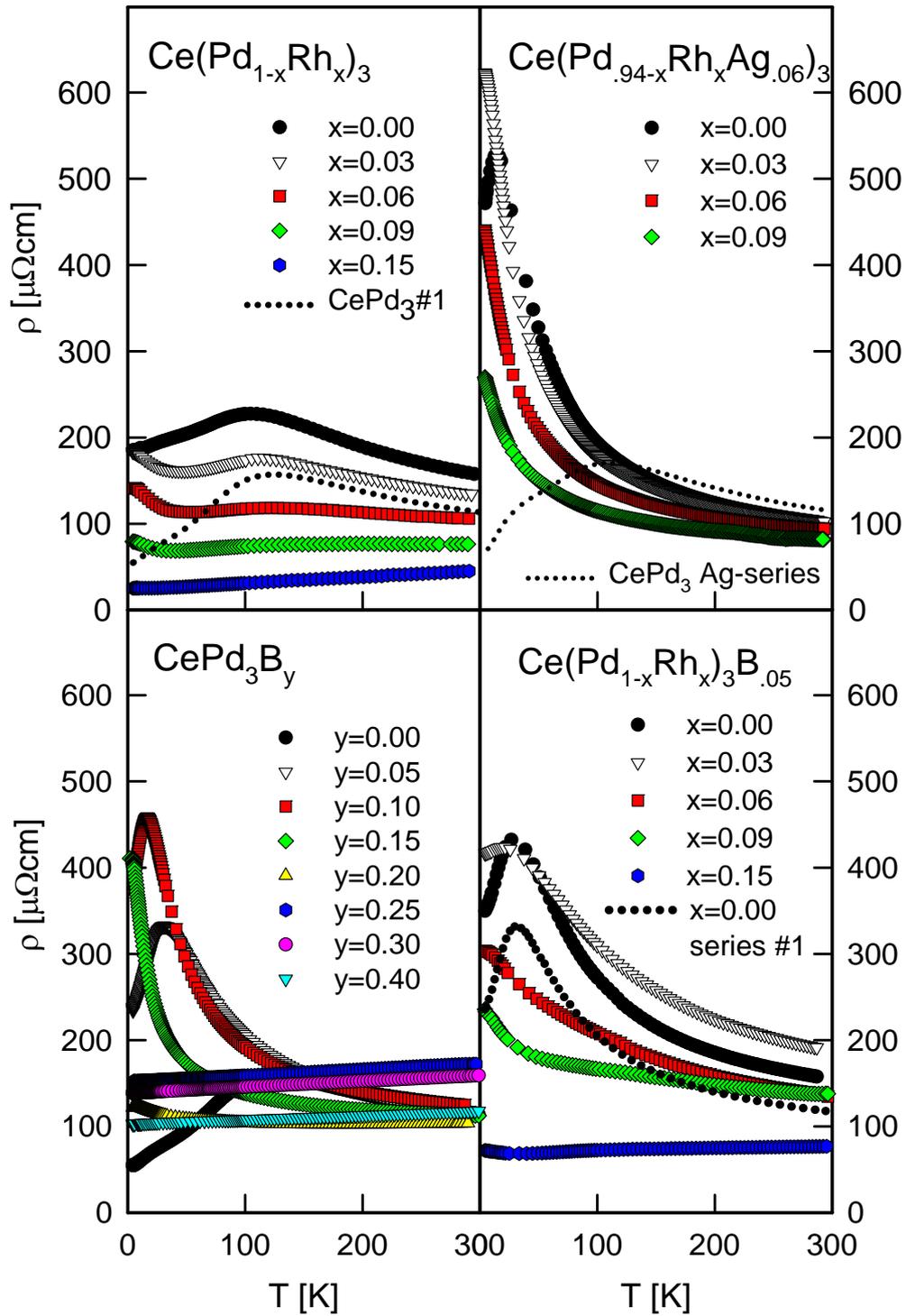


Figure 3.39: The four panels show the temperature dependent resistivity of the discussed sample series.

latter have lower values for $x \leq 0.03$ and enhanced values at higher Rh concentrations. Also misfitting has to be taken into account, because specially on this sample-set the fit-algorithm tended to produce unphysical fits, which didn't even follow the curvature, but due to the consistency of the $T_{0,1}$ - and $T_{0,2}$ -values we think that we have found a reasonable set of values describing the thermopower of the different substitution and doping series.

3.5.3 Thermal conductivity

The low temperature maximum of $\lambda(T)$ of CePd₃ is completely suppressed by the substitution of 5% Pd by Ag, but above 150 K $\lambda_{tot}(T)$ of CePd₃⁽³⁾ even is a little smaller than that of the Ag substituted derivate due to the higher electrical resistivity which decreases $\lambda_e(T)$. The additional substitution of Rh does not change the behavior effectively. $\lambda_{tot}(T)$ is decreased marginally due to a small reduction of $\lambda_{ph}(T)$ which is not completely compensated by the en-

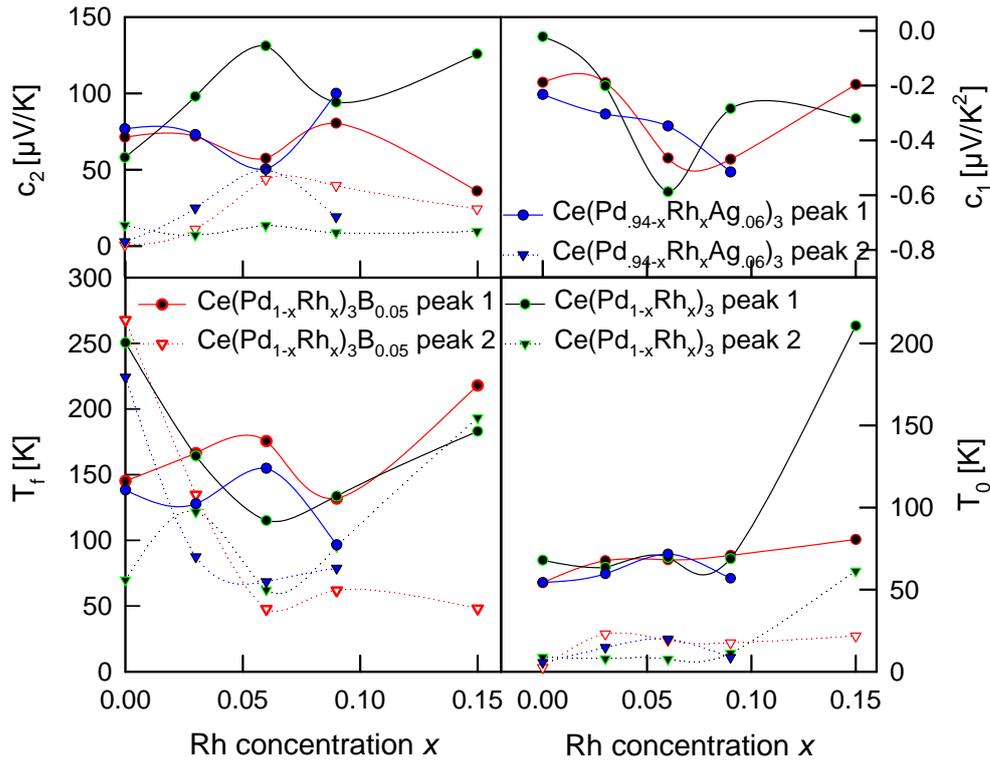


Figure 3.40: The diagrams show the development of characteristic temperatures and scaling parameters of Ce(Pd_{1-x}Rh_x)₃, Ce(Pd_{1-x}Rh_x)₃B_{0.05} and the Ce(Pd_{0.94-x}Rh_xAg_{0.06})₃-samples according to a fit-procedure in the scope of the double peak *A.F-model*.

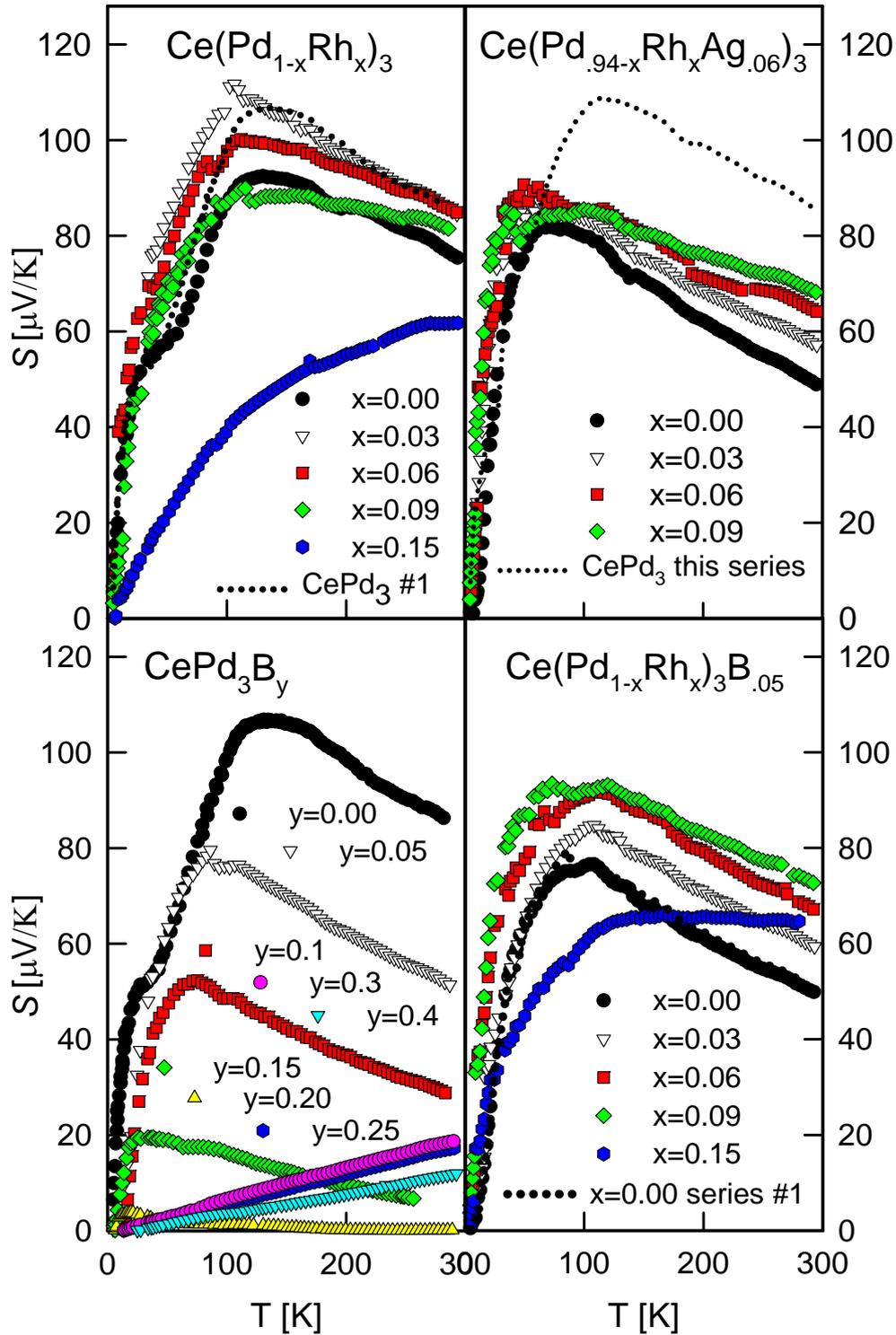


Figure 3.41: The four panels show the temperature dependent thermopower of the discussed sample series.

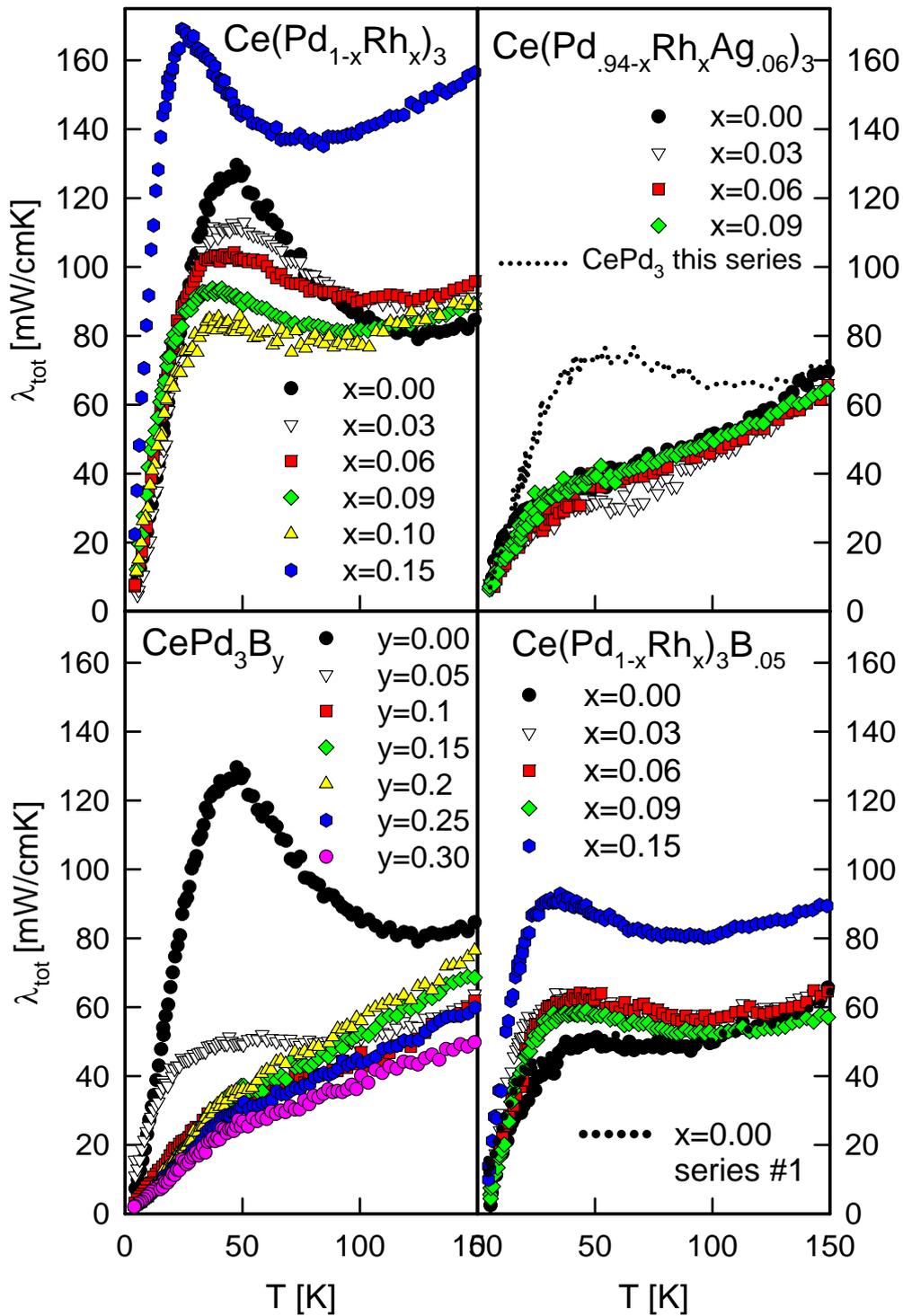


Figure 3.42: The four diagrams plot the measured values of $\lambda_{tot}(T)$ for the discussed sample-sets.

hanced $\lambda_e(T)$. A comparison of the measured $\lambda_{tot}(T)$ -curves for the discussed sample-sets is plotted in Fig. 3.42. It can be seen, that the introduction of 6% Ag has about the same effect as a 10% B doping, but the scattering mechanisms seem to be completely different because the analysis resulted in very disparate scattering parameters as can be seen in Fig. 3.43, which gives a comparison of all evaluated fit-parameters of the four sample series in the scope of the *WF-l* and the Callaway model taking into account the T^3 -law for radiation losses. The single cyan point marks the fit-parameters for $\text{CePd}_3^{(3)}$ so that one can see that the substitution with Ag leads to an reduction of the ph-el scattering, which is exactly the opposite as for B doping. The suppression of the low temperature maximum is mainly due to the sharply enhanced point defect scattering. While boundary scattering and umklapp processes are effectively reduced in $\text{Ce}(\text{Pd}_{0.94}\text{Ag}_{0.06})_3$ the subsequent substitution of Pd by Rh again increases this parameters as it is observed also in the $\text{Ce}(\text{Pd}_{1-x}\text{Rh}_x)_3\text{B}_{0.05}$ -series. Also the ph-el-interaction is increased with enhanced Rh content. The point defect scattering seems to grow further for $x = 0.03$ and then shows a slight reduction for higher Rh contents.

3.5.4 Figure of merit

Finally the figure of merit was calculated and the results are plotted in the upper right diagram of Fig. 3.44, which gives a comparison of the thermoelectric figure of merit of all sample sets. The curves of dense points are calculated by applying Eqn. 1.77 on the pristine measured data, while the dotted lines are corrected with respect to radiation losses. According to the decreased thermopower due to the substitution of Pd by Ag, ZT is diminished over the whole temperature range. At room temperature it is reduced about 70%, taking into account the radiation loss corrected values. The introduction Rh results in an enhancement of ZT and for $x = 0.09$ the measured curve looks alike that of the $\text{CePd}_3^{(3)}$, but the radiation loss correction makes the pure CePd_3 -sample still having the highest thermoelectric figure of merit at room temperature. It can be concluded that the thermoelectric properties can not be improved by this method. The best thermoelectric properties of all samples has $\text{Ce}(\text{Pd}_{0.9}\text{Rh}_{0.1})_3$ of the first sample series, but the achieved performance is far from being useful in technical applications.

3.6 Summary

Lattice-parameter and transport properties of five sample series based on CePd_3 have been measured and the achieved data have been presented and analyzed in the previous chapters. Gambke et al. published several sample sets in Ref. [8] where either Ce was substituted by Y, Sc and La or Pd was

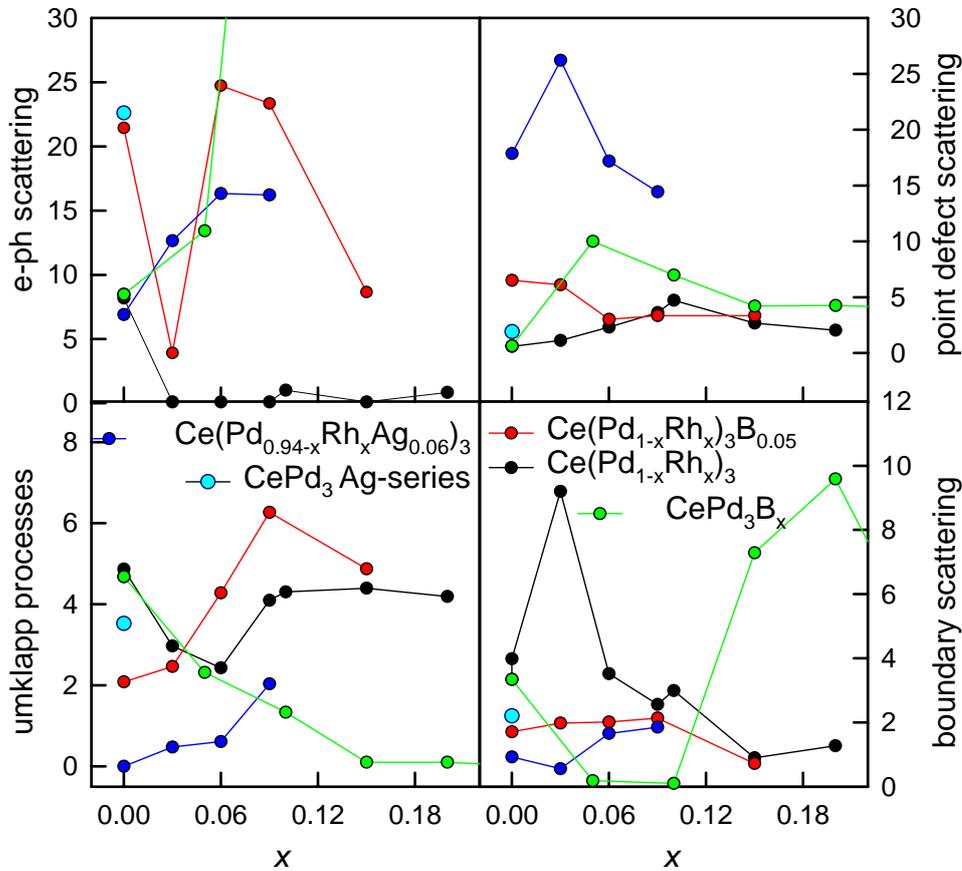


Figure 3.43: The diagrams show the derived scattering parameters according to ph-el, point defect- and boundary scattering as well as to umklapp processes for the four discussed sample sets

exchanged partially by Rh or Ag. They showed that the lattice parameters of these substitution series don't follow Vegard's law, but the dependence of the lattice constant to the grade of substitution is divided into two linear parts. At a critical concentration, which is dependent on the substituent, the slope of the function is changed unsteadily. It has been shown that the regression lines for concentrations larger than the critical one meet in one point at the y-axis. This value can be interpreted as lattice parameter for virtual $Ce^{4+}Pd_3$ in the case of Y, Sc or Rh or $Ce^{3+}Pd_3$ for substituents like Ag. For concentrations below criticality the regression lines join at the lattice constant of CePd₃. Thus it is assumed that the changing of slope is originated by the intermediate valency of the Ce. We have plotted the lattice constants of our samples in the same way as it was done in [8] and additionally included the digitized regression-lines from therein in Fig. 3.45. Furthermore data for

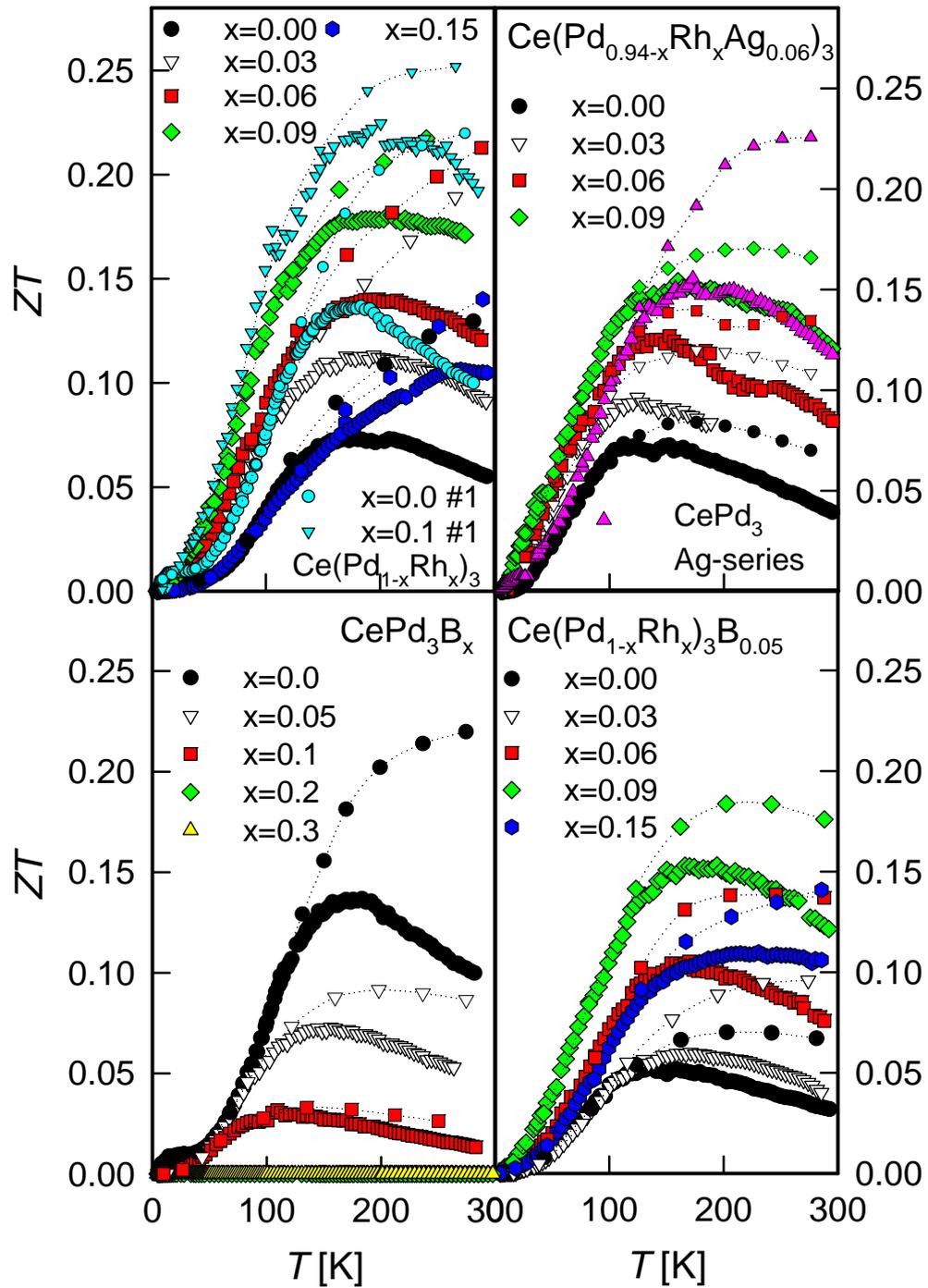


Figure 3.44: The diagrams plot the calculated ZT -curves. The dense data lines represent values which are computed directly from the measured transport properties, while the solid lines with few marks correspond to an assessment taking into account radiation losses contributing to $\lambda(T)$.

CePd₃B_y by Dhar et al. [9] is mapped for comparison. The measured lattice constants are in good agreement with the data from literature. Only the curve of Ce(Pd_{0.94-x}Rh_xAg_{0.06})₃ exhibits a systematic positive offset off the lattice parameter we can not explain yet, but a failure of Ag and Rh weighting can be excluded because of the systematicness of the offset. We can estimate ν_{Ce} by constructing a parallel of the line toward the integer valency through a data point of intermediate valence. The intercept of this straight line lies between the Ce 3+ and 4+ state. We assume a continuous scaling of ν_{Ce} between the virtual integer valency points and thus the respective valency can be assessed. The lattice-parameters and the estimated Ce valency as well

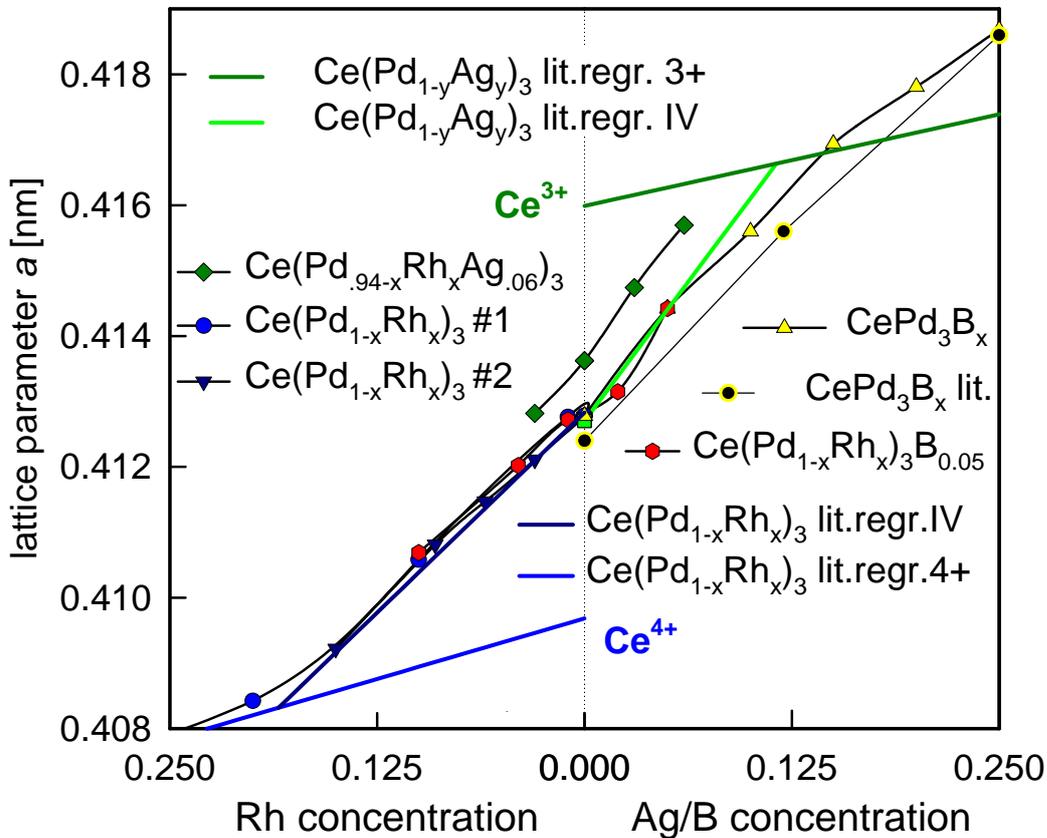


Figure 3.45: This diagram shows the dependence of the lattice-parameter on the grade of substitution or doping with Rh, Ag or B. The solid colored lines are regression curves digitized from [8] pointing out the behavior of Ce(Pd_{1-x}Rh_x)₃ and Ce(Pd_{1-y}Ag_y)₃ assuming saturated integer Ce-valency of 3+ for high concentrations of Ag (dark green) or 4+ for Rh (blue) and for low concentrations of Ag or Rh the Ce has intermediate valence (green or dark blue line).

as the data of the maxima of the temperature difference are listed in table 3.1. Additionally the parameters $T_{0,1}$ and $T_{f,1}$ from the double peak *A-F-model* are reported. We assessed 3.51 as a value for ν_{Ce} for $CePd_3$ which is in good agreement with values from the literature ($\nu_{Ce} = 3.45$ [5], $\nu_{Ce} = 3.5$ [11]). We searched for a relation between the representative values of the sample series by plotting the different parameters in dependence of the lattice constant a (see Fig. 3.47) and tested if the estimated Ce valency serves as a better scaling parameter (see Fig. 3.48). The diagrams reveal some kind of scaling of ρ_{max} and T_{max}^ρ with lattice parameter and Ce valency except the values of the $Ce(Pd_{1-x}Rh_x)_3B_{0.05}$ samples. Generally ρ_{max} is enhanced, while T_{max}^ρ is diminished with increasing a . The thermopower maxima seem also to scale with the lattice parameter. Only the T_{max}^S -values of $Ce(Pd_{0.94-x}Rh_xAg_{0.06})_3$ are not in line, but here the maxima are very broad and the overlap of the discussed double peak structure so that no definite assertion can be made. With increasing lattice parameter T_{max}^S is strongly reduced and the maximal thermopower of $S = 111$ for all samples is reached for $a = 4.121 \text{ \AA}$ at $\approx 108 \text{ K}$.

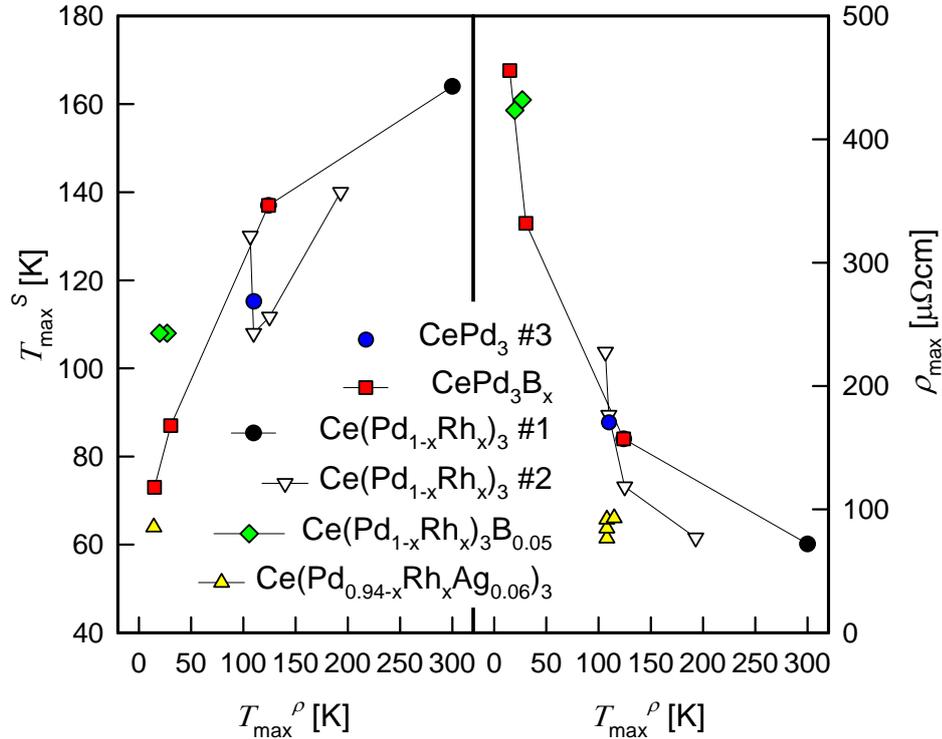


Figure 3.46: The diagrams plot the relation between T_{max}^ρ and ρ_{max} (right panel) and T_{max}^S (left panel) of the different sample series.

Series	$x(y)$	a [Å]	ν_{Ce}	T_{max}^o [K]	ρ_{max} [$\mu\Omega$ cm]	T_{max}^S [K]	S_{max} [μ V/K]	$T_{0,1}$ [K]	$T_{f,1}$ [K]	$T_{max}^{\lambda_{tot}}$ [K]	$\lambda_{tot,max}$ [mW/cmK]
CePd ₃ ⁽¹⁾	0.00	4.1277	3.51	124	157	137	106	65	267	48	130
	0.10	4.1058	3.75	300*	72	165*	94	67	122	40	86
Ce(Pd _{1-x} Rh _x) ₃	0.00	4.1276	3.51	107	228	130	92	68	251		
	0.03	4.1211	3.58	110*	176	108	111	63	164	46	113
Ce(Pd _{1-x} Rh _x) ₃	0.06	4.1147	3.65	125*	118	112	100	70	115	42	104
	0.09	4.1081	3.72	193*	77	140*	88	69	134	38	92
	0.15	4.0922	3.90					211	183	24	169
CePd ₃ ⁽¹⁾	0.00	4.1277	3.51	124	157	137	106			48	130
	0.05	4.1442	3.43	31	332	87	80			56	51
CePd ₃ B _y	0.10	4.1560	3.38	15	456	73	52				
	0.15	4.1694	3.31			37	20				
Ce(Pd _{1-x} Rh _x) ₃ B _{0.05}	0.20	4.1781	3.27			20	4				
	0.00	4.1442	3.60	27	432	108*	77	54	145	50	50
Ce(Pd _{1-x} Rh _x) ₃ B _{0.05}	0.03	4.1315	3.68	20	424	100*	85	68	166	38	64
	0.06	4.1272	3.71			108*	92	68	176	44	64
Ce(Pd _{1-x} Rh _x) ₃ B _{0.05}	0.09	4.1202	3.76			115*	93	71	132	43	59
	0.15	4.1069	3.84					81	218	35	93
CePd ₃ ⁽³⁾	0.00	4.1270	3.51	110	171	115*	109	70	134	54	74
	0.00	4.1570	3.15	14	528	64	82	54	138		
Ce(Pd _{0.94-x} Rh _x Ag _{0.06}) ₃	0.03	4.1474	3.27			63	87	60	128		
	0.06	4.1362	3.40			50	91	72	155		
	0.09	4.1282	3.50			34	85	57	97		

*the maximum is very broad so that the value is rather rough.

Table 3.1: This table lists the measured lattice-parameters, the estimated Ce valency and the values of the maxima in the temperature dependence of $\rho(T)$, $S(T)$ and $\lambda_{tot}(T)$ as well as fit parameters from the double peak-A.F-model. Cells with no content mean that there is no maximum.

The evolution of the maxima in relation to ν_{Ce} does not reveal such a distinct scaling as it can be found with the development with a . On the other hand $T_{tot,max}^\lambda$ seems to scale rather with ν_{Ce} than with a . For a valence smaller than 3.43 no local maximum is build, but $\lambda_{tot}(T)$ steadily increases with temperature. For higher valences the maximum is shifted to lower temperatures. The $\lambda_{tot,max}$ -value neither scales with a nor with ν_{Ce} . The lowest diagrams of Fig. 3.47 and 3.48 map the dependence of $T_{0,1}$ and $T_{f,1}$ on a and ν_{Ce} , respectively, but no scaling can be evidenced.

Further investigations were made to find out if there are any interrelations of the different T_{max}^i or if these temperatures are correlated to their maximum values. For the resistivity maxima, there certainly exist such a scaling as can be seen in the right diagram of Fig. 3.46. With increasing T_{max}^ρ the value for ρ_{max} is decreased. The left panel points out a relation between T_{max}^ρ and T_{max}^S . It shows a proportionality, which was expected because both temperatures should be correlated with T_K . The comparison of other values listed in table 3.1 has not revealed more of such general relations. Specially the λ_{max} -values neither exhibit a relation to the lattice constant nor to the Ce valence. We plotted the fit-parameters presented in Fig. 3.43 versus the lattice parameter and the Ce-valency, to investigate if single scattering mechanisms can be related to a or ν_{Ce} . The results can be found in Fig. 3.49 and 3.50. The data of phonon-electron scattering reveal no evidence for scaling, actually the points are scattered over a large area seemingly without systematic. The plots of point defect scattering show data points, which are also unaffected by the different x-coordinates. Due to the enhanced values of the Ce(Pd_{0.94-x}Rh_xAg_{0.06})₃-series the antithetic development of the single series is not apparent. The boundary scattering of the CePd₃B_y-series has high variability and the peak of the Ce(Pd_{1-x}Rh_x)₃-data is maybe oversized. The rest of the boundary scattering data fits more or less together, but neither a nor ν_{Ce} seem to be a scaling parameter. However the umklapp processes show a distinct dependence on the lattice parameter; they are generally diminished with increasing a , but the curves of each series are somehow separated. By plotting the same values versus ν_{Ce} the curves coincide and reveal that the umklapp processes are enhanced with increasing Ce-valence and build a local peak for pure CePd₃. For the sample of Ce(Pd_{1-x}Rh_x)₃B_{0.05} with $x = 0.09$ and a $\nu_{Ce} \approx 3.76$ a second peak is build then the data-lines join and build a plateau as $\nu_{Ce} \rightarrow 4$. From this examinations we can say, that the Ce-valency is a driving parameter for some important mechanism affecting electrical resistivity, thermal conductivity and thermopower of the CePd₃-derivatives. Still there have to be other scaling parameters to explain the whole variety of physical effects in this material system.

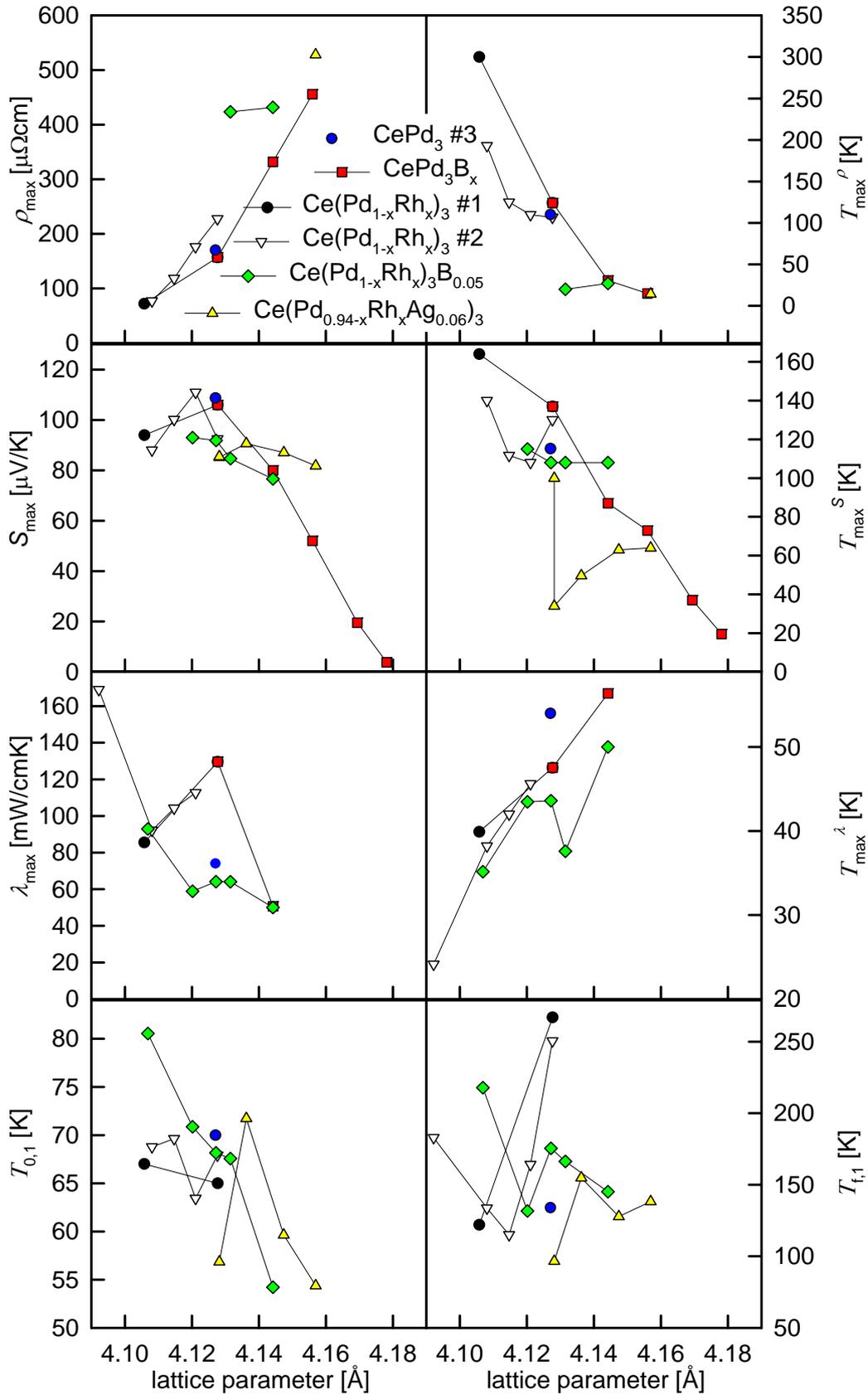


Figure 3.47: The diagrams visualize the relation between the parameters presented in table 3.1 and the lattice constants of the different sample series.

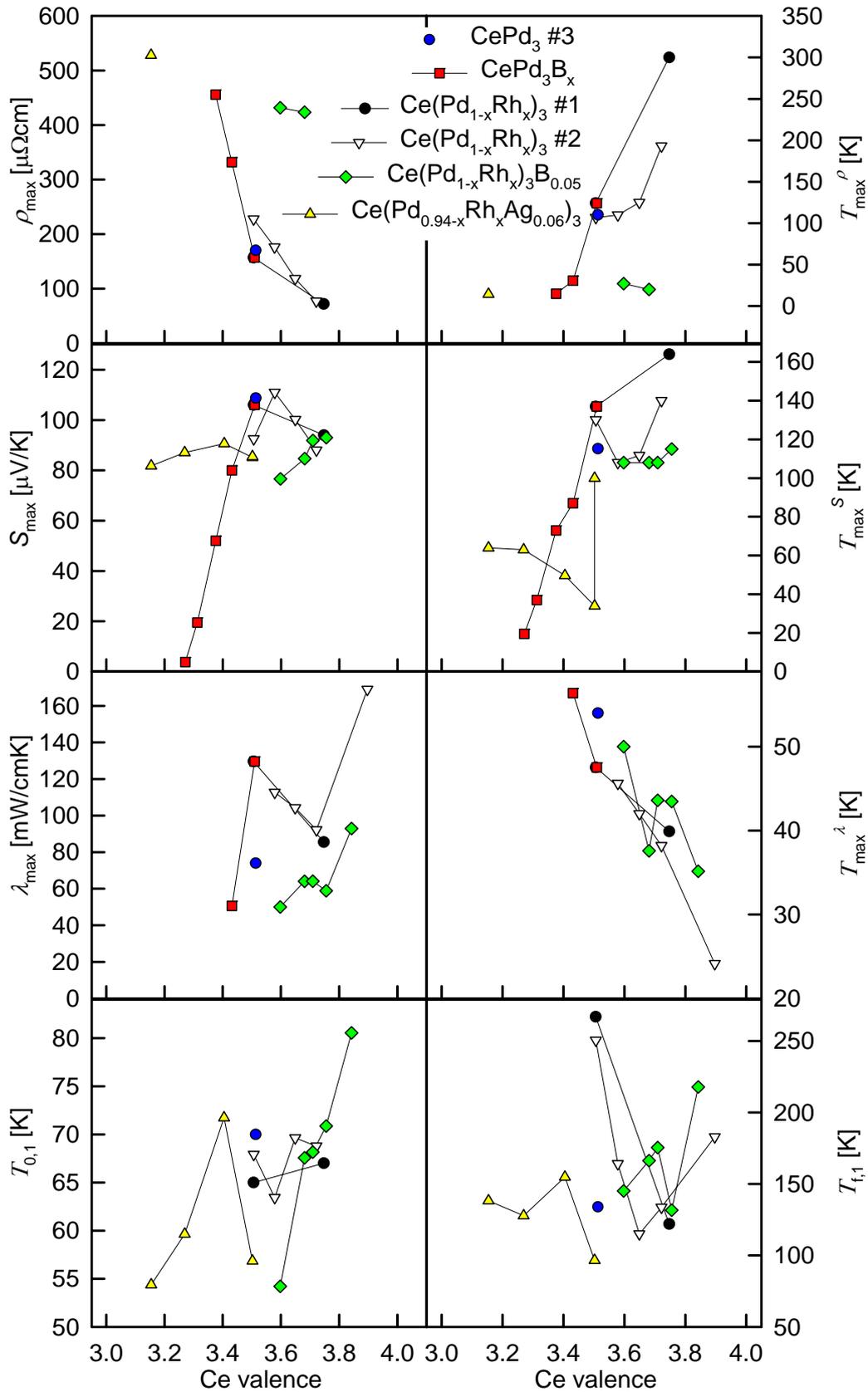


Figure 3.48: The diagrams visualize the relation between the parameters presented in table 3.1 and the estimated Ce valency of the different sample series.

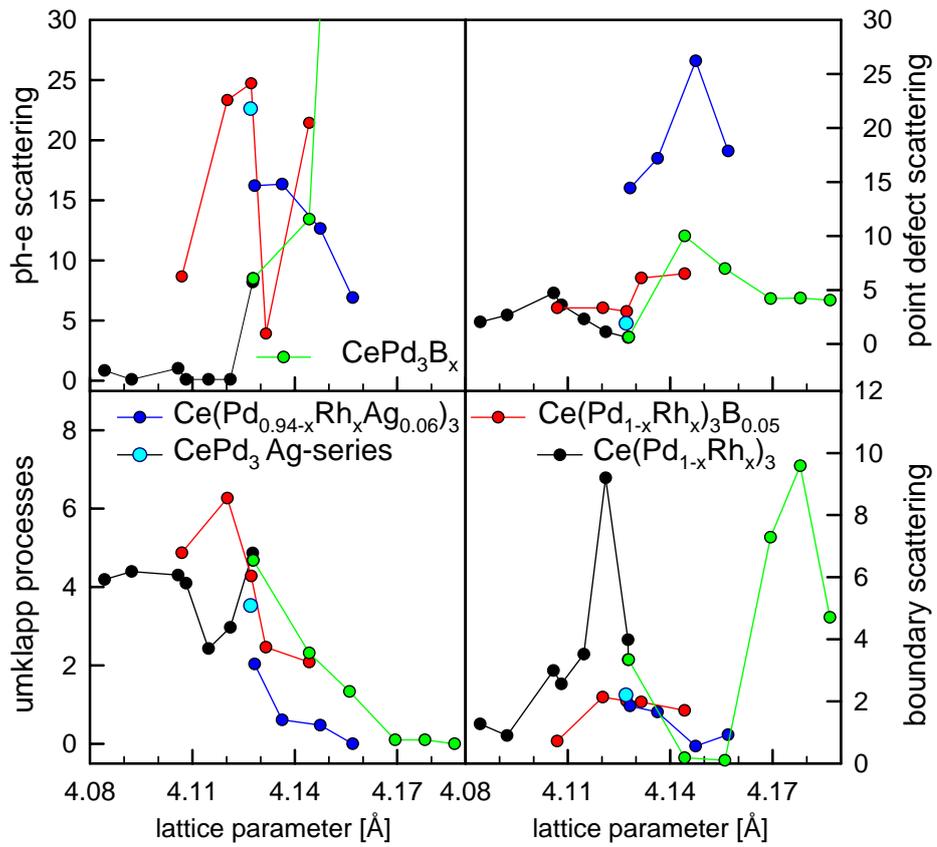


Figure 3.49: The diagrams plot the relation between the scattering parameters according to the $\lambda_{ph}(T)$ -fit curves assessed by $WF-l$ and the lattice parameter a .

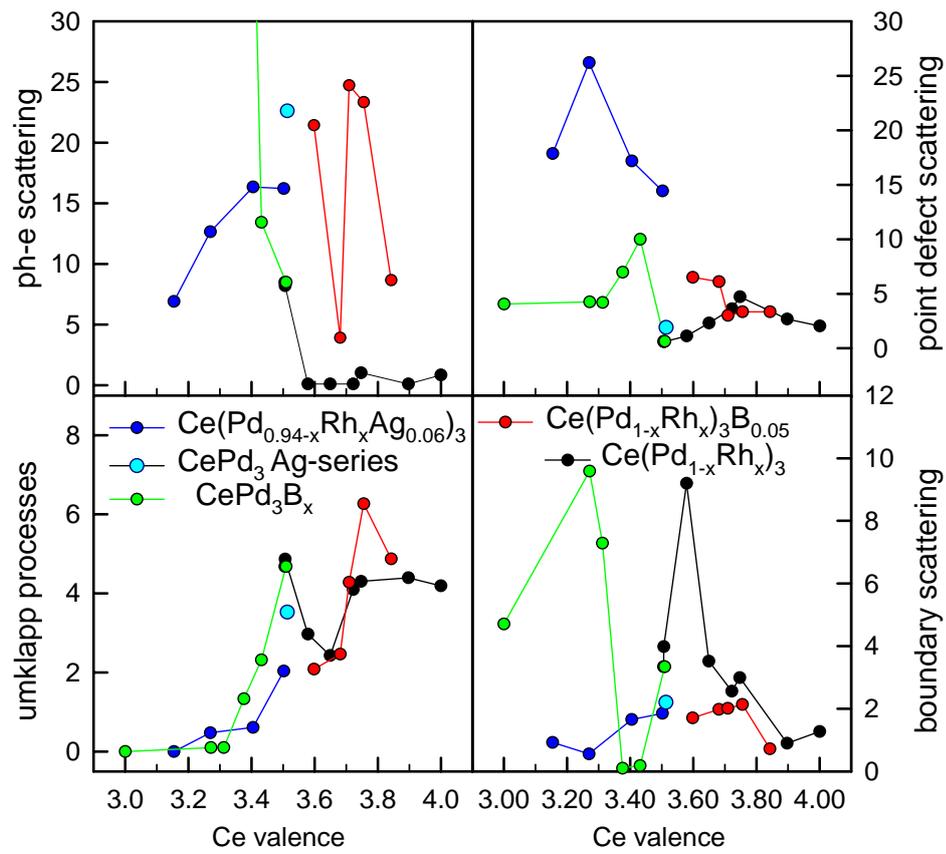


Figure 3.50: The diagrams plot the relation between the scattering parameters according to the $\lambda_{ph}(T)$ -fit curves assessed by $WF-l$ and ν_{Ce} .

Conclusion

The aim of this thesis was to investigate the effect of substitution and doping on the thermoelectric properties of CePd_3 . Five sample series with Ag and Rh as a substitute for Pd and B as dopant were prepared, namely CePd_3B_y , $\text{Ce}(\text{Pd}_{1-x}\text{Rh}_x)_3$, $\text{Ce}(\text{Pd}_{1-x}\text{Rh}_x)_3\text{B}_{0.05}$ and $\text{Ce}(\text{Pd}_{0.94-x}\text{Rh}_x\text{Ag}_{0.06})_3$. Using X-ray diffraction the phase purity of the composites were checked and the lattice parameters were evaluated. The thermoelectric properties were measured and analyzed in the scope of theoretical and empirical models. Finally the thermoelectric figure of merit has been calculated. The X-ray diffraction patterns do not reveal any secondary phases and the achieved lattice parameters are in good agreement to data in literature. However the transport properties of three different CePd_3 -productions show large deviations, because the electronic structure of CePd_3 is very sensitive to smallest changes in the stoichiometry. From the lattice constants we estimated a Ce-valency $\nu_{\text{Ce}} \approx 3.51$ which is in good agreement with literature. While a substitution of 20% of Pd by Rh tunes $\nu_{\text{Ce}} \rightarrow 4$, 13% of Ag shift Ce toward its 3+ state. The doping with B also results in a 3+ state for more than 20% of filled elementary cells. The shift of the intermediate valence state has enormous consequences on all transport properties. In literature resistivity and thermopower data for the first two series already exist and our data are in good agreement. By the introduction of B or Ag the Kondo temperature is generally shifted downward because $\nu_{\text{Ce}} \rightarrow 3$ and as a consequence T_{max}^ρ decreases while ρ_{max} is enhanced. Above the critical B concentration of about 25% the physics changes completely. The $S(T)$ -values are effectively decreased over the whole temperature range and additionally T_{max}^S is steadily reduced. However, the substitution with Rh causes an increase of T_K , due to the shift of $\nu_{\text{Ce}} \rightarrow 4$. Hence T_{max}^ρ is enhanced, accompanied by a reduction of ρ_{max} . T_{max}^S should be also increased, but due to an overlap with a second maximum at lower temperatures the average T_{max}^S sometimes is even reduced with increasing ν_{Ce} . The S_{max} -value of $\text{Ce}(\text{Pd}_{1-x}\text{Rh}_x)_3$ was increased by a substitution of 3% and decreased for higher Rh concentration. In the $\text{Ce}(\text{Pd}_{1-x}\text{Rh}_x)_3\text{B}_{0.05}$ -series S_{max} is steadily enhanced with increasing x . However, the S_{max} of $\text{Ce}(\text{Pd}_{0.94-x}\text{Rh}_x\text{Ag}_{0.06})_3$ increases up to $x = 0.06$ and sinks for higher Rh concentrations.

It was demonstrated that the measured thermal conductivity data can

be separated into its phonon and electronic contributions by applying Wiedemann-Franz law or Wilson's formula. While the first procedure has to be favored, the second still achieves reasonable results and can be used if no electrical resistivity data are at hand. The obtained $\lambda_{ph}(T)$ -curves were analyzed according to Callaway's model using common fit functions for the relaxation times of umklapp-processes, point defect scattering, boundary scattering and phonon electron scattering. While the latter two determine the behavior of $\lambda_{ph}(T)$ at lowest temperatures the first noted scatter mechanism dominates the high temperature region. The maximum value is mainly affected by the point defects. The umklapp processes are the only component of the lattice thermal conductivity which seem to be governed by the valence change. On the contrary phonon-electron scattering seems to be of minor importance in these series of compounds. The thermoelectric figure of merit has been calculated from the measured transport coefficients. The largest enhancement of ZT was found for $\text{Ce}(\text{Pd}_{0.91}\text{Rh}_{0.09})_3$ to be about 70% compared with pure CePd_3 of the second $\text{Ce}(\text{Pd}_{1-x}\text{Rh}_x)_3$ -series. However sample $\text{Ce}(\text{Pd}_{0.9}\text{Rh}_{0.1})_3$ of the first sample set exhibits the highest $ZT(\approx 0.23)$ at room temperature. It has about 15% better performance than the corresponding CePd_3 -material, nevertheless it is far from industrial applicability.

Appendix A

Fitting procedure

Within the scope of this thesis the experimentally obtained transport data were interpreted using theoretical and empirical formulae as fit functions. In this section a summary of the used formulas is given. Generally the fitting was executed using *TableCurve 2D v.5.01* within this program so called *user defined functions (*.udf)* were programmed and the appropriate limits for the fit-parameters were set. The program then searches for the best least square fit within these limits. Of course the uncertainty rises with an increasing count of fit-parameters especially if one parameter cancels the other and a good mathematical fit does not always give a good physical description. Nevertheless some good and physical reasonable results have been gained by this method as it has been shown in the discussion of the experimental data.

A.1 Electrical resistivity $\rho(T)$

The electrical resistivity data $\rho(T)$ (in units of $[\mu\Omega cm]$) were fitted for temperatures $T \gg T_{max}$ by using Eqn. 1.14 and Eqn. 3.1.

$$\rho_{ph} = \frac{c_B G}{\Theta_D} \left(\frac{T}{\Theta_D} \right)^5 \int_0^{\Theta_D/T} \frac{x^5 dz}{(e^x - 1)(1 - e^{-x})} \quad (\text{A.1})$$

$$\rho_f(T \gg T_{max}) = \rho_0 + \rho_{ph} + c * \ln[T] \quad (\text{A.2})$$

The first equation is the theoretical deduced Bloch-Grüneisen formula where $c_B G$ denotes a material dependent constant, Θ_D is the Debye temperature and $x = \frac{\hbar\omega}{k_B T}$. The second equation is an empirical fit formula according to the Kondo impurity model Eqn. 1.32 with a scaling parameter c . Alternatively formula 1.34 was used, which bases on a model by A. Freimuth. Using a temperature dependent effective scattering width $W(T)$ he wrote:

$$W(T) = T_f \exp(-T_f/T) \quad (\text{A.3})$$

$$\rho_f(T) = bJ_{sf}^2 \frac{W(T)}{T_0^2 + W(T)^2} \quad (\text{A.4})$$

This formula can reproduce the maximum of $\rho(T)$ of CePd₃, but not its behavior at lowest temperatures. The parameter b follows from a comparison of the Drude-formula leading to $b = m^*k_b/n e^2 \hbar$ with m^* is the effective mass and n is the charge carrier concentration. J_{sf} is interpreted as hybridization integral taking the overlap of the sd - and the f -wavefunctions into account. $W(T)$ is a temperature dependent effective scattering width $W(T) = T_f \exp(-T_f/T)$ at the fluctuation temperature T_f which is proportional to T_K . The temperature T_0 is interpreted as energy difference between the energy of the "f-band" e_f and the Fermi energy ϵ_f ($k_b T_0 = (e_f - \epsilon_f)$), where $k_b = 1.3807 * 10^{-23}$ J/K is the Boltzmann constant. These formulas were transformed into a *user defined functions* as follows:

User defined function corresponding to Eqn. A.2

#F1=#5/(EXP(-#)+EXP(#)-2)	'integrand ρ_{ph}
#F2=#D/X	' θ_D divided by T
Y=#A+#B*LN(X)+#E*#D*AI(1,0,#F2)/#F2^5	' $\rho(T) = \rho_0 + c * \ln[T] + \rho_{ph}$

User defined function corresponding to Eqn. A.4

#F1=#C*EXP(-#C/X)	' $W(T) = T_f \exp(-T_f/T)$
Y=#A*#F1/(#B^2+#F1^2)	' $\rho_f(T) = bJ_{sf}^2 W(T)/(T_0^2 + W(T)^2)$

A.2 Seebeck coefficient $S(T)$

As described in chapter 1.1.3 two empirical models were found in literature to describe the thermopower of IV compounds. The first formula by M. Koterlyn [42] has only two adjustable parameters T_0 as defined above and N_f , denoting the orbital degeneracy. In this model T_0 has only influence on the position of S_{max} , while N_f determines the magnitude of it. So we introduced a further scaling parameter k as a multiplication factor, because the orbital degeneracy was fixed to $N_F = 2J + 1 = 6$.

$$S_f(T) = k \frac{2\pi^2 k_b}{3|e|} * \frac{TT_0}{\frac{\pi^2}{3}T^2 + (1 + \frac{\pi^2}{N_f^2})T_0^2}. \quad (\text{A.5})$$

The second formula was presented by A. Freimuth [21] together with Eqn. A.4 for the description of the $\rho(T)$ -behavior.

$$S_f(T) = c_1 * T + c_2 * \frac{TT_0}{T_0^2 + W(T)^2}. \quad (\text{A.6})$$

c_1 and c_2 are material constants and $W(T)$ and T_0 are explained as for the resistivity. In order to fit the double peak structure a formula was introduced (Eqn. 3.3) in which the second term of Equ. A.6 was split and we used two different fluctuation temperatures $T_{f,i}$ and also two different $T_{0,i}$. Thus the used fit formula reads like:

$$W_i(T) = T_{f,i} \exp(-T_{f,i}/T) \quad (\text{A.7})$$

$$S_f(T) = c_1 * T + c_{2,1} * \frac{TT_{0,1}}{T_{0,1}^2 + W_1(T)^2} + c_{2,2} * \frac{TT_{0,2}}{T_{0,2}^2 + W_2(T)^2} \quad (\text{A.8})$$

Here the *user defined functions* for the Seebeck fit procedure are presented:

User defined function corresponding to Eqn. A.5

#F1=#B*10 ⁶ *2*PI ² *...	'scaling factor $k * 10^6 * 2 * \pi^2 * \dots$
...*1.38065E-23/3/1.60217E-19	... * $k_b / (3 * e)$
#F2=PI ² /3	' $\pi^2/3$
#F3=1+PI ² /6 ²	' $1 + \pi^2/N_f = 6$
Y=#F1*X*#A/(#F2*X ² +#F3*#A ²)	' $S_f(T) = \#F1 * T * T_0 / \dots$.../($\#F2 * T^2 + \#F3 * T_0^2$)

User defined function corresponding to Eqn. A.6

#F1=#D*EXP(-#D/X)	' $W(T) = T_f \exp(-T_f/T)$
Y=#A*X+#B*X*#C/(#C ² +#F1 ²)	' $S_f(T) = c_1 * T + c_2 * T * T_0 / (T_0^2 + W(T)^2)$

User defined function corresponding to Eqn. A.8

#F1=#D*EXP(-#D/X)	' $W_1(T) = T_{f,1} \exp(-T_{f,1}/T)$
#F1=#E*EXP(-#E/X)	' $W_2(T) = T_{f,2} \exp(-T_{f,2}/T)$
Y=#A*X+#B*X*#C/(#C ² +#F1 ²)+...	' $S_f(T) = c_1 * T + c_{2,1} * T * T_{0,1} / (T_{0,1}^2 +$...+ $\#F*X*#G / (\#G^2 + \#F^2)$
...+#F*X*#G/(#G ² +#F ²)	$W_1(T)^2) + c_{2,2} * T * T_{0,2} / (T_{0,2}^2 + W_2(T)^2)$

A.3 Thermal conductivity $\lambda(T)$

The fitting of thermal conductivity data is a very elaborate procedure. The applied theories were introduced in the theoretical section 1.1.2 where the Wiedemann-Franz law (*WF-l*, Eqn. 1.37) and Wilson's equation (*W-Eqn*, 1.39) are presented to split the total thermal conductivity λ_{tot} into an electron contribution λ_e and a phonon contribution λ_{ph} . It is assumed that $\lambda_{tot} = \lambda_e + \lambda_{ph}$. Following *WF-l* one has to calculate $\lambda_e(T)$ according to

$$\lambda_e = L_0 \sigma T. \quad (\text{A.9})$$

with $L_0 = \frac{\pi^2}{3} \left(\frac{k_B}{e}\right)^2 = 2.45 \times 10^{-8}$ and then subtract the $\lambda_e(T)$ -values from the $\lambda_{tot}(T)$ -values. As one has different temperature scaling normally, spline

values of $\lambda_e(T)$ according to temperature values of $\lambda_{tot}(T)$ have to be generated, which can be subtracted consequently. The obtained $\lambda_{ph}(T)$ -curves were analyzed in terms of the formula according to a relaxation time approach proposed by J. Callaway [23] (Eqn. 1.45).

$$\lambda_{ph} = \frac{k_B}{2\pi^2\nu_s} \left(\frac{k_B T}{\hbar} \right)^3 \left[\int_0^{\Theta_D/T} \tau_c \frac{x^4 e^x}{(e^x - 1)^2} dx \right] \quad (\text{A.10})$$

Because we neglect normal three-phonon interactions, the term I_1/I_2 of Eqn. 1.45 is dropped. The sound velocity ν_s is substituted by its equivalent according to Debye theory (Eqn. 1.47) and τ_c^{-1} is expressed according to Matthiessen's rule (Eqn. 1.8)

$$\nu_s = \omega_D \left(6\pi^2 \frac{N}{V} \right)^{-\frac{1}{3}} \quad (\text{A.11})$$

$$\tau_c^{-1} = \tau_U^{-1} + \tau_D^{-1} + \tau_B^{-1} + \tau_{el-ph}^{-1} + \tau_{rattle}^{-1} \quad (\text{A.12})$$

τ_D , τ_B , τ_U , τ_{el-ph} and τ_{rattle} denote point defect scattering, boundary scattering, Umklapp processes, scattering of phonons by electrons and scattering by loose bound atoms, respectively. The explicit expressions of the inverse relaxation times are given by:

$$\tau_U^{-1} = AT^3 x^2 e^{-\frac{\theta_D}{3T}} \quad (\text{A.13})$$

$$\tau_D^{-1} = Dx^4 T^4 \quad (\text{A.14})$$

$$\tau_B^{-1} = B \quad (\text{A.15})$$

$$\tau_{el-ph}^{-1} = CTx \quad (\text{A.16})$$

$$\tau_{rattle}^{-1} = Ef(x, T)g(x, T) \quad (\text{A.17})$$

using

$$f(x, T) = \frac{\left(\frac{k_B \theta_E}{\hbar} \right)^2 \left(1 - \frac{Tx}{\theta_E} \right)^2 e^{\left(\frac{\theta_E}{T} - x \right)} (e^{x-1})}{\left(e^{\frac{\theta_E}{T}} - 1 \right) \left[e^{\left(\frac{\theta_E}{T} - x \right)} - 1 \right]} \quad (\text{A.18})$$

$$g(x, T) = \left(1 + \frac{4\alpha\nu_s\hbar}{k_B\theta_E} \right) \ln \left[1 + \frac{\frac{Tx}{\theta_E} \left(1 - \frac{Tx}{\theta_E} \right)}{\frac{4\alpha\nu_s\hbar}{k_B\theta_E}} \right] - 4 \left[\frac{Tx}{\theta_E} \left(1 - \frac{Tx}{\theta_E} \right) \right]$$

The factor before the integral of the Callaway term can be calculated as follows.

$$\frac{k_B}{2\pi^2\nu_s} \left(\frac{k_B T}{\hbar} \right)^3 = \frac{\hbar}{2\pi^2} \left(6\pi^2 \frac{N}{V} \right)^{\frac{1}{3}} \left(\frac{k_B}{\hbar} \right)^3 \frac{T^3}{\Theta_D} = 4.6729 * 10^{-2} * \left(\frac{N}{V} \right)^{\frac{1}{3}} \quad (\text{A.19})$$

For CePd₃ the number of atoms per unit cell N is 4 and with a lattice parameter a of 0.4128 nm one gets a unit cell volume V of about $7.032 \times 10^{-29} \text{ m}^3$ which leads to a ratio $N/V = 5.69 \times 10^{28} \text{ m}^{-3}$. Taking into account, that the data has a dimension of [mW/cmK], while the described parameters are calculated for [W/mK], one has to multiply the factor with 10. Finally the coefficient of the Callaway term for CePd₃ equals 1.7970×10^9 . Of course this coefficient changes with the grade of doping and substitution, but the maximum deviations for CePd₃B_{0.4} and CeRh₃ are smaller than 3% and therefore neglected. On the CePd₃B _{y} -series we have studied if changing of this factor by about one order of magnitude has an effect on the evolution of the other fit parameters according increasing y . It can be assumed that the tendencies are specified correctly with minor changes in detail as can be seen in Fig. A.1, where the fit-parameters according to the W -Eqn and the WF - l using $K = 2.8526 \times 10^8$ are compared to a fit-series using $K = 1.7970 \times 10^9$ and the WF - l . It is evident that the differences between the interpretation according to WF - l and W -Eqn are larger, than that between WF - l using two different K -values. Only the boundary scattering parameter shows strong deviations.

User defined function corresponding to Eqn. A.10

K=4.6729e-2;	'factor using Debye and Callaway
N=4;	'atoms per unit cell
V=7.032e-29;	'unit cell volume
F = 10*K*(N/V)^(1/3);	'dimension correction*K * (N/V)^(1/3)
F1=#A*\$^4*X^4;	'point defect scattering
F2=#B*\$^2*X^3*EXP(-#E/(3*X));	'umklapp processes
F3=#C;	'boundary scattering
F4=#D*X*\$;	'electron phonon scattering
F5=1/(F1+F2+F3+F4)	' $\tau_c = 1/(\tau_D^{-1} + \tau_U^{-1} + \tau_B^{-1} + \tau_{el-ph}^{-1})$
F9=(\$^4*EXP(\$)/(EXP(\$) - 1)^2)*F5	'integrand
Y=(F*X^3*#E/X)*AI(9,0,(#E/X))+#F*X^3	'factor*T ³ /Θ _D *Integral+radiation losses

For the six fit-parameters physical reasonable borders have to be found. To do this the coefficients of the scattering times are set zero. Based on the resistivity data we assumed 200 K for $\Theta_{D,min}$ and also based on literature data ($\Theta_D < 350 \text{ K}$ [60]) $\Theta_{D,max}$ was fixed at 400 K. The radiation loss coefficient was found by experience in an interval of [5e-7,1e-5]. The maximum of a scattering parameter was determined by setting all other scattering dependent factors zero, the radiation losses to maximum and Θ_D to 250 K. Then the test-parameter was increased until the generated curve touches the measured curve. This has to be the maximum value for the according scattering parameter, because further enhancement would lead to smaller thermal conductivity values as that which were measured.

The model by Wilson describes the thermal resistivity of the electrons, by two additive terms. The first term expresses the scattering of electrons on

imperfections, follows the $WF-l$ according to Eqn. 1.38 and can be written as:

$$W_{e,0} = \frac{\rho_0}{L_0 T} \quad (\text{A.20})$$

$W_{e,ph}$ caused by electron scattering on phonons can be deduced similarly to the Bloch-Grüneisen equation 1.14 and is known as *Wilson equation*.

$$W_{e,ph} = \frac{4R}{L_0 T} \left(\frac{T}{\theta_D} \right)^5 \left\{ \left[1 + \frac{3}{\pi^2} \left(\frac{k_F}{q_D} \right)^2 \left(\frac{\theta_D}{T} \right)^2 \right] J_5(\theta_D/T) - \frac{1}{2\pi^2} J_7(\theta_D/T) \right\} \quad (\text{A.21})$$

R is a material dependent constant, k_F is the wave vector at the Fermi energy and q_D is defined by the dispersion relation $q_D = \frac{\omega_D}{v_s}$ with the Debye frequency

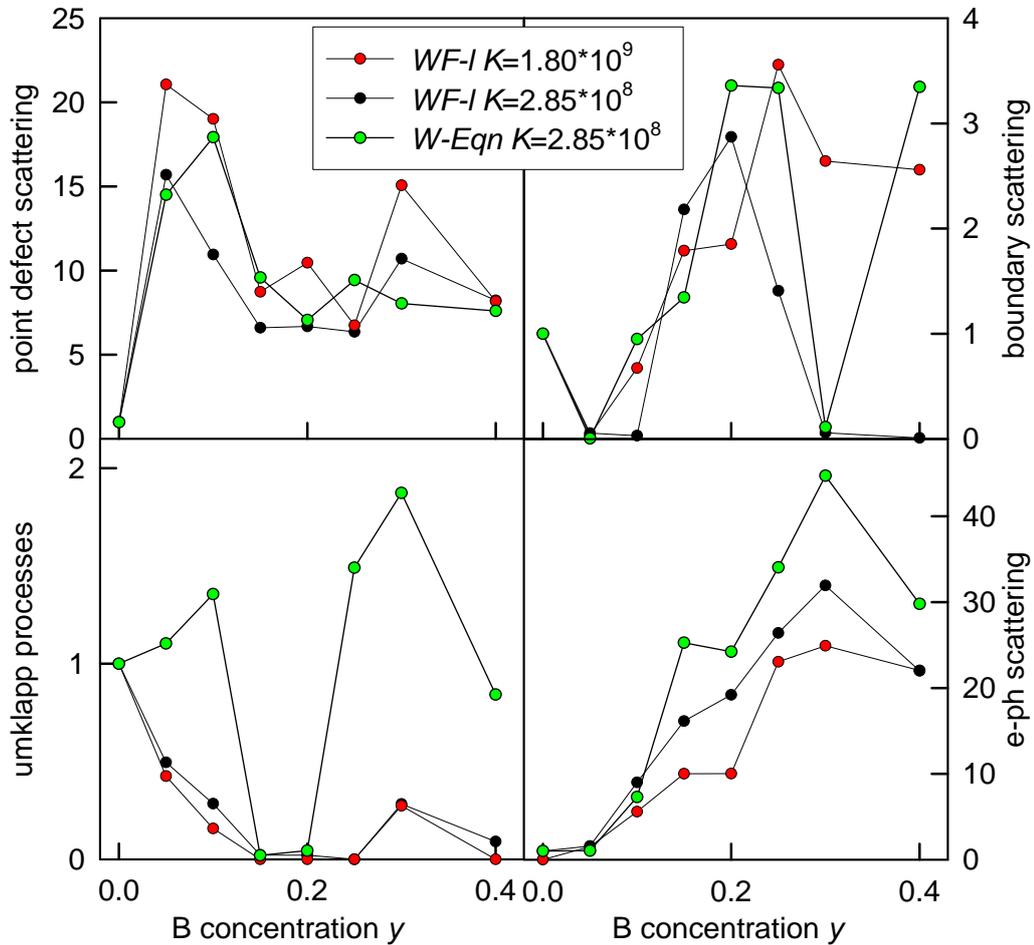


Figure A.1: Comparison of the generated fit-parameters according to the $W-Eqn$ and the $WF-l$ using two different scaling constants K

ω_D . The formulae for $W_{e,0}$ and $W_{e,ph}$ according to *W-Eqn* and λ_{ph} derived by Callaway can be combined into one general fit-function including eight fit-parameters.

User defined function corresponding to Wilson's model

F1=#A/X;	' Θ_D/T
F2=#B/X;	' $W_{e,0} = \alpha/T$
F3=#C/X;	' $4R/(L_0.T)$
F4=\$^5/(EXP(-\$)+EXP(\$)-2);	'J5
F5=\$^7/(EXP(-\$)+EXP(\$)-2);	'J7
F6=F3*F1^-5*((1+(3*F1^2/(4*PI^2)))*... ...*AI(4,0,F1)-AI(5,0,F1)/(2*PI^2));	' $W_{e,ph}$
F7=F2+F6;	' $W_{e,tot}$
K=1797025870;	'Callaway factor
F8=#D*\$^4*X^4+#E*\$^2*X^3*... ...*EXP(-#A/(3*X))+#F+#G*X*\$;	' $\tau_c^{-1} = (\tau_D^{-1} + \tau_U^{-1} + \tau_B^{-1} + \tau_{el-ph}^{-1})$
F9=\$^4*EXP(\$)/(EXP(\$)-1)^2/F8	'integrand Callaway
Y=(K*X^3/#A)*AI(9,0,F1)+1/F7+#H*X^3	' $\lambda_{tot} = faktor * (T^3/\theta_D) * integral + \lambda_e + radiation losses$

Bibliography

- [1] Seebeck, T. J. In *Abhandlungen der Königlichen Akademie der Wissenschaften zu Berlin*, 289. (1821).
- [2] Peltier, J. *Ann. Chim* **89**, 371 (1834).
- [3] Besnus, M., Kappler, J., and Meyer, A. *J. Phys. F: Met. Phys.* **13**, 597–606 (1983).
- [4] Gambino, R., Grobman, W., and Toxen, A. *Appl. Phys. Lett.* **22**(10), 506–507 (1973).
- [5] Harris, I. R., Norman, M., and Gardner, W. E. *Journal of the Less Common Metals* **29**(3), 299–309 (1972).
- [6] Mihalisin, T., Scoboria, P., and Ward, J. A. *Phys. Rev. Lett.* **46**(13), 862–865 Mar (1981).
- [7] Culverhouse, S. R., Rainford, B. D., and Paul, D. M. *Journal of Magnetism and Magnetic Materials* **108**(1-3), 121–122 (1992).
- [8] Gambke, T., Elschner, B., Schaafhausen, J., and Schaffer, H. In *Valence Fluctuations in Solids*, Falicov, L., editor, 447–450. North Holland, (1981).
- [9] Dhar, S., Malik, S., and Vijayaraghavan, R. *Phys. Rev. B* **24**(10), 6182–6184 Nov (1981).
- [10] Gordon, R. A., Jones, C., Alexander, M., and DiSalvo, F. J. *Physica B: Condensed Matter* **225**(1-2), 23–32 (1996).
- [11] Sthioul, H., Jaccard, D., and Sierro, J. In *Valence Instabilities*, P.Wachter and H.Boppart, editors, 443–445. North Holland, (1982).
- [12] Houshiar, M., Adroja, D. T., and Rainford, B. D. *Physica B* **223-224**, 268–270 (1996).

- [13] Grimvall, G. *The Electron-Phonon Interaction in Metals*, volume XVI of *Series of Monographs on Selected Topics in the Solid State Physics*. North Holland, (1981).
- [14] Grüneisen, E. *Ann. Physik* **16**, 530 (1933).
- [15] Landau, L. and Pomeranchuk, I. *Phys. Z. Sowjet.* **10**, 649–59 (1936).
- [16] Zhao, J., Bass, J., Jr., W. P., and Schroeder, P. *J. Phys. F: Met. Phys.* **16**, L271–L274 (1986).
- [17] Bauer, E., Hilscher, G., Michor, H., Paul, C., Scheidt, E. W., Griбанov, A., Seropegin, Y., Noël, H., Sigrist, M., and Rogl, P. *Phys. Rev. Lett.* **92**(2), 027003 Jan (2004).
- [18] Stevens, K. *Proc. Phys. Soc. A* **65**, 209 (1952).
- [19] Jensen, J. and Mackintosh, A. *Rare earth magnetism*. Clarendon Pr., Oxford, (1911).
- [20] Kondo, J. *Progr. Theor. Physics* **32**, 37 (1964).
- [21] Freimuth, A. *J. Magn. Magn. Mater.* **68**, 28 (1987).
- [22] Wilson, A. H. *Proc. Cambridge Phil. Soc.* **33**, 371 (1937).
- [23] Callaway, J. *Phys. Rev.* **113**, 1046 (1959).
- [24] Klemens, P. *Proc. Roy. Soc. A* **208**, 108 (1951).
- [25] Holland, M. G. *Phys. Rev.* **132**(6), 2461–2471 Dec (1963).
- [26] Slack, G. A. and Galginaitis, S. *Phys. Rev.* **133**(1A), A253–A268 Jan (1964).
- [27] Ziman, J. M. *Electrons and phonons : the theory of transport phenomena in solids*, volume XIV of *The international series of monographs on physics*. Clarendon Pr., Oxford, (1960).
- [28] Berman, R. *Thermal conduction in solids*, volume XI of *Oxford studies in physics*. Clarendon Pr., Oxford, (1958).
- [29] Parrott, J. and Stuckes, A. *Thermal Conductivity of Solids*. Pion Limited, London, (1975).
- [30] Smirnov, I., Oskotskii, V., and Parfenev, L. *Journal of the Less Common Metals* **111**(1-2), 353–357 (1985).

-
- [31] Kitagawa, J., Sasakawa, T., Suemitsu, T., Echizen, Y., and Takabatake, T. *Phys. Rev. B* **66**(22), 224304 Dec (2002).
- [32] Aoki, Y., Chernikov, M. A., Ott, H. R., Sugawara, H., and Sato, H. *Phys. Rev. B* **62**(1), 87–90 Jul (2000).
- [33] Yang, J. *Thermal conductivity*, chapter 1.1 Theory of Thermal Conductivity. Springer (2004).
- [34] Ziman, J. M. *Phil. Mag.* **1**, 191–198 (1956).
- [35] Ziman, J. M. *Phil. Mag.* **2**, 292 (1957).
- [36] Griffin, A. and Carruthers, P. *Phys.Rev.* **131**, 1976–1992 (1963).
- [37] Pippard, A. *Phil. Mag.* **46**, 1104–1114 (1955).
- [38] Einstein, A. *Ann. Phys. (Leipzig)* **35**, 679 (1911).
- [39] Cahill, D. and Pohl, R. *Solid State Communications* **70**(10), 927–930 (1989).
- [40] Wagner, M. *Phys.Rev.* **131**(4), 1443–1455 (1963).
- [41] Walker, C. and Pohl, R. *Phys.Rev.* **131**(4), 1433–1442 (1963).
- [42] Koterlyn, M., Babych, O., and Koterlyn, G. *Journal of Alloys and Compounds* **325**(1-2), 6–11 (2001).
- [43] Nolas, G., Sharp, J., and Goldsmid, H. *Thermoelectrics - Basic Principles and New Materials Developments*. Springer-Verlag, Berlin Heidelberg, (2001).
- [44] Bhandari, C. and Rowe, D. *CRC Handbook of Thermoelectrics*. CRC Press, (1995).
- [45] Roisnel, T. *Materials-Science-Forum* **118**, 378–381 (2001).
- [46] Giannò, K., Sologubenko, A. V., Chernikov, M. A., Ott, H. R., Fisher, I. R., and Canfield, P. C. *Phys. Rev. B* **62**(1), 292–300 Jul (2000).
- [47] Tritt, T. *Semiconductors and Semimetals*. Academic Press, (2001). Chap.2 p.25.
- [48] Scoboria, P., Crow, J. E., and Mihalisin, T. *J. of Appl. Phys.* **50**(B3), 1895–1897 (1979).
- [49] Proctor, K., Jones, C., and DiSalvo, F. *Journ. of Phys. and Chem. of Solids* **60**(5), 663–671 (1999).

- [50] Kappler, J.-P., Herr, A., Schmerber, G., Derory, A., Parlebas, J.-C., N. Jaouen, F. W., and Rogalev, A. *Eur. Phys. J. B* **37**, 163–167 (2003).
- [51] Schneider, H. and Wohlleben, D. *Zeitschrift-fur-Physik-B-Condensed-Matter* **44**(3), 193–202 (1981).
- [52] Kanai, K., Y. Tezuka, Terashima, T., Muro, Y., Ishikawa, M., Uozumi, T., A. Kotani, G. S., Kappler, J., Parlebas, J., and S. Shin. *Phys. Rev. B* **60**(8), 5244–5250 Aug (1999).
- [53] Maekawa, S., Kashiba, S., and Tachiki, M. *J. Phys. Soc. Jap.* **55**, 3194 (1986).
- [54] D. Kaczorowski, K. G. Poster presented at "IICAM Workshop on Correlated Thermoelectricity" (<http://hvar05.ifs.hr/>), Sept. (2001).
- [55] Srinivasan, M., Vaidya, S., Dhar, S., and Malik, S. *High Temperature - High Pressure* **20**, 525 (1988).
- [56] Sereni, J., Nieva, G., Kappler, J., Besnus, M., and Meyer, A. *J. Phys. F: Met. Phys.* **16**, 435–448 (1986).
- [57] Yubuta, K., Nomura, A., Nakajima, K., and Shishido, T. *J. Alloys Comp.* **426**, 308–311 (2006).
- [58] Dhar, S., Gschneidner, K., Bredl, C., and Steglich, F. *Phys. Rev. B* **39**(4), 2439–2441 Feb (1989).
- [59] Callaway, J. and von Baeyer, H. *Phys. Rev.* **120**, 1149 (1960).
- [60] Loong, C.-K., Zarestky, J., Stassis, C., McMasters, O., and Nicklow, R. *Phys. Rev. B* **38**(11), 7365–7369 Oct (1988).
- [61] Jones, C., Gordon, R., Cho, B., DiSalvo, F., Kimb, J. S., and Stewart, G. R. *Physica B: Condensed Matter* **262**(3-4), 284–295 (1999).
- [62] Lawrence, J., Thompson, J., and Chen, Y. *Phys. Rev. Lett.* **54**(23), 2537–2540 Jun (1985).
- [63] Shapiro, S., Stassis, C., and Aeppli, G. *Phys. Rev. Lett.* **62**(1), 94–97 Jan (1989).
- [64] Mihalisin, T., Scoboria, P., and Ward, J. A. In *Valence Fluctuations in Solids*, Falicov, L., editor, 61–65. North Holland, (1981).

List of publications

1. H. Fillunger, M. Foitl, K. Hense, I. Kajgana, A. Kasztler, H. Kirchmayr, R. Lackner, J. Leoni, R. Maix, M. Müller. IEEE Transactions on Applied Superconductivity **12**(1), 1049-1051 (2002).

"Optimized Heat Treatment of Internal Tin Nb₃Sn Strands"

2. H. Fillunger, M. Foitl, K. Hense, I. Kajgana, A. Kasztler, H. Kirchmayr, R. Lackner, J. Leoni, R. Maix, T. Matthias, J. Fidler. Physica C **372-376**, 1758-1761 (2002).

"Influence of the annealing time of internal tin Nb₃Sn strands on the critical current and the magnetization losses"

3. K. Hense, H. Fillunger, I. Kajgana, H. Kirchmayr, R. Lackner, R. Maix, M. Müller. Fusion Engineering and Design **66-68**, 1103-1107 (2003).

"Optimisation of the reaction heat treatment cycle of internal tin and bronze Nb₃Sn strands for ITER"

4. K. Hense, H. Kirchmayr, P. Kovac, R. Lackner, M. Müller, W. Pachla, J. Pitel, M. Polak, P. Usak. Physica C **392-396**(2), 1007-1010 (2003).

"Preparation and characterization of Bi-2223 tapes"

5. K. Hense, M. Müller, R. Lackner, H. Kirchmayr, R. Maix, H. Fillunger. Physica C **401**(1-4), 214-217 (2004).

"Scaling behaviour for the exponents of U-I-, U-B- and U-T-measurements"

6. M. Müller, K. Hense, H. Kirchmayr, R. Lackner. Applied Superconductivity 2003, Proceedings of the 6th EUCAS, Sorrento, Italy 14-18. Sept. 2003 Institute of Physics Conference Series Number **181**, 2284-2289 (2004).

"A model for the prediction of the exponents of U-I and U-T-characteristics of multifilamentary Nb₃Sn-strands"

7. R. Lackner, K. Hense, H. Kirchmayr, J. Leoni, M. Müller, L. Jansak, M. Polak Applied Superconductivity 2003, Proceedings of the 6th EUCAS, Sorrento, Italy 14-18. Sept. 2003 Institute of Physics Conference Series Number **181**, 2379-2385 (2004).
"Effect of filament arrangement on the transversal resistivity of Bi-2223 tapes"
8. K. Hense, M. Müller, H. Schulz Applied Superconductivity 2003, Proceedings of the 6th EUCAS, Sorrento, Italy 14-18. Sept. 2003 Institute of Physics Conference Series Number **181**, 2330-2334 (2004).
"Comparison between Nb₃Sn single strands and triplets"
9. R. Lackner, E. Bauer, P. Rogl Proceedings of the 2nd European Conference on Thermoelectrics, Cracow, (2004).
"Reducing lattice thermal conductivity by valence fluctuations: an experimental study on Ce(Pd_{1-x}Rh_x)₃"
10. D. Berardan, E. Alleno, C. Godart, M. Puyet, B. Lenoir, R. Lackner, E. Bauer, L. Girard, D. Ravot. Journal of Applied Physics **98**(3), 33710-1-6 (2005).
"Improved thermoelectric properties in double-filled Ce_{y/2}Yb_{y/2}Fe_{4-x}(Co/Ni)_xSb₁₂-skutterudites"
11. E. Bauer, R. Lackner, G. Hilscher, H. Michor, M. Sieberer, A. Eichler, A. Griбанov, Y. Seropegin, P. Rogl. Journal of Physics: Condensed Matter **17**(12), 1877-1888 (2005).
"REPt₃Si (RE=La, Pr, Nd, Sm and Gd): isotypes of the heavy fermion superconductor CePt₃Si"
12. R. Lackner, M. Sieberer, H. Michor, G. Hilscher, E. Bauer, P. Salamakha, O. Sologub, K. Hiebl. Journal of Physics: Condensed Matter **17**(11), 905-910 (2005).
"Low temperature properties of the ternary compounds CePt₂B and CePt₃B"
13. R. Lackner, E. Bauer, P. Rogl Proceedings of the 3rd European Conference on Thermoelectrics, Nancy, (2005).
"Transport properties of Ce(Pd_{1-x}Rh_x)₃ in a wide temperature range"
14. M. Nicklas, G. Sparn, R. Lackner, E. Bauer, F. Steglich Physica B **359-361**, 386-8 (2005).
"Effect of hydrostatic pressure on the ambient pressure superconductor CePt₃Si"

15. A. Griбанov, A. Tursina, E. Murashova, Yu. Seropegin, E. Bauer, H. Kaldarar, R. Lackner, H. Michor, E. Royanian, M. Reissner, P. Rogl Journal of Physics: Condensed Matter **18**, 9593-9602 (2006).
"New orthorhombic modification of equiatomic CePdAl"
16. E. Bauer, I. Bonalde, A. Eichler, G. Hilscher, Y. Kitaoka, R. Lackner, St. Laumann, H. Michor, M. Nicklas, P. Rogl, E. Scheidt, M. Sigrist, M. Yogi in: "LOW TEMPERATURE PHYSICS: 24th International Conference on Low Temperature Physics; LT24", AIP Conference Proceedings **850**, 695-702 (2006).
"CePt₃Si: Heavy Fermion Superconductivity and Magnetic Order without Inversion Symmetry"
17. E. Alleno, D. Berardan, C. Godart, M. Puyet, B. Lenoir, R. Lackner, E. Bauer, L. Girard, D. Ravot Physica B **383**(1), 103-106 (2006).
"Double filling in skutterudites: A promising path to improved thermoelectric properties"
18. E. Bauer, St. Laumann, R. Lackner. H. Michor, G. Hilscher Physica B **378-380**, 386-387 (2006).
"Crystal electric field effects in Ce_{1-x}La_xPt₃Si"
19. R. Lackner, E. Bauer, P. Rogl Physica B **378-380**, 835-836 (2006).
"Study of the thermoelectric properties of CePd₃B_x"
20. M. Giovannini, E. Bauer, G. Hilscher, R. Lackner, H. Michor, A. Saccone Physica B **378-380**, 831-2 (2006).
"Structure and Kondo properties of the novel compound CeCu₂Mg"
21. E. Bauer, R. Lackner, G. Hilscher, H. Michor, E.W. Scheidt, W. Scherer, P. Rogl, A. Griбанov, A. Tursina, Y. Seropegin, G. Giester Phys.Rev.B **73**(10), 104405-1-7 (2006).
"Crystal chemistry and low-temperature properties of Yb₁₈Pt_{51.1}Si_{15.1} (approximately=YbPt₃Si)"
22. St. Laumann, H. Kaldarar, R. Lackner, E. Bauer Contributed in Fukuoka Aug. 2006, IN PRESS
"Pressure-, field- and substitution studies on heavy fermion superconductor CePt₃Si"
23. H. Michor, R. Lackner, H. Kaldarar, L. Fornasari, E. Bauer, G. Hilscher, U. Schwarz, H. Rosner Contributed in Fukuoka Aug. 2006, IN PRESS
"Pressure effects upon the itinerant magnetism in RCo₉Si₄"

List of conference contributions

- **5th European Conference on Applied Superconductivity (EUCAS'01), Copenhagen, Denmark; 25-30 August 2001**
Poster: *"Optimized Heat Treatment of Internal Tin Nb₃Sn Strands"*
H. Fillunger, M. Foitl, K. Hense, I. Kajgana, A. Kasztler, H. Kirchmayr, R. Lackner, J. Leoni, R. Maix, M. Müller
- **OST Project meeting (GZ45.481/2-VII/B/8a/2000) , Warsaw, Poland; 6-7 June 2002**
Talk: *"Measurement possibilities and future investigations on Bi₂₂₂₃/Ag multifilament tapes"*
R. Lackner, H. Kirchmayr
- **US-Japan Workshop on Superconducting Magnet Technology, MIT Plasma Fusion Centre, Cambridge, USA; 12-15 August 2002**
Talk: *"Optimisation of the Reaction Heat Treatment Cycle of Nb₃Sn Strands for ITER"*
R. Maix, K. Hense, H. Fillunger, I. Kajgana, H. Kirchmayr, R. Lackner, M. Müller
- **SOFT 2002, Helsinki; 9-13 September 2002**
Poster: *"Optimisation of the Reaction Heat Treatment cycle of Internal Tin and Bronze Nb₃Sn Strands for ITER"*
K. Hense, H. Fillunger, I. Kajgana, H. Kirchmayr, R. Lackner, R. Maix, M. Müller
- **ISS 2002, Yokohama, Japan; 11-13 November 2002**
Poster: *"Preparation and Characterization of Bi-2223 tapes"*
K. Hense, H. Kirchmayr, P. Kovàc, R. Lackner, M. Müller, W. Pachla, J. Pitel, M. Polák, P. Uask

- **Topical Conference on the Voltage-Current Relation in Technical Superconductors (ICMC'03), Enschede, Netherlands; 25-28 May 2003**

Talk: *"Scaling behaviour for the exponents of U-I-, U-B- and U-T-measurements"*

K. Hense, M. Müller, R. Lackner, H. Kirchmayr, R. Maix, H. Fillunger

- **6th European Conference on Applied Superconductivity (EUCAS'03), Sept. 14th to 18th 2003, Naples, Italy,**

Poster: *"A model for the prediction of the exponents of U-I and U-T-characteristics of multifilamentary Nb₃Sn-strands"*

M. Müller, K. Hense, H. Kirchmayr, R. Lackner

Poster: *"Effect of filament arrangement on the transversal resistivity of Bi-2223 tapes"*

R. Lackner, K. Hense, H. Kirchmayr, J. Leoni, M. Müller, L. Jansak, M. Polak

Poster: *"Comparison between Nb₃Sn single strands and triplets"*

K. Hense, M. Müller, H. Schulz

- **19th Workshop on Novel Materials and Superconductors, Planeralm, Austria; 22-28 February 2004**

Poster: *"Effect of Ge and B doping on the superconductivity in CePt₃Si"*

E. Bauer, A. Buchsbaum, G. Hilscher, R. Lackner, H. Michor, C. Paul, E. Scheidt, A. Griбанov, Yu. Seropegin, H. Noel, M. Sigrist, P. Rogl

Poster: *"A Model for the Prediction of the Exponents of U-I- and U-T-Characteristics of Multifilamentary Nb₃Sn Strand"*

M. Müller, K. Hense, H. Kirchmayr, R. Lackner, H. Schulz

Poster: *"The effect of doping upon superconductivity in La₃Ni₂B₂N₃"*

M. Sieberer, H. Michor, M. Della Mea, P. Hehenberger, C. Hofstätter, R. Lackner, E. Bauer, G. Hilscher, A. Grytsiv, P. Rogl

- **20th General Conference of the Condensed Matter Division, European Physical Society, Prag, Czech Republic; 19-23 July 2004**

Poster: *"Magnetic properties of RPt₃Si"*

H. Michor, E. Bauer, G. Hilscher, C. Hofstätter, R. Lackner, M. Sieberer, A. Griбанov, Yu. Seropegin, P. Rogl

- **2nd International Symposium on Physics of Solids Under High Pressure Using Nuclear Probes, HPNP 04, Cologne, Germany; 20-24 July 2004**

Invited talk: *"Ground state behaviour of $Yb_2Pd_2(In,Sn)$: Possibility of two quantum critical points"*

E. Bauer, G. Hilscher, R. Lackner, H. Michor, C. Paul, Y. Aoki, H. Sato, D.T. Adroja, J.-G. Park, P. Bonville, C. Godart, M. Giovannini, A. Saccone

Poster: *"Low temperature properties of ternary $CePt_3B$ and $CePt_2B$ "*

R. Lackner, M. Sieberer, E. Bauer, G. Hilscher, H. Michor, O.L. Sologub, K. Hiebl

- **International Conference on Strongly Correlated Electron Systems (SCES'04), Karlsruhe, Germany; 26-30 July 2004**

Poster: *"Effect of hydrostatic pressure on the ambient pressure superconductor $CePt_3Si$ "*

M. Nicklas, G. Sparn, R. Lackner, E. Bauer, F. Steglich

- **2nd European Conference on Thermoelectrics, Krakow, Poland; 15-17 Sept. 2004**

Talk: *"Improved thermoelectric properties in the double filled skutterudites $(Ce-Yb)_y(Fe-Co-Ni)_4Sb_{12}$ "*

D. Berardan, E. Alleno, O. Rouleau, C. Godart, M. Puyet, B. Lenoir, H. Scherrer, L. Girard, D. Ravot, R. Lackner, E. Bauer

Poster: *"Reducing lattice thermal conductivity by valence fluctuations: an experimental study on $Ce(Pd_{1-x}Rh_x)_3$ "*

R. Lackner, E. Bauer, P. Rogl

- **3rd European Conference on Thermoelectrics (ECT'05), Nancy, France; 31 September - 1 October 2005**

Poster: *"Transport properties of $Ce(Pd_{1-x}Rh_x)_3$ in a wide temperature range"*

R. Lackner, E. Bauer, P. Rogl

- **20th Workshop on Novel Materials and Superconductors, Planeralm, Austria; 12-19 February 2005**

Poster: *"Reducing lattice thermal conductivity by valence fluctuations: an experimental study on $Ce(Pd_{1-x}Rh_x)_3$ "*

R. Lackner, E. Bauer, P. Rogl

- **International Conference on Strongly Correlated Electron Systems (SCES'05), Vienna, Austria; 26-30 July 2005**
Poster: *"Study of the Thermoelectric Properties of $CePd_3B_x$ "*
R. Lackner, E. Bauer, P. Rogl
- **IICAM Workshop on Correlated Thermoelectricity, Hvar, Croatia; 25-30 September 2005**
Poster: *"Driving thermoelectricity by doping in $CePd_3$ "*
R. Lackner, E. Bauer, P. Rogl
- **Workshop on "Quantum Complexities in Condensed Matter", Cambridge, UK; 04-07 July 2006**
Poster: *"Crystal chemistry and low temperature properties of novel $Yb_{18}Pt_{51.1}Si_{15.1}$ ($YbPt_3Si$)"*
E. Bauer, R. Lackner, H. Kaldarar, E. Royanian, H. Michor, G. Hilscher, E.-W. Scheidt, W. Scherer, A. Griбанov, A. Tursina, Yu. Seropegin, P. Rogl, G. Giester
- **15th International Conference on Solid Compounds of Transition Elements, Krakow, Poland; 15-20 July 2006**
Poster: *"New orthorhombic modification of equiatomic $CePdAl$ "*
A. Griбанov, A. Tursina, E. Murashova, Yu. Seropegin, P. Rogl, H. Kaldarar, R. Lackner, E. Bauer, G. Hilscher, H. Michor, L. Lipatov
- **Novel Pressure-induced Phenomena in Condensed Matter Systems, Fukuoka, Japan; 15-19 August 2006**
Invited talk: *"Pressure effects upon the itinerant magnetism in RCo_9Si_4 "*
H. Michor, R. Lackner, H. Kaldarar, L. Fornasari, E. Bauer, G. Hilscher, U. Schwarz, H. Rosner
Poster: *"Pressure-, field-, and substitution studies on heavy fermion superconductor $CePt_3Si$ "*
St. Laumann, H. Kaldarar, R. Lackner, E. Bauer

Curriculum Vitae

Dipl.-Ing. Robert Lackner

Neugasse 10; A-2453 Sommerein

Tel.: ++ 43(0) 650 9252631

e-mail: lackner@ifp.tuwien.ac.at

Persönliche Daten:

Geburtsdatum: 28.4.1977

Geburtsort: Wien

Staatsbürgerschaft: Österreich

Familienstand: verheiratet (mit Doris Lackner (ehem. Brunner) seit 31.07.2003)

Kinder: Maximilian (23.04.2003), Rebekka (30.10.2004)

Wehrdienst: abgeleistet (01/06-07/06)

Bildungsweg:

09/87-06/95 BG und BRG Neusiedl/See

07.06.1995 Reifeprüfung

10/95-01/04 Studium der Technischen Physik an der TU Wien

29.01.2004 Diplomingenieur der Technischen Physik

unter der Betreuung von o. Univ. Prof. Dr. Hans Kirchmayr
am Institut für Festkörperphysik der TU-Wien,

Diplomarbeit: "Effect of filament arrangement on the transversal resistivity of Bi-2223 tapes"

Praxiserfahrung:

01.00 - 06.03 Projektassistent im Rahmen des EFDA-Projekts
(ITER Task TWO-T405-2/01) "Conductor Layout Optimisation"
Betreuung: o. Prof. Dipl.Ing. Dr. Hans Kirchmayr
Institut für Experimentalphysik, TU-Wien

12.03 - 01.06 Projektassistent im Rahmen des FWF-Projektes (P 16370)
"Neuer Ansatz zur Wärmeleitfähigkeit in Thermoelektika"
Betreuung: a.o. Prof. Dipl.Ing. Dr. Ernst Bauer
Institut für Festkörperphysik, TU-Wien

08.06 - 07.07 Projektassistent im Rahmen des FWF-Projektes (P 19165-N16)
"Reduktion der thermischen Leitfähigkeit in Thermoelektika"
Betreuung: a.o. Prof. Dipl.Ing. Dr. Ernst Bauer
Institut für Festkörperphysik, TU-Wien